SURFACE AND INTERFACE DIFFUSION PROCESSES IN NANOSCALE THIN FILMS

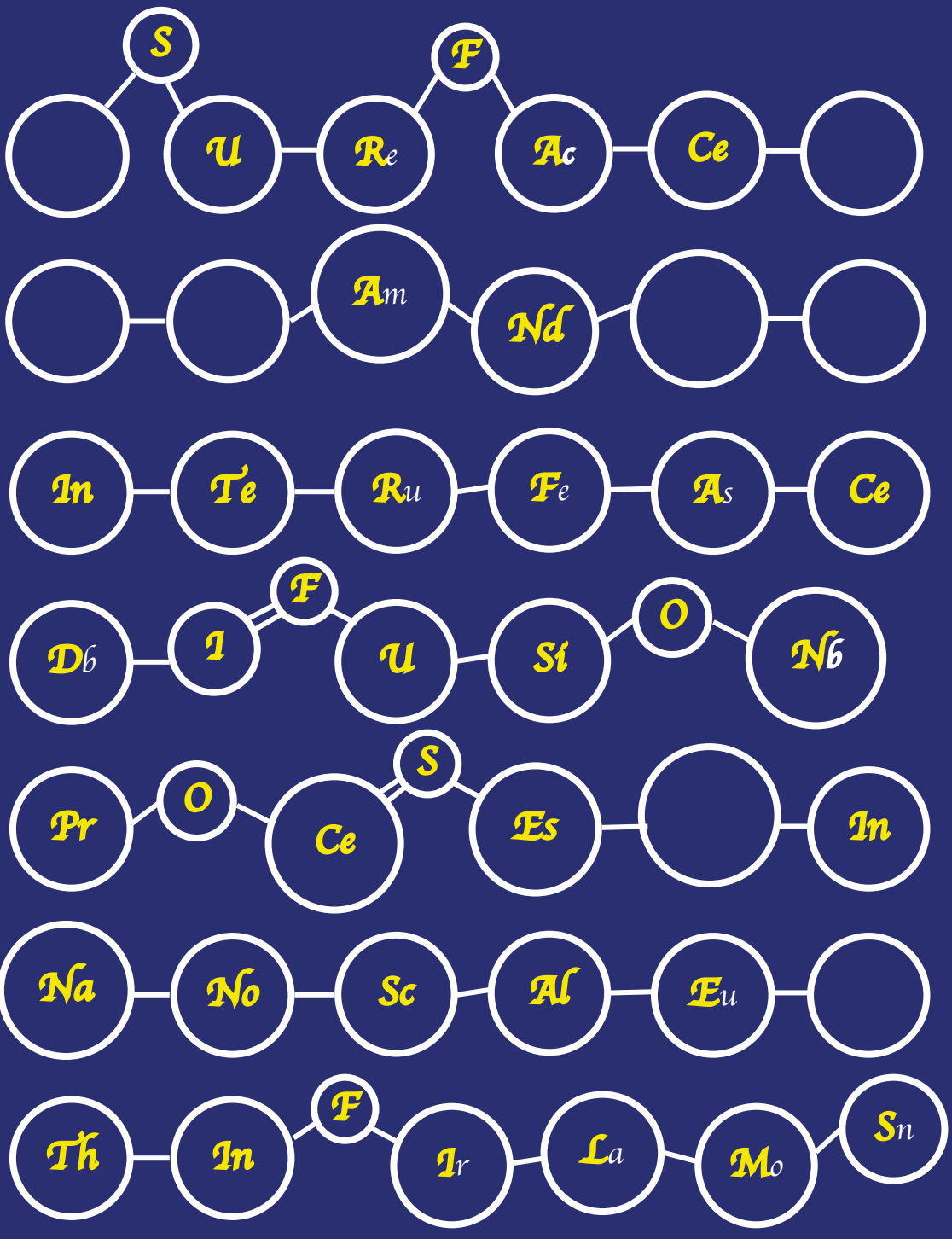

Anirudhan Chandrasekaran

SURFACE AND INTERFACE DIFFUSION PROCESSES IN NANOSCALE THIN FILMS

Anirudhan Chandrasekaran

SURFACE AND INTERFACE DIFFUSION PROCESSES IN NANOSCALE THIN FILMS

DISSERTATION

to obtain
the degree of doctor at the Universiteit Twente,
on the authority of the rector magnificus,
prof. dr. ir. A. Veldkamp,
on account of the decision of the Doctorate Board
to be publicly defended
on Wednesday 16 November 2022 at 16.45 hours
by

Anirudhan Chandrasekaran

born on the 29th of June, 1992
in Madurai, Tamil Nadu, India

This dissertation has been approved by:

Supervisor: Prof. dr. F. Bijkerk

Co-supervisor: Dr. ir. R.W.E. van de Kruijs

This work was carried out at the Industrial Focus Group XUV Optics, MESA+ Institute for Nanotechnology, University of Twente. We acknowledge the support and funding from the industrial partners ASML, ZEISS, Malvern Panalytical, TNO as well as the Province of Overijssel and the Dutch Organization for Scientific Research NWO.

Cover design	:	Anirudhan Chandrasekaran
Printed by	:	Ipskamp, Enschede
ISBN	:	978-90-365-5476-3
DOI	:	10.3990/1.9789036554763

Graduation Committee:

Chair / secretary:	**Prof. dr. J.L. Herek** Universiteit Twente
Supervisor:	**Prof. dr. F. Bijkerk** Universiteit Twente, TNW, XUV Optics
Co-supervisor:	**Dr. ir. R.W.E. van de Kruijs** Universiteit Twente, TNW, XUV Optics
Committee Members:	**Prof. dr. F. Delmotte** Institut d'Optique, Universite Paris-Saclay
	Prof. dr. D. Primetzhofer Uppsala Universitet
	Prof. dr. ir. J.W.M. Hilgenkamp Universiteit Twente, TNW, Interfaces and Correlated Electron Systems
	Prof. dr. ir. H.J.W. Zandvliet Universiteit Twente, TNW, Physics of Interfaces and Nanomaterials
	Prof. dr. M.D. Ackermann Universiteit Twente, TNW, XUV Optics

List of Publications

This thesis is based on the following publications:

Chapter 2

Chandrasekaran, A.; van de Kruijs, R. W. E.; Sturm, J. M.; Zameshin, A. A.; Bijkerk, F.
Nanoscale Transition Metal Thin Films: Growth Characteristics and Scaling Law for Interlayer Formation.
ACS Appl. Mater. Interfaces 2019, 11 (49), 46311–46326.
https://doi.org/10.1021/acsami.9b14414.

Chapter 3

Chandrasekaran, A.; van de Kruijs, R. W. E.; Bijkerk, F.
Intermixing and Segregation during Growth of Transition Metal Thin Films on Si and Al Substrate Layers.
In preparation.

Chapter 4

Chandrasekaran, A.; van de Kruijs, R. W. E.; Sturm, J. M.; Bijkerk, F.
Nb Texture Evolution and Interdiffusion in Nb/Si-Layered Systems.
ACS Appl. Mater. Interfaces 2021, 13 (26), 31260–31270.
https://doi.org/10.1021/acsami.1c06210.

Chapter 5

Chandrasekaran, A.; van de Kruijs, R. W. E.; Sturm, J. M.; Bijkerk, F.
Solid state reactions in Zr-Si layered systems during low temperature annealing.
To be submitted.

Contents

CHAPTER 1

Introduction

1.1. BACKGROUND INFORMATION

Over the last decades, a wide range of scientific and industrial communities in the field of microelectronics have explored the advantages of miniaturization* of the critical dimensions of electronic devices. The miniaturization trend has made it possible to embed multiple functionalities within a single device, with additional benefits of reduced manufacturing cost, material usage and power consumption. Computer, telephone, camera, music player, and bank card, which were standalone devices years ago, have now become integral parts of a mobile phone that fits into the palm of a hand. High-tech portable devices such as lab-on-chip, health monitors, and nanosensors play a crucial role in the medical industry, especially in early detection of diseases and preventive care. The advancements in aviation and aerospace industries are enabled by miniaturization technologies that facilitate manufacturing of small and light-weight instruments such as sensors, satellites, and actuators. The size of the basic structures in electronic, optical, and mechanical components in modern devices is in the scale of micro- and nanometers. Further miniaturization, down to molecular- and atomic-scales, is additionally driven by fundamental scientific interests, besides the economic opportunities in the field of consumer device technologies.

Although miniaturization offers immense potential for future technological developments, the path toward the final goal of creating advanced miniature devices is neither direct nor simple. With reducing feature size, the effects of atomic diffusion and interaction become much more obvious and play a dominant role in determining the device functionality. Fabrication of nano- and atomic-scale devices requires atomic scale manufacturing processes,[1] in which atomic diffusion is strongly limited or controlled. Therefore, an in-depth understanding of atomic scale processes, such as diffusion, segregation, and chemical interactions, is inevitable to continue the miniaturization trend in future technologies.

Nanostructures are classified into different types based on the number of dimensions that are in the nanometer scale. Nanosheets and nanofilms are two-dimensional (2D) structures with the third dimension, usually the thickness, in the order of nanometers. One-dimensional (1D) structures, such as nanotubes and nanowires, generally have two of the three dimensions in the nanometer range. Following this classification, zero-dimensional (0D) structures, such as quantum-dots and nanoparticles, have all three dimensions in the nanometer scale. This thesis deals with ultra-thin-film 2D structures with layer thicknesses typically in the range of a few nanometers. In nanoscale thin films, sub-nanometer scale diffusion or segregation of atoms in the growth-direction can completely alter or even destroy the properties of the thin-film structure. The primary focus of this work is to understand

* *Miniaturization in the field of technology can be defined as the process of reducing the size of components in a device*, e.g. reducing the size of transistors in integrated circuit and memory chips

the fundamental mechanisms of atomic diffusion and chemical interactions that occur during layer growth at near room temperature and during low-temperature annealing (< 300 C). The understanding accumulated is essential to overcome the challenges related to fabrication of nanoscale thin films. In the next section, a general introduction to nanoscale thin films is given, and the technical challenges in fabricating high-quality nanoscale layered structures and the scientific knowledge required to tackle those challenges are discussed. The advantages and disadvantages of most commonly used thin-film deposition methods are also reviewed. The last section of this chapter provides an overview of the thesis, including the scope of the work.

1.2. NANOSCALE THIN FILMS

The term nanoscale-thin-films typically describes layers that are in the range of a few nanometers in thickness. The high surface area-to-volume ratio of nanoscale thin-film materials makes them excellent candidates for surface-chemistry related applications such as fuel cells, sensors, and catalysis.[2–4] Ultra-thin corrosion resistant layers are used as protective coatings on top of materials that are generally susceptible to corrosion.[5] Multi-layered thin-film structures, with individual layer thicknesses less than 5 nm, are commonly used in optical and magnetic devices.[6–8] In addition, the ability to deposit ultra-thin films in a controlled way allows us to mimic and utilize various interesting phenomena found in nature, in order to create new applications or improve existing technologies. Bioinspired thin-film materials and structures offer immense potential in the development of technologies such as targeted drug delivery, energy storage, solar cells, and decorative optics.[9–13] Nanoscale thin-film deposition techniques can significantly broaden the scope of designing advanced nano-opto-electro-mechanical devices. In all these applications, it is important to select the right thin-film stack design and deposition technique to fully realize the potentials.

1.2.1. Challenges in Designing and Fabricating Nanoscale Thin Films

Thin-film structures are designed by choosing appropriate layer materials, thicknesses, and stacking order, according to the calculations based on application specific requirements. However, the functional properties of nanoscale thin-structures are often limited by the layer growth characteristics, such as clustering or island formation, phase segregation, intermixing between consecutive layers, roughness buildup, and porous growth. For ultra-thin protective layer coatings (Figure 1.1a), it is necessary to completely cover the underlying layer in order to protect it from the environment. In that regard, island formation or intermixing with the underlying layer can increase the minimum required thickness of the protective layer, which can lead to compromises in the functional properties. For multilayer-stack-based (Figure 1.1b) optical and magnetic applications, the device performance is usually related to the contrast between the layer materials. Intermixing between consecutive layers and high roughness buildup during growth will lead to low contrast between alternating layer materials and

thus, result in poor multilayer performance.[14–16] Crystallinity of the layers (crystalline or amorphous nature) can also have a strong influence on the functional properties of the thin-film structure. For instance, grain boundaries in polycrystalline ultra-thin protective layers can act as a short-circuit pathway for diffusion process, defeating its sole purpose of protecting the underlayer. Furthermore, the current semiconductor and electronic devices have a complex 3D layer architecture.[17,18] Depositing an ultra-thin-film on high-aspect-ratio structures (Figure 1.1c) can result in a trade-off between layer conformality and thickness control. Although some of the layer growth characteristics can be controlled by utilizing an appropriate deposition technique and optimizing the process conditions, modification to the fundamental layer design, in the form of additional interlayers and different layer material combination, is required in most cases to improve layer and interface qualities.[19–21] Therefore, to design and fabricate an ultra-thin-film system, it is primarily important to consider both functional and growth properties of the layer materials. Currently, there is no generalized model in the literature that can predict the layer growth characteristics, such as intermixing, segregation, and island formation processes for a wide range of material combinations. The aim of this thesis is to address this problem by developing a model that can quantitatively or qualitatively predict the layer growth and interface characteristics, which can potentially help with designing and fabricating ultra-thin-film systems with the most suitable layer material combination.

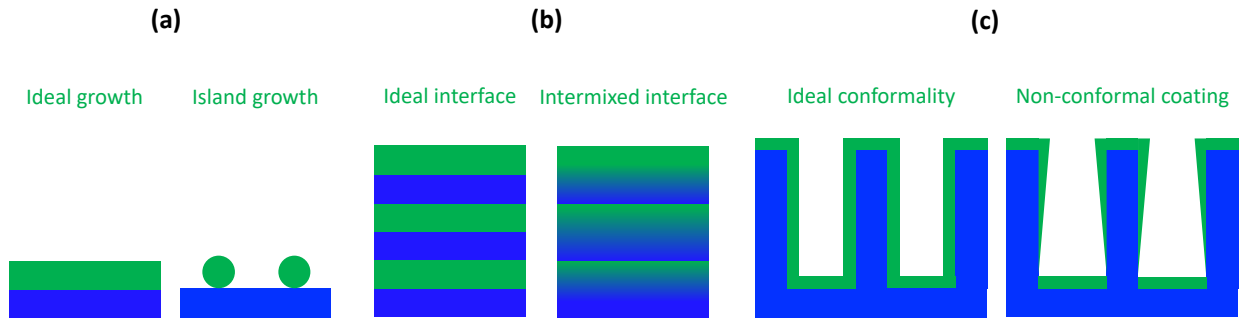

Figure 1.1. Schematic representation of (a) ultra-thin film, (b) multilayer stack, (c) high-aspect-ratio structure

1.2.2. Deposition Methods for Nanoscale Thin Films

Thin films are commonly produced using a bottom-up approach, by building atom-by-atom on a substrate or existing layer through some form of a deposition process.[22] This approach offers more capabilities and better control over the layer properties when compared to the top-down approach, where a thick material is thinned or structured using etching, grinding, and milling methods, until the desired thin film structure is obtained.

The bottom-up deposition methods can be classified into two types: solution-based and vapor-based. The solution-based deposition methods involve wet-chemical processes at the solid (substrate) – liquid (solution) interface, resulting in the deposition of a layer on the substrate. Examples of

solution-based deposition methods are electrodeposition, dip coating, spray pyrolysis, and roll-to-roll screen printing.[23,24] These methods offer high conformality and thickness uniformity over large substrates, along with low manufacturing cost and good scalability. However, depositing nanoscale thin-film layers with good control over layer thickness, purity, and properties is a challenge for solution-based methods because of various factors such as high temperature required to remove solvent residues in the layer, shrinkage and rearrangement of layer material during evaporation of solvent. In vapor-based deposition methods, layer growth occurs through condensation of material in the vapor phase onto a substrate. There are two types of vapor-based methods: chemical vapor deposition (CVD) and physical vapor deposition (PVD). These methods can be used to deposit sub-nanometer thick layers with high accuracy and purity. In addition, they offer the possibility to tune the layer properties by changing the process parameters. Hence, vapor-based techniques are preferred over solution-based methods for depositing nanoscale thin films.

The chemical vapor deposition[25] process involves decomposition and reaction of one or more volatile species known as precursor, in the vicinity of a heated substrate to form a thin-film layer of the desired material. The volatile by-products of the chemical reactions are removed by controlling the gas flow through the chamber. Because of the gaseous nature of the precursor, deposition can take place even in those regions on the substrate that are not directly in line-of-sight, which can be beneficial for applications that require coating of high-aspect-ratio and complex 3D structures. Atomic layer deposition[26] (ALD) is a special kind of CVD process, where the precursors are introduced sequentially into the chamber resulting in a self-limiting reaction on the surface of the substrate. Unlike standard CVD techniques, where deposition is a continuous process, ALD allows for a better thickness control by promoting self-limiting layer-by-layer growth at comparatively lower temperature than CVD. Although CVD methods have several benefits for depositing ultra-thin layers, the high substrate temperature required to initiate the surface chemical reactions is a major disadvantage for substrates with pre-existing ultra-thin-film coatings. Even in the case of ALD, substrate temperatures are typically in the range of 150° C – 400° C, which can lead to strong interdiffusion in the pre-existing ultra-thin layers on the substrate. Moreover, the range of materials that can be deposited by CVD is restricted by the availability of precursors with required chemical properties. Therefore, CVD methods are preferred for uniform and conformal single layer coatings, but they are not suitable for depositing multi-layered structures with sharp interfaces and several material combinations. CVD methods are predominantly used in applications that require thin-film coating of non-planar surfaces, as in the case of corrosion-resistant coatings of hardware components, catalyst coatings, metal and dielectric layers in integrated circuit and memory devices.[25]

Physical vapor deposition[22] is a process in which a target material in a condensed state is converted into a vapor phase through evaporation, sublimation, or sputtering process, followed by

condensation of the vapor material on to a substrate in order to form a thin-film coating. The atoms ejected out of the target are highly directional, and therefore, the substrate is placed in front of the target at close proximity. This means that PVD is a line-of-sight deposition process that cannot be used to deposit conformal and uniform thin films over uneven substrate topographies, though some process variants can well increase the lateral thickness uniformity across the substrate area. One of the main advantages of PVD over CVD is the low-substrate temperature required for deposition. The substrate can in principle remain near room temperature during deposition because the PVD process does not depend on activation of surface chemical reactions for the deposition process to occur. This is highly beneficial for applications that require coating of multiple ultra-thin films in a single coating procedure, without damaging the pre-existing layers. Moreover, it is possible to deposit a wide range of materials, including compounds and alloys, by choosing the right target composition.

The commonly used PVD methods are thermal evaporation, electron beam (e-beam) evaporation, pulsed layer deposition (PLD), and sputter deposition.[22,27–29] In thermal and e-beam evaporation techniques, atoms from the target material are ejected through an evaporation (or sublimation) process caused by resistive heating (thermal) or a focused high-energy e-beam. Evaporation-based techniques require a high-vacuum environment during deposition to avoid contamination and to minimize collision with background gas atoms before condensation on the substrate. The evaporated target atoms have a low kinetic energy, typically in the order of 0.1 eV; however, contribution from thermal radiation can be significant depending on the substrate-target distance.[29] On the one hand, the low kinetic energy of atoms arriving at the surface can be favorable in terms of limiting intermixing or physical damage to the previously deposited layer. On the other hand, as a consequence of low adatom mobility, the deposited layer tends to have high roughness and low bulk density. For this reason, additional energy in the form of substrate heating or low-energy (50-100 eV) ion bombardment may be required during deposition to improve the layer quality.[29] The main advantage of evaporation methods is the simple chamber design and process requirements, which makes them suitable for high-volume manufacturing of ultra-thin film coatings. The drawback is usually in the form of compromises in film quality and thickness control. The applications of evaporation methods are mainly in the fields of optical and mechanical coatings.[29]

In the PLD technique,[29,30] short pulses of a high-power laser beam ablate a target, and the ablated material in the form of a vapor plume is collected on to the substrate to grow the desired film. The advantages of the PLD technique are: high deposition rate (in the order of tens of nm per pulse), high-quality dense films, film stoichiometry is similar to that of target, and a wide range of materials can be deposited. However, the main challenge of PLD for depositing ultra-thin film layers is the production of nano- and micro-sized particles during the ablation process that can potentially be incorporated into the growing film.[31] Nevertheless, PLD is a fast-growing deposition technique used

in a wide range of optical, mechanical, and superconducting applications, for coating tens or hundreds of nanometers thick oxides and nitrides of ternary or more complex alloys with desired stoichiometry.[30]

Unlike previously discussed PVD methods, the technique of sputter deposition[28,32] does not involve evaporation or sublimation or ablation of target material, but rather physical sputtering of target atoms caused by bombardment of positively charged noble gas ions (e.g. Ar^+ or Kr^+) either from an ion beam source or from a plasma generated close to a negatively charged target. The sputtered atoms are deposited on to the substrate placed in the vicinity to produce the desired thin film. In magnetron sputtering deposition (MSD) technique, a closed magnetic field is used to confine electrons near the target, and thus, allowing to generate a well confined high-density plasma even in low background gas pressure (10^{-3} to 10^{-4} mbar). This background pressure (sputter gas pressure) in magnetron sputtering is ~ two orders of magnitude higher than evaporation-based techniques, and therefore the mean-free-path of the sputtered atoms is usually only a few centimeters. The kinetic energy of the deposited atoms is typically in range of 1-10 eV depending on the number of collisions before arriving at the substrate, which depends on the substrate-to-target distance and sputter gas pressure.[28] This kinetic energy results in a high adatom surface mobility that is required for the growth of high-density films with low surface roughness, However, the undesirable consequence of high energy incoming atoms is the ballistic intermixing with previous layers, which leads to a thick interface (intermixed zone) between consecutive layers in a thin-film stack.[33] Nevertheless, this can be partially reduced by controlling the particle energy, by tuning the background pressure and sputter conditions. The advantages of MSD technique are the possibility to obtain a high-quality film, excellent thickness accuracy, ability to use a wide range of materials, and a good uniformity over a large substrate area by controlling substrate rotation and movement over target. The disadvantages of MSD are the relatively low deposition rate for some dielectric materials, lower suitability for deposition of complex alloys with desired stoichiometry, and poor conformality. The MSD technique is used in a broad range of industries such as microelectronics, optics, biomedical, mechanical, and aerospace. Ion beam sputter deposition[32] (IBSD) uses a remote ion source instead of generating a plasma close to the target, which allows for a better control over sputter ion energy, ion density, and angle of incidence. Therefore, IBSD provides even better thickness and defects control when compared to MSD.

In summary, every deposition technique discussed in this section has its advantages and disadvantages. CVD and ALD techniques are generally preferred for non-planar surfaces and conformal coatings of high-aspect-ratio structures, whereas PVD techniques are preferred for deposition of high-quality films on planar-surfaces at low temperatures. The aim of this thesis is to understand the surface atomic diffusion processes involved during the growth of nanoscale-thin-films. This requires a growth technique like magnetron sputtering (MSD), which can produce high-quality films with low contaminations near-room temperature, in order to eliminate the contamination-induced

diffusion and temperature-induced bulk diffusion. Therefore, all thin-film systems studied in this work are deposited using the MSD technique.

1.3. SCOPE OF THE THESIS

1.3.1. Research Objectives

The two main phenomena that determine the quality of interfaces in nanoscale thin-film structures are: (i) intermixing with the substrate layer that occurs during layer growth, and (ii) thermally-activated interdiffusion between different layers in a thin-film stack that occurs during low-temperature annealing (100C – 300° C). In the case of magnetron sputtering deposition (MSD), the kinetic energy of sputtered atoms is high-enough to cause ballistic intermixing with the substrate layer even during deposition near room temperature. However, the kinetic energy of sputtered atoms is not the only parameter that determines the intermixing phenomenon during growth. Intermixing in some thin-film systems is significantly more than other systems deposited under similar conditions, which strongly indicates that intermixing during growth depends on material properties in addition to the deposition conditions.[33] The thermally-activated interdiffusion phenomenon depends primarily on the structural and material properties of the layers.[34]

Intermixing between layers during growth is commonly defined in terms of the effective interface width (σ) observed after deposition.[33,35,36] The interface width between two layers in a thin-film system is generally obtained from the experimental data using techniques, such as cross-sectional transmission electron microscopy (XTEM), X-ray reflectivity (XRR), and X-ray photoelectron spectroscopy (XPS).[8,34,36–40] It is common to explain intermixing as the drive to form interlayer compounds based on the enthalpy of compound formation.[20,21] This approach is however questionable because most depositions, especially MSD, are non-equilibrium processes. There are several reports in the literature that show asymmetric interfaces between two layers, where the interface width of an A-on-B bilayer system is significantly wider than of a B-on-A system.[33–35,37,41–45] The asymmetry in interfaces between two layer materials is commonly described using parameters such as deposition energy, atomic mass, layer crystallinity, and density and roughness of the constituent layers.[37,42,46,47] However, these factors cannot explain the difference in interface width values between different layer material combinations.[33] Intermixing between film and substrate layers is rarely explained in terms of layer-material-dependent surface atomic diffusion and surface exchange processes that occur during growth, which can possibly explain the difference in interface characteristics observed for different layer material combinations. Although there are several reports in the literature on activation energies for adatom hopping and surface diffusion obtained from advanced computer calculations,[48–53] it is not possible to make a quantitative predictive model for effective interface width based on these values. Also, it is extremely time consuming to simulate the entire deposition process involving several nanometer thick layers.

From the basic science point of view, it is crucial to understand the surface diffusion mechanisms involved during a non-equilibrium process like deposition. From the industrial application point of view, using that fundamental knowledge to develop a generic model that has the ability to predict the growth and interface characteristics of ultra-thin films, can be highly beneficial for designing a thin-film stack with the most suitable layer material combination, especially when sub-nanometer thick interlayers have to be included in the stack design. This forms the basis for the first objective of this thesis:

***Objective 1**: Identify fundamental material properties that drive the surface atomic diffusion and exchange processes during growth, and develop a theoretical model and an experimental database, which can serve as a tool to quantitatively estimate the layer growth and interface characteristics of ultra-thin film systems.*

When it comes to thermally-activated interdiffusion phenomena, the common approach is to define interdiffusion between layers in terms of the activation energy for diffusion.[54] However, in the case ultra-thin film layers, a wide range of activation energy values can be found in the literature for a given thin-film system because of its dependence on layer thicknesses, structural properties, and deposition conditions.[54–56] Therefore, it is essential to understand the role of layer structural properties (grain boundaries, density, roughness) and layer material properties (atomic size, mixing energy) in thermally-activated interdiffusion phenomenon. A generic model based on layer properties that can, at least, qualitatively predict the interdiffusion phenomena will be useful in improving the thermal stability of the thin-film stack. It is important to realize that high-temperature (> 300° C) annealing can lead to significant structural changes (phase transition, crystallization), which can influence and also be influenced by the interdiffusion process. For this reason, the scope of this thesis is limited to investigating interdiffusion in layered systems during low temperature annealing (< 300° C). This is the second objective of this thesis:

***Objective 2**: Identify key layer structural and material properties that drive the interdiffusion process at interfaces during low temperature annealing of ultra-thin-film systems, or in other words, layer properties that determine the thermal stability.*

1.3.2. Methodology

In order to understand intermixing and surface diffusion processes, it is important to be able to precisely measure the surface composition changes during layer growth. This is not possible using conventional analysis techniques, such as cross-sectional transmission electron microscopy (XTEM), X-ray reflectivity (XRR), and X-ray photoelectron spectroscopy (XPS), because of low surface-to-bulk signal ratio. An analysis technique with high surface sensitivity, like low-energy ion scattering (LEIS), is required for this purpose. LEIS is commonly used for characterizing the surface and

subsurface atomic composition in nanoscale thin films,[57–60] and it is widely used for studying the layer closure and nucleation behavior during growth of ultra-thin films.[61–63] In LEIS, low-energy noble gas ions with kinetic energy in the range of 1 keV to 8 keV are directed toward the sample at a certain incidence angle, as shown in Figure 1.2a. By measuring the kinetic energy of the backscattered ions (not neutrals), the mass of the scattering atoms can be calculated according to the law of conservation of mass and energy. Primary ions that are backscattered from the surface atoms contribute to the surface peak (Figure 1.2b) in the LEIS spectrum. Primary ions that penetrate into subsurface layers are immediately neutralized because of the high neutralization probability of low-energy ions. This means that the primary neutrals, that are backscattered from the subsurface layers, have to be re-ionized at the surface before they can be detected. The re-ionization probability of backscattered neutrals at the surface is considerably low in general and it depends on the material and surface composition. The primary neutrals that are backscattered from subsurface layers and reionized at the surface contribute to the low-energy tail (Figure 1.2b) because of the loss in energy while moving through the subsurface layers. The final kinetic energy of the ions backscattered from subsurface layers depends on the penetration depth, where primary ions backscattered from deeper layers have lower energy. Overall, the high neutralization probability coupled with low re-ionization probability results in a high surface-to-bulk signal ratio, which is the fundamental reason for the high surface sensitivity of LEIS technique.

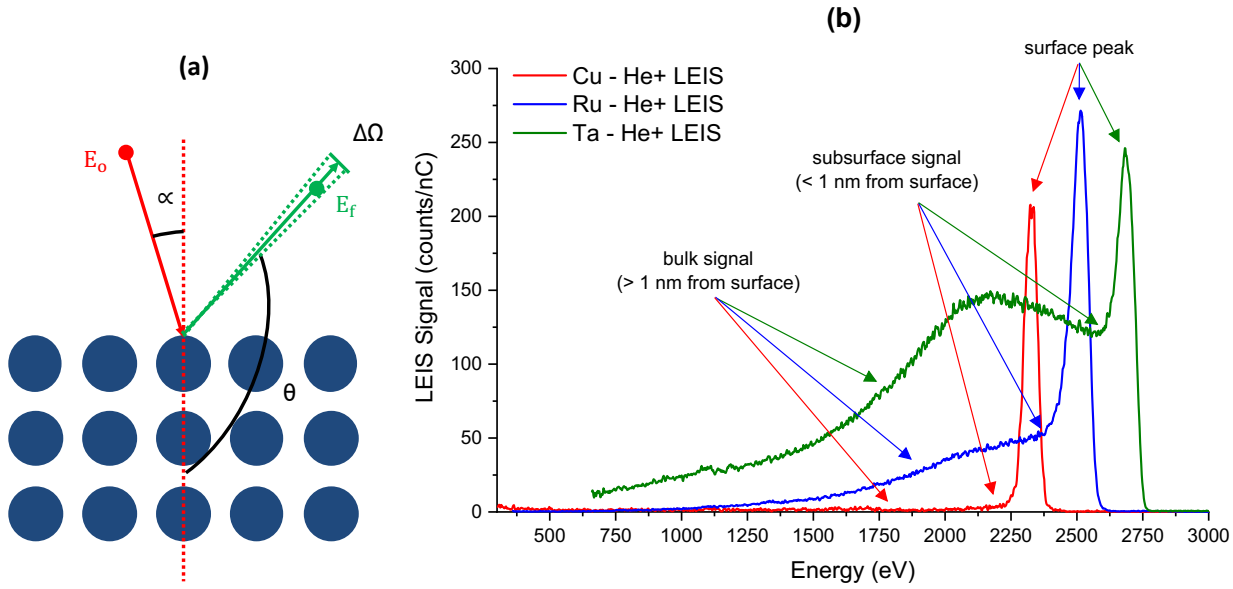

Figure 1.2. (a) schematic representation of ion scattering during LEIS, (b) 3 keV He+ LEIS spectra of Cu, Ru, and Ta

In this thesis work, an IONTOF Qtac[100] tool is used for high sensitivity low energy ion scattering (HS-LEIS) measurements. HS-LEIS has orders of magnitude higher signal-to-primary ion current ratio when compared to conventional LEIS because the scattered ions are collected over all azimuth angles at the desired scattering angle.[60] Therefore, it is sufficient to use a low primary ion current to obtain a good LEIS spectrum, which reduces the primary-ion-induced damage to the sample

surface. The primary-ion-induced sputtering of surface atoms is expected to be less than 0.5% of a monolayer for a standard HS-LEIS measurement.[60] This enables the measurement of surface composition without significantly altering the surface during measurement.

Typical LEIS spectra are shown in Figure 1.2b. In the ideal case, the neutralization probability of an incident ion scattering from a surface atom is not influenced by the matrix or the presence of other neighboring atoms in the sample. Therefore, the surface composition can be quantified by comparing the LEIS surface peak signal of the investigated sample and the pure reference sample. In rare cases, the so-called matrix effect is observed, where the neutralization probability, and thus the intensity of the LEIS signal, depends on the matrix or the neighboring atoms.[59,64–66] For such cases, quantification of surface composition becomes extremely complex. Also, if the reference sample deviates considerably from the investigated sample in terms of surface roughness, contamination, crystallinity and surface orientation, the quantification of the surface composition will not be reliable. In order to obtain meaningful surface quantification from the LEIS data and for the sake of simplifying LEIS analysis, all material combinations investigated in this work are verified to have no matrix effect (linear change in LEIS signal with atomic concentration),[59] and relevant reference samples are prepared for each material combination studied in this work to avoid significant deviation in roughness and crystallinity.

In this work, the surface composition analysis is done by calculating the surface coverage (θ) of an element in a bielement system using the expression:

$$\theta = \frac{Surface\ peak\ area\ of\ an\ element\ in\ the\ investigated\ bielement\ sample}{Surface\ peak\ area\ of\ an\ element\ in\ the\ pure\ reference\ sample}. \qquad (1)$$

It is important to note that the variable θ simply indicates the number of surface atoms per unit area of an element in the bielement system when compared to the pure reference of that element, and it does not represent the surface atomic fraction of an element in the bielement system, (i.e.) fraction of atoms of an element in the total number of atoms per unit area. A bielement system in which the number of surface atoms per unit area of the mixture (A+B) is similar to that of the pure elements (A, B), $\theta_{Total} = \theta_A + \theta_B \cong 1$, and θ of an element also indicates the surface atomic fraction of that element. However, when the number of surface atoms per unit area of the mixture is significantly different from that of pure elements, which is most likely the case when the elements have a large difference in atomic size or surface atomic density, $\theta_{Total} > 1$, and θ of an element does not represent its surface atomic fraction. Because of the intrinsic surface sensitivity of LEIS, surface contamination as a result of exposure to atmosphere during ex-situ sample handling can strongly affect the surface composition analysis. Any kind of surface cleaning procedure to remove surface contamination before LEIS measurement will generally alter the surface under investigation, which is not desirable. For this

reason, all layer growth studies reported in this thesis are done in an ultra-high vacuum (UHV) cluster set up available at the Industrial Focus Group XUV Optics (Figure 1.3), consisting of a magnetron sputtering deposition chamber (Atomic Growth and Analysis – AGA), and the facility to transfer samples *in vacuo* (~ 5 x 10^{-10} mbar) to a HS-LEIS tool for surface composition analysis and to an XPS tool for chemical bonding and composition analysis. The *in vacuo* sample transfer procedure, with a transfer time of typically 7 – 10 mins, can significantly limit surface contamination to less than the detectable limit of LEIS, (i.e.) less than 1% surface coverage. The UHV cluster set up provides the possibility to measure surface composition changes after every sub-nanometer growth step. Further information on the deposition chamber, LEIS/XPS tools, and process methodology are provided in the main chapters.

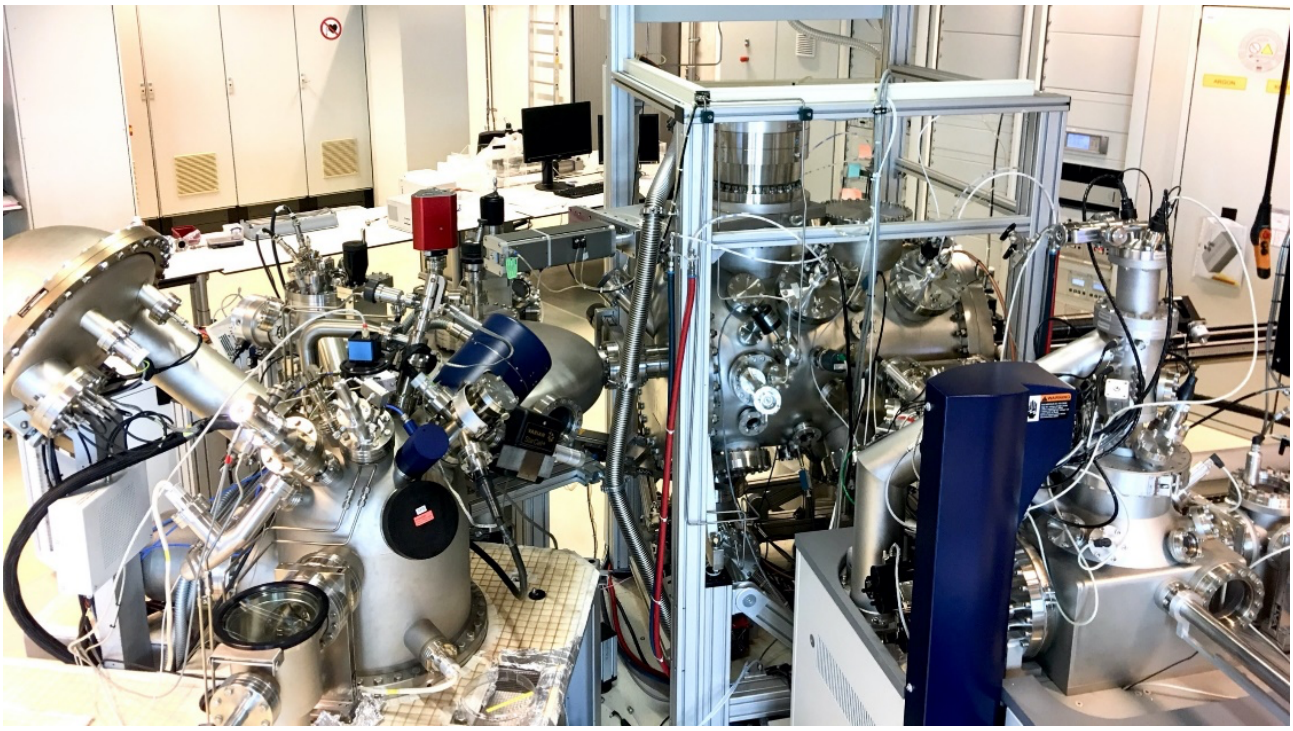

Figure 1.3. UHV cluster set up at the Industrial Focus Group XUV Optics, University of Twente

For thermally-activated interdiffusion studies, it is important to be able to measure the changes at the interfaces between two layers after annealing. Conventional techniques such as XTEM and XRR are the preferred analysis tools for this purpose. Because these analysis techniques require ex-situ sample transfer, a multilayer structure is used instead of a bilayer or trilayer architecture, in order to avoid the effect of surface oxidation and contamination, and also to mitigate the damage caused by sample preparation for XTEM. The AGA system is not suitable for the deposition of repetitive layers, as in the case of a multilayer structure, because of the slow linear movement of the arm carrying the sample stage. For this reason, the multilayer structures used in this work are produced using a Roth & Rau MS1600 deposition system available at the Industrial Focus Group XUV Optics. The deposition

conditions, such as sputter voltage, sputter gas, pressure, and substrate-to-target distance, of AGA and MS1600 systems are similar to each other.

An overview of all analysis tools used in this thesis work is given in Table 1.1. All necessary information regarding the methodology, process conditions, and analysis tools, required to comprehend the reported results are provided in the main chapters. For detailed information on principles, instrumentations, and data interpretation of the analysis tools, readers are kindly directed to the respective literature given in the table below.

Table 1.1. Overview of all analysis tools used in this thesis

TOOL	TARGET	PROBE	INFORMATION OBTAINED	FURTHER READING
Low-energy ion scattering (LEIS)	Surface	Low-energy noble gas ions	Surface composition	57,59,67
Cross-sectional transmission electron microscope (XTEM)	Bulk layer and interfaces	Electrons	Magnified images of ultra-thin layers and interfaces, crystallinity	68
X-ray Photoelectron Spectroscopy (XPS)	Surface, bulk layer, and interfaces	X-rays	Elemental composition and chemical interaction	69
X-ray reflectivity (XRR)	Surface, bulk layer, and interfaces	X-rays	Layer thickness, period thickness in multilayer structure, surface and interface roughness	67
Grazing incidence X-ray diffraction (GIXRD)	Bulk layer	X-rays	Layer crystallinity and orientations	67,70
Atomic Force Microscope (AFM)	Surface	High-resolution cantilever tip	Surface roughness, surface topography image	67

1.3.3. Thesis Outline

The results of this work are presented in chapters 2 to 5. Chapters 2 and 3 address *objective-1* of this thesis: intermixing during layer growth, and, chapters 4 and 5 address *objective-2*: interdiffusion between layers during low-temperature annealing. The chapter-by-chapter outline and the conclusions of this work are presented in Table 1.2.

Table 1.2. Chapter-by-Chapter outline and conclusions

RESEARCH OBJECTIVE	CHAPTER	MATERIAL SYSTEM	OUTLINE	CONCLUSIONS
Objective-1 *Intermixing during layer growth*	2	TM-on-TM (bilayer)	• A semi-empirical model is presented to describe the surface (atomic) exchange processes during layer growth based on the surface energy difference between film and substrate atoms • TM-on-TM systems are categorized into four growth types depending on the observed intermixing and segregation behavior	• The semi-empirical model acts as a scaling law to predict the effective interface widths of TM-on-TM, TM-on-Si systems in general • Based on the experimental data, general rules are suggested to predict the layer growth characteristics such as segregation, island formation
	3	TM-on-Si Ru-on-Al (bilayer)	• Applicability of scaling law for interface width and layer growth rules for most investigated TM-on-Si systems and Ru-on-Al system is discussed	
Objective-2 *Interdiffusion between layers during low-temperature annealing*	4	Nb-Si (bilayer and multilayer)	• Nb is shown to exhibit two microstructural transitions during Nb-on-Si growth • The effect of Nb layer microstructure on interlayer diffusion during low-temperature annealing in Nb/Si multilayer systems is presented	• Large atomic size difference between the layer materials can result in solid state amorphization and complete intermixing of layers during low-temperature annealing, and in some cases at near room temperature • Interlayer diffusion can be strongly reduced by limiting the number of grain boundary and interstitial pathways for diffusion
	5	Zr-Si (bilayer and multilayer)	• The solid state amorphization of Zr layers in Zr/Si multilayers during low-temperature annealing is discussed • The effect of atomic size difference between layer materials is shown to strongly affect the thermal stability of the multilayer stack	

1.4. REFERENCES

(1) Fang, F. Atomic and Close-to-Atomic Scale Manufacturing: Perspectives and Measures. *Int. J. Extrem. Manuf.* **2020**, *2* (3), 030201. https://doi.org/10.1088/2631-7990/aba495.

(2) Stoian, M.; Maurer, T.; Lamri, S.; Fechete, I. Techniques of Preparation of Thin Films: Catalytic Combustion. *Catalysts* **2021**, *11* (12), 1–32. https://doi.org/10.3390/catal11121530.

(3) Seo, H. G.; Choi, Y.; Koo, B.; Jang, A.; Jung, W. Robust Nano-Architectured Composite Thin Films for a Low-Temperature Solid Oxide Fuel Cell Cathode. *J. Mater. Chem. A* **2016**, *4* (24), 9394–9402. https://doi.org/10.1039/c6ta00052e.

(4) Biener, J.; Wittstock, A.; Baumann, T.; Weissmüller, J.; Bäumer, M.; Hamza, A. Surface Chemistry in Nanoscale Materials. *Materials (Basel).* **2009**, *2* (4), 2404–2428. https://doi.org/10.3390/ma2042404.

(5) Abdulagatov, A. I.; Yan, Y.; Cooper, J. R.; Zhang, Y.; Gibbs, Z. M.; Cavanagh, A. S.; Yang, R. G.; Lee, Y. C.; George, S. M. Al2O3 and TiO2 Atomic Layer Deposition on Copper for Water Corrosion Resistance. *ACS Appl. Mater. Interfaces* **2011**, *3* (12), 4593–4601. https://doi.org/10.1021/am2009579.

(6) Kuznetsov, D.; Yakshin, A.; Sturm, M.; van de Kruijs, R.; Louis, E.; Bijkerk, F. High-Reflectance La/B-Based Multilayer Mirror for 6.x-Nm Wavelength. In *Advances in X-Ray/EUV Optics and Components X*; Goto, S., Morawe, C., Khounsary, A. M., Eds.; 2015; Vol. 9588, p 958806. https://doi.org/10.1117/12.2199427.

(7) Vávra, I.; Lobotka, P.; Dérer, J.; Wellenberg, L. R. Structural and Electrical Properties of Superconducting Nb/Si Multilayers. *Vacuum* **1998**, *50* (1–2), 31–33. https://doi.org/10.1016/S0042-207X(98)00009-8.

(8) Haase, A.; Bajt, S.; Hönicke, P.; Soltwisch, V.; Scholze, F. Multiparameter Characterization of Subnanometre Cr/Sc Multilayers Based on Complementary Measurements. *J. Appl. Crystallogr.* **2016**, *49* (6), 2161–2171. https://doi.org/10.1107/S1600576716015776.

(9) Park, S.; Han, U.; Choi, D.; Hong, J. Layer-by-Layer Assembled Polymeric Thin Films as Prospective Drug Delivery Carriers: Design and Applications. *Biomater. Res.* **2018**, *22* (1), 29. https://doi.org/10.1186/s40824-018-0139-5.

(10) Senthil, R.; Yuvaraj, S. A Comprehensive Review on Bioinspired Solar Photovoltaic Cells. *Int. J. Energy Res.* **2019**, *43* (3), 1068–1081. https://doi.org/10.1002/er.4255.

(11) Zhang, H.; Ly, K. C. S.; Liu, X.; Chen, Z.; Yan, M.; Wu, Z.; Wang, X.; Zheng, Y.; Zhou, H.; Fan, T. Biologically Inspired Flexible Photonic Films for Efficient Passive Radiative Cooling.

Proc. Natl. Acad. Sci. U. S. A. **2020**, *117* (26), 14657–14666. https://doi.org/10.1073/pnas.2001802117.

(12) Motamedi, M.; Warkiani, M. E.; Taylor, R. A. Transparent Surfaces Inspired by Nature. *Adv. Opt. Mater.* **2018**, *6* (14), 1–28. https://doi.org/10.1002/adom.201800091.

(13) He, J.; Song, C.; Shan, H.; Jiang, Y.; Zhou, L.; Tao, P.; Wu, J.; Shang, W.; Deng, T. Bioinspired Color Change through Guided Reflection. *Adv. Opt. Mater.* **2018**, *6* (24), 1–8. https://doi.org/10.1002/adom.201800464.

(14) Sakhonenkov, S. S.; Filatova, E. O. Nanoscale W/Be Multilayers: Intermixing during Magnetron Sputtering Deposition and Effect of Heat Treatment. *Appl. Surf. Sci.* **2022**, *571* (September 2021), 151265. https://doi.org/10.1016/j.apsusc.2021.151265.

(15) Nedelcu, I.; van de Kruijs, R. W. E.; Yakshin, A. E.; Tichelaar, F.; Zoethout, E.; Louis, E.; Enkisch, H.; Muellender, S.; Bijkerk, F. Interface Roughness in Mo/Si Multilayers. *Thin Solid Films* **2006**, *515* (2 SPEC. ISS.), 434–438. https://doi.org/10.1016/j.tsf.2005.12.168.

(16) Trost, M.; Schröder, S.; Yulin, S.; Duparré, A. Roughness Evolution of Multilayer Coatings for 6.7 Nm and Its Impact on Light Scattering. In *Optical Interference Coatings 2016*; OSA: Washington, D.C., 2016; p TA.2. https://doi.org/10.1364/OIC.2016.TA.2.

(17) Loubet, N.; Hook, T.; Montanini, P.; Yeung, C.-W.; Kanakasabapathy, S.; Guillom, M.; Yamashita, T.; Zhang, J.; Miao, X.; Wang, J.; et al. Stacked Nanosheet Gate-All-around Transistor to Enable Scaling beyond FinFET. In *2017 Symposium on VLSI Technology*; IEEE, 2017; Vol. 5, pp T230–T231. https://doi.org/10.23919/VLSIT.2017.7998183.

(18) Barraud, S.; Lapras, V.; Previtali, B.; Samson, M. P.; Lacord, J.; Martinie, S.; Jaud, M.-A.; Athanasiou, S.; Triozon, F.; Rozeau, O.; et al. Performance and Design Considerations for Gate-All-around Stacked-NanoWires FETs. In *2017 IEEE International Electron Devices Meeting (IEDM)*; IEEE, 2017; pp 29.2.1-29.2.4. https://doi.org/10.1109/IEDM.2017.8268473.

(19) De Rooij-Lohmann, V. I. T. A.; Veldhuizen, L. W.; Zoethout, E.; Yakshin, A. E.; Van De Kruijs, R. W. E.; Thijsse, B. J.; Gorgoi, M.; Schäfers, F.; Bijkerk, F. Chemical Interaction of B4 C, B, and C with Mo/Si Layered Structures. *J. Appl. Phys.* **2010**, *108* (9). https://doi.org/10.1063/1.3503521.

(20) Kuznetsov, D. S.; Yakshin, A. E.; Sturm, J. M.; Van De Kruijs, R. W. E.; Bijkerk, F. Structure of High-Reflectance La/B-Based Multilayer Mirrors with Partial La Nitridation. *AIP Adv.* **2016**, *6* (11). https://doi.org/10.1063/1.4968175.

(21) Tsarfati, T.; Van De Kruijs, R. W. E.; Zoethout, E.; Louis, E.; Bijkerk, F. Nitridation and

Contrast of B4C/La Interfaces and X-Ray Multilayer Optics. *Thin Solid Films* **2010**, *518* (24), 7249–7252. https://doi.org/10.1016/j.tsf.2010.04.088.

(22) Chapter 1 - Deposition Technologies: An Overview. In *Handbook of Deposition Technologies for Films and Coatings (Third Edition)*; Martin, P. M., Ed.; William Andrew Publishing: Boston, 2010; pp 1–31. https://doi.org/https://doi.org/10.1016/B978-0-8155-2031-3.00001-6.

(23) Gamburg, Y. D.; Zangari, G. Introduction to Electrodeposition: Basic Terms and Fundamental Concepts. In *Theory and Practice of Metal Electrodeposition*; Springer New York: New York, NY, 2011; pp 1–25. https://doi.org/10.1007/978-1-4419-9669-5_1.

(24) Tufail Chaudhary, K. Thin Film Deposition: Solution Based Approach. In *Thin Films*; IntechOpen, 2021; p 13. https://doi.org/10.5772/intechopen.94455.

(25) Carlsson, J.-O.; Martin, P. M. Chapter 7 - Chemical Vapor Deposition. In *Handbook of Deposition Technologies for Films and Coatings (Third Edition)*; Martin, P. M., Ed.; William Andrew Publishing: Boston, 2010; pp 314–363. https://doi.org/https://doi.org/10.1016/B978-0-8155-2031-3.00007-7.

(26) Pakkala, A.; Putkonen, M. Chapter 8 - Atomic Layer Deposition. In *Handbook of Deposition Technologies for Films and Coatings (Third Edition)*; Martin, P. M., Ed.; William Andrew Publishing: Boston, 2010; pp 364–391. https://doi.org/https://doi.org/10.1016/B978-0-8155-2031-3.00008-9.

(27) Shah, S. I.; Jaffari, G. H.; Yassitepe, E.; Ali, B. Chapter 4 - Evaporation: Processes, Bulk Microstructures, and Mechanical Properties. In *Handbook of Deposition Technologies for Films and Coatings (Third Edition)*; Martin, P. M., Ed.; William Andrew Publishing: Boston, 2010; pp 135–252. https://doi.org/https://doi.org/10.1016/B978-0-8155-2031-3.00004-1.

(28) Depla, D.; Mahieu, S.; Greene, J. E. Chapter 5 - Sputter Deposition Processes. In *Handbook of Deposition Technologies for Films and Coatings (Third Edition)*; Martin, P. M., Ed.; William Andrew Publishing: Boston, 2010; pp 253–296. https://doi.org/https://doi.org/10.1016/B978-0-8155-2031-3.00005-3.

(29) Ohring, M. Chapter 3 - Thin-Film Evaporation Processes. In *Materials Science of Thin Films (Second Edition)*; Ohring, M., Ed.; Academic Press: San Diego, 2002; pp 95–144. https://doi.org/https://doi.org/10.1016/B978-012524975-1/50006-9.

(30) *Pulsed Laser Deposition of Thin Films*; Eason, R., Ed.; John Wiley & Sons, Inc.: Hoboken, NJ, USA, 2006. https://doi.org/10.1002/0470052120.

(31) Prentice, J. J.; Grant-Jacob, J. A.; Kurilchik, S. V.; Mackenzie, J. I.; Eason, R. W. Particulate

Reduction in PLD-Grown Crystalline Films via Bi-Directional Target Irradiation. *Appl. Phys. A* **2019**, *125* (2), 152. https://doi.org/10.1007/s00339-019-2456-5.

(32) Mattox, D. M. Physical Sputtering and Sputter Deposition (Sputtering). In *Handbook of Physical Vapor Deposition (PVD) Processing*; Mattox, D. M., Ed.; Elsevier: Boston, 2010; pp 237–286. https://doi.org/10.1016/B978-0-8155-2037-5.00007-1.

(33) Chandrasekaran, A.; van de Kruijs, R. W. E.; Sturm, J. M.; Zameshin, A. A.; Bijkerk, F. Nanoscale Transition Metal Thin Films: Growth Characteristics and Scaling Law for Interlayer Formation. *ACS Appl. Mater. Interfaces* **2019**, *11* (49), 46311–46326. https://doi.org/10.1021/acsami.9b14414.

(34) Chandrasekaran, A.; van de Kruijs, R. W. E.; Sturm, J. M.; Bijkerk, F. Nb Texture Evolution and Interdiffusion in Nb/Si-Layered Systems. *ACS Appl. Mater. Interfaces* **2021**, *13* (26), 31260–31270. https://doi.org/10.1021/acsami.1c06210.

(35) Coloma Ribera, R.; van de Kruijs, R. W. E.; Sturm, J. M.; Yakshin, A. E.; Bijkerk, F. In Vacuo Growth Studies of Ru Thin Films on Si, SiN, and SiO 2 by High-Sensitivity Low Energy Ion Scattering. *J. Appl. Phys.* **2016**, *120* (6), 065303. https://doi.org/10.1063/1.4960577.

(36) Windt, D. L. IMD—Software for Modeling the Optical Properties of Multilayer Films. *Comput. Phys.* **1998**, *12* (4), 360. https://doi.org/10.1063/1.168689.

(37) Windt, D. L.; Christensen, F. E.; Craig, W. W.; Hailey, C.; Harrison, F. A.; Jimenez-Garate, M.; Kalyanaraman, R.; Mao, P. H. Growth, Structure, and Performance of Depth-Graded W/Si Multilayers for Hard x-Ray Optics. *J. Appl. Phys.* **2000**, *88* (1), 460–470. https://doi.org/10.1063/1.373681.

(38) Zameshin, A.; Makhotkin, I. A.; Yakunin, S. N.; van de Kruijs, R. W. E.; Yakshin, A. E.; Bijkerk, F. Reconstruction of Interfaces of Periodic Multilayers from X-Ray Reflectivity Using a Free-Form Approach. *J. Appl. Crystallogr.* **2016**, *49* (4), 1300–1307. https://doi.org/10.1107/S160057671601044X.

(39) Filatova, E. O.; Sakhonenkov, S. S.; Gaisin, A. U.; Konashuk, A. S.; Chumakov, R. G.; Pleshkov, R. S.; Chkhalo, N. I. Inhibition of Chemical Interaction of Molybdenum and Silicon in a Mo/Si Multilayer Structure by the Formation of Intermediate Compounds. *Phys. Chem. Chem. Phys.* **2021**, *23* (2), 1363–1370. https://doi.org/10.1039/d0cp05180b.

(40) De Rooij-Lohmann, V. I. T. A.; Veldhuizen, L. W.; Zoethout, E.; Yakshin, A. E.; Van De Kruijs, R. W. E.; Thijsse, B. J.; Gorgoi, M.; Schäfers, F.; Bijkerk, F. Chemical Interaction of B4 C, B, and C with Mo/Si Layered Structures. *J. Appl. Phys.* **2010**, *108* (9), 1–6. https://doi.org/10.1063/1.3503521.

(41) Fullerton, E. E.; Pearson, J.; Sowers, C. H.; Bader, S. D.; Wu, X. Z.; Sinha, S. K. Interfacial Roughness of Sputtered Multilayers: Nb/Si. *Phys. Rev. B* **1993**, *48* (23), 17432–17444. https://doi.org/10.1103/PhysRevB.48.17432.

(42) Bajt, S.; Stearns, D. G.; Kearney, P. A. Investigation of the Amorphous-to-Crystalline Transition in Mo/Si Multilayers. *J. Appl. Phys.* **2001**, *90* (2), 1017–1025. https://doi.org/10.1063/1.1381559.

(43) Smith, G. D. W. D. W.; Larson, D. J. J.; Johnson, R. A. A.; Zhou, X. W. W.; Petford-Long, A. K. K.; Kelly, T. F. F.; Cerezo, A.; Wadley, H. N. G. N. G.; Tabat, N.; Martens, R. L. L.; et al. Atomic Scale Structure of Sputtered Metal Multilayers. *Acta Mater.* **2001**, *49* (19), 4005–4015. https://doi.org/10.1016/S1359-6454(01)00287-7.

(44) Eberl, C.; Liese, T.; Schlenkrich, F.; Döring, F.; Hofsäss, H.; Krebs, H. U. Enhanced Resputtering and Asymmetric Interface Mixing in W/Si Multilayers. *Appl. Phys. A Mater. Sci. Process.* **2013**, *111* (2), 431–437. https://doi.org/10.1007/s00339-013-7587-5.

(45) Gupta, A.; Kumar, D.; Phatak, V. Asymmetric Diffusion at the Interfaces in Fe/Si Multilayers. *Phys. Rev. B - Condens. Matter Mater. Phys.* **2010**, *81* (15), 1–5. https://doi.org/10.1103/PhysRevB.81.155402.

(46) Li, H.; Zhu, J.; Wang, Z.; Song, Z.; Chen, H. Asymmetrical Diffusion at Interfaces of Mg/SiC Multilayers. *Opt. Mater. Express* **2013**, *3* (5), 546. https://doi.org/10.1364/ome.3.000546.

(47) Nedelcu, I.; Van De Kruijs, R. W. E.; Yakshin, A. E.; Bijkerk, F. Thermally Enhanced Interdiffusion in MoSi Multilayers. *J. Appl. Phys.* **2008**, *103* (8), 1–6. https://doi.org/10.1063/1.2907964.

(48) Zhou, X. W.; Wadley, H. N. G. Atomistic Simulations of the Vapor Deposition of Ni/Cu/Ni Multilayers: The Effects of Adatom Incident Energy. *J. Appl. Phys.* **1998**, *84* (4), 2301–2315. https://doi.org/10.1063/1.368297.

(49) Zhou, X. W.; Wadley, H. N. G. Hyperthermal Vapor Deposition of Copper: Athermal and Biased Diffusion Effects. *Surf. Sci.* **1999**, *431* (1–3), 42–57. https://doi.org/10.1016/S0039-6028(99)00335-0.

(50) Gilmore, C. M.; Sprague, J. A. Molecular-dynamics Study of Film Growth with Energetic Ag Atoms. *J. Vac. Sci. Technol. A Vacuum, Surfaces, Film.* **2002**, *10* (4), 1597–1599. https://doi.org/10.1116/1.578050.

(51) Villarba, M.; Jónsson, H. Atomic Exchange Processes in Sputter Deposition of Pt on Pt(111). *Surf. Sci.* **1995**, *324* (1), 35–46. https://doi.org/10.1016/0039-6028(94)00631-8.

(52) Evans, J. W.; Sanders, D. E.; Thiel, P. A.; DePristo, A. E. Low-Temperature Epitaxial Growth of Thin Metal Films. *Phys. Rev. B* **1990**, *41* (8), 5410–5413. https://doi.org/10.1103/PhysRevB.41.5410.

(53) Roling, L. T.; Mavrikakis, M. Toward Rational Nanoparticle Synthesis: Predicting Surface Intermixing in Bimetallic Alloy Nanocatalysts. *Nanoscale* **2017**, *9* (39), 15005–15017. https://doi.org/10.1039/C7NR04779G.

(54) Bosgra, J.; Verhoeven, J.; Van De Kruijs, R. W. E.; Yakshin, A. E.; Bijkerk, F. Non-Constant Diffusion Characteristics of Nanoscopic Mo-Si Interlayer Growth. *Thin Solid Films* **2012**, *522*, 228–232. https://doi.org/10.1016/j.tsf.2012.08.051.

(55) Nakajima, H.; Fujimori, H.; Koiwa, M. Interdiffusion and Structural Relaxation in Mo/Si Multilayer Films. *J. Appl. Phys.* **1988**, *63* (4), 1046–1051. https://doi.org/10.1063/1.340005.

(56) Bruijn, S.; Van De Kruijs, R. W. E.; Yakshin, A. E.; Bijkerk, F. In-Situ Study of the Diffusion-Reaction Mechanism in Mo/Si Multilayered Films. *Appl. Surf. Sci.* **2011**, *257* (7), 2707–2711. https://doi.org/10.1016/j.apsusc.2010.10.049.

(57) Brüner, P.; Grehl, T.; Brongersma, H.; Detlefs, B.; Nolot, E.; Grampeix, H.; Steinbauer, E.; Bauer, P. Thin Film Analysis by Low-Energy Ion Scattering by Use of TRBS Simulations. *J. Vac. Sci. Technol. A Vacuum, Surfaces, Film.* **2015**, *33* (1), 01A122. https://doi.org/10.1116/1.4901451.

(58) Dittmar, K.; Triyoso, D. H.; Erben, E.; Metzger, J.; Binder, R.; Brongersma, H. H.; Weisheit, M.; Engelmann, H.-J. The Application of Low Energy Ion Scattering Spectroscopy (LEIS) in Sub 28-Nm CMOS Technology. *Surf. Interface Anal.* **2017**, *49* (12), 1175–1186. https://doi.org/10.1002/sia.6312.

(59) Brongersma, H.; Draxler, M.; Deridder, M.; Bauer, P. Surface Composition Analysis by Low-Energy Ion Scattering. *Surf. Sci. Rep.* **2007**, *62* (3), 63–109. https://doi.org/10.1016/j.surfrep.2006.12.002.

(60) ter Veen, H. R. J.; Kim, T.; Wachs, I. E.; Brongersma, H. H. Applications of High Sensitivity-Low Energy Ion Scattering (HS-LEIS) in Heterogeneous Catalysis. *Catal. Today* **2009**, *140* (3–4), 197–201. https://doi.org/10.1016/j.cattod.2008.10.012.

(61) Singhania, R. M.; Price, H.; Kounga, V. Y.; Davis, B.; Brüner, P.; Thorpe, R.; Hynek, D. J.; Cha, J. J.; Strandwitz, N. C. Surface Characterization of Ultrathin Atomic Layer Deposited Molybdenum Oxide Films Using High-Sensitivity Low-Energy Ion Scattering. *J. Vac. Sci. Technol. A* **2021**, *39* (6), 063210. https://doi.org/10.1116/6.0001164.

(62) Werner, M.; Roberts, J. W.; Potter, R. J.; Dawson, K.; Chalker, P. R. Elucidation of ALD MgZnO Deposition Processes Using Low Energy Ion Scattering. *J. Vac. Sci. Technol. A Vacuum, Surfaces, Film.* **2018**, *36* (2), 02D406. https://doi.org/10.1116/1.5015958.

(63) Primetzhofer, D.; Markin, S. N.; Zeppenfeld, P.; Bauer, P.; Prusa, S.; Kolibal, M.; Sikola, T. Quantitative Analysis of Ultra Thin Layer Growth by Time-of-Flight Low Energy Ion Scattering. *Appl. Phys. Lett.* **2008**, *92* (1), 011929. https://doi.org/10.1063/1.2822816.

(64) Bruckner, B.; Bauer, P.; Primetzhofer, D. Neutralization of Slow Helium Ions Scattered from Single Crystalline Aluminum and Tantalum Surfaces and Their Oxides. *Surf. Sci.* **2020**, *691* (August 2019), 121491. https://doi.org/10.1016/j.susc.2019.121491.

(65) Kürnsteiner, P.; Steinberger, R.; Primetzhofer, D.; Goebl, D.; Wagner, T.; Druckmüllerova, Z.; Zeppenfeld, P.; Bauer, P. Matrix Effects in the Neutralization of He Ions at a Metal Surface Containing Oxygen. *Surf. Sci.* **2013**, *609*, 167–171. https://doi.org/10.1016/j.susc.2012.12.003.

(66) Zameshin, A. A.; Yakshin, A. E.; Sturm, J. M.; Brongerma, H. H.; Bijkerk, F. Double Matrix Effect in Low Energy Ion Scattering from La Surfaces. *Appl. Surf. Sci.* **2018**, *440*, 570–579. https://doi.org/10.1016/j.apsusc.2018.01.174.

(67) Bracco, G.; Holst, B. *Surface Science Techniques*; Springer Series in Surface Sciences; Springer: Berlin, Heidelberg, 2013; Vol. 51. https://doi.org/10.1007/978-3-642-34243-1.

(68) Egerton, R. F. *Physical Principles of Electron Microscopy*; Springer International Publishing: Cham, 2016. https://doi.org/10.1007/978-3-319-39877-8.

(69) Watts, J.; Wolstenholme, J. *An Introduction to Surface Analysis by XPS and AES*.

(70) Cullity, B. D. *Elements of X-Ray Diffraction*; Addison-Wesley series in metallurgy and materials; Addison-Wesley Publishing Company, 1978.

CHAPTER 2

Nanoscale Transition Metal Thin Films: Growth Characteristics and Scaling Law for Interlayer Formation

A comprehensive study on the growth of nanoscale transition metal – on – transition metal (TM-on-TM) systems is presented. The near room temperature intermixing and segregation phenomena during growth are studied *in vacuo* using high-sensitivity low energy ion scattering (HS-LEIS). The investigated TM-on-TM systems are classified into four types according to the observed intermixing and segregation behavior. Empirical rules are suggested to qualitatively predict the growth characteristics of any TM-on-TM system based on the atomic size difference, surface energy difference and enthalpy of mixing between the film and substrate atoms. An exponential trend is observed in the effective interface width as a function of the surface energy difference between the film and substrate layers, with a subtrend based on the crystal structure of the TM layers. A semi-empirical model that accurately describes the experimental data is presented. It serves as a scaling law to predict the effective interface width and the minimum film thickness required for full film coverage in TM-on-TM systems in general. The ability to predict the growth characteristics as well as the interface width for any TM-on-TM system significantly contributes to the process of finding the best material combination for a specific application, where layer growth characteristics are implicitly considered when selecting materials based on their functional properties.

2.1. INTRODUCTION

Nanoscale transition metal (TM) thin films are widely used in several applications such as superconductors, semiconductors, magnetic, diffusion barriers, oxidation protective layers, and X-ray optics. Improvements in vacuum technology and deposition techniques, especially the ability to deposit sub-nanometer thick layers, have been fueling the growth of thin-film-based technologies. When layer thicknesses reach the order of nanometers and sub-nanometers, the quality of the interface with adjacent layers becomes a key factor in realizing and further improving the device performance.

Nanoscale thin film structures are generally designed to function near room temperature, where bulk diffusion of atoms is kinetically inhibited. Yet intermixing with substrate atoms can easily occur during growth, even near room temperature, leading to wide interface profiles between the layers.[1,2] This has become one of the limiting factors that restrains a thin film structure from functioning at its maximum efficiency.[3,4] With the help of current state-of-the-art characterization techniques, it is possible to do an in-depth analysis of interfaces and completely reconstruct the atomic concentration profiles with high accuracy.[4,5] However, there is currently a limited capability to accurately predict the interface profile without having to deposit test structures and use advanced metrology for reconstruction. The availability of a scaling law to predict the interface profile between any two layers will add another dimension to the layer material selection process and consequently, enable us to find the best material combination for the desired application.

The existing layer growth and segregation models[6–11] cannot be used to predict interface profiles because of their dependence on energy terms (e.g. activation barrier, segregation energy) that can be obtained only from the experimental results of the specific material combination. Advancements in computational methods have made it possible to calculate the surface processes such as atomic exchange and adatom migration that take place during deposition.[12–17] Recently, Roling et al[17] compiled a database of calculated energies for adatom hopping and surface substitution in several transition metal systems. The database serves as a useful tool for a qualitative prediction of surface processes. Nevertheless, a quantitative prediction of the effective interface width due to intermixing during growth would require advanced simulations, which can become extremely time consuming and challenging. While it is a laborious task to develop a general predictive model using computation methods, methodical experimental studies can be a viable alternative approach. Buchanan et al[1] presented an experimental study on intermixing between sputter deposited aluminum and transition metals. The authors reported a correlation between the intermixing length and cohesive energy of the transition metals, but were unable to present a model that explains the results. Given the absence of other extensive systematic studies on interlayer formation in the literature, it is the aim of this work to

provide a generic database and develop a predictive model for intermixing in transition metal bilayer systems.

In this chapter, we present an experimental data set on intermixing during layer growth in sputter deposited transition metal – on – transition metal (TM-on-TM) thin films. The evolution of surface coverage during layer growth was systematically characterized using high sensitivity low energy ion scattering (HS-LEIS) and the effective interface width values were extracted from the experimental data. A semi-empirical model is developed based on the surface energy and crystal structure properties of the TM layers to describe the intermixing process during growth. The values of the model parameters are obtained by fitting the experimental results.

2.2. THEORETICAL BACKGROUND

2.2.1. Surface Exchange Model

Intermixing between film atoms and substrate atoms during deposition generally results in an intermixed zone between the layers. We consider intermixing to be the consequence of an exchange process between film and substrate atoms during layer growth. This approach is similar to the two-state-exchange model developed by Jorke[9] to explain the surface segregation of Sb on Si(100) during molecular beam epitaxy growth. The following assumptions are made in our model:

(1) In the current study, the deposition is done near room temperature. The energy for atom mobility at the surface level comes only from the deposition process, with energy of the incoming film atoms in the order of ~ 10 eV. Hence, the exchange process is considered to occur only between a surface atom and an underlying subsurface atom, whereas all the atoms below the subsurface layer are considered to be part of the bulk and do not take part in the exchange process.

(2) Surface-exchange processes are much faster than the timescale in which additional atoms arrive at the surface. This is certainly true for typical deposition rates on the order of sub-tenth nanometer per second and leads to a stationary state of surface and subsurface atoms before the arrival of the next atoms.

(3) Near room temperature, diffusion of atoms in the bulk and desorption of atoms from the surface are negligible. The position of an atom is therefore final once it is buried under subsequently deposited film atom.

(4) Although ~ 10 eV incoming film atoms do not induce resputtering[18], backscattered sputter gas neutrals with tens of eV energy can lead to resputtering of surface atoms. However, considering the typical low sputter yield up to ~ 100 eV of incident energy and the low fraction of high-energy backscattered neutrals, the number of resputtered atoms must be negligible (if not completely absent) when compared to the deposited film atoms. Therefore, resputtering during

growth is not considered in the model. Note that resputtering can become critical when low energy ion treatment or substrate bias is used during deposition and it may strongly affect the intermixing process.

(5) For the sake of simplicity, a typical 2D film layer growth is assumed without dewetting or island formation. This is a reasonable assumption considering the negative enthalpy of mixing for most TM-TM combinations.[19] The effects of positive mixing enthalpy on the surface morphology and intermixing process will be discussed in the results and discussion section.

We now consider two possible surface exchange mechanisms during film deposition: deposition induced exchange (Ex-1) and surface energy minimization induced exchange (Ex-2). Ex-1 is caused by the ballistic collision between incident atoms and surface atoms. It may depend on several factors such as the energy of the incident film atom, bond energy, atomic mass, coordination number and interatomic distance. Ex-1 is significant especially for deposition methods with high incident atom energy.[13–15] Ex-2 is driven by the reduction in the surface free energy of the system because of exchange in positions of the surface and subsurface atoms. It is well known that in an alloy the element with the lowest surface energy tends to segregate from the bulk towards the surface[20,21], which is one of the ways to reduce the surface free energy of the system. This is facilitated by bulk diffusion of atoms over long timescales and/or at elevated temperatures. In contrast, the deposition process takes place near room temperature and at short time scales. Thus, Ex-2 in general represents the exchange of atoms between the surface and subsurface layers because of surface-energy difference, and not due to diffusion of atoms from the bulk.

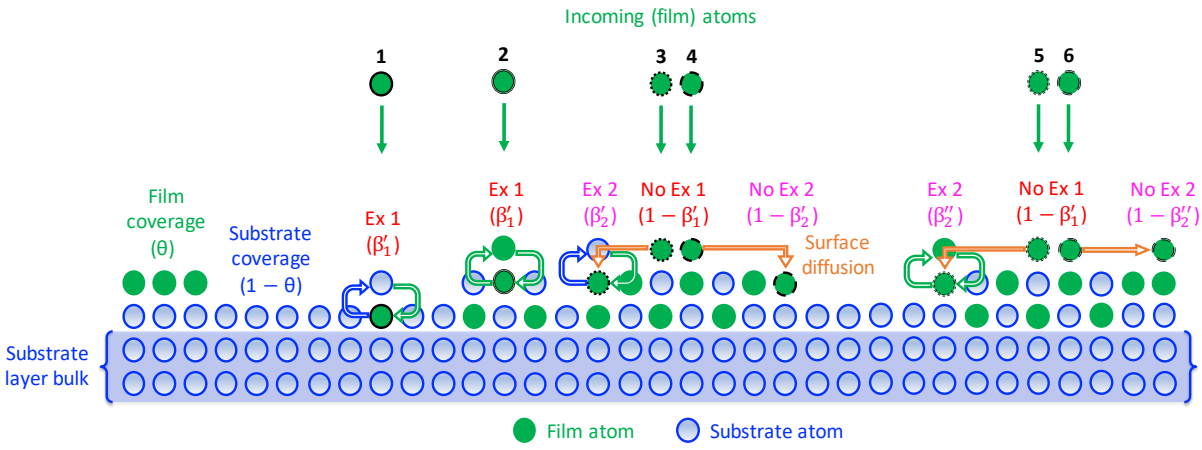

Figure 2.1. Schematic representation of all six surface exchange processes considered in the surface exchange model. To facilitate the tracking of incoming film atoms and their final locations, different border patterns (solid, short dashed and long dashed lines) are indicated for the film atoms 1 through 6.

A schematic representation of the surface exchange model is shown in Figure 2.1. Incoming film atoms arriving at the surface have a certain probability of being implanted into the surface through the exchange mechanism Ex-1 (represented by atoms 1 and 2). Although the probability of exchange

Ex-1 depends on the atomic composition near the site of arrival, it is not trivial to analytically express the exchange probability for each atom. As a result, we assume an effective probability of exchange Ex-1 (β_1') for a given film–substrate material combination. Atoms that undergo Ex-1 are assumed to remain in the stationary state until the next impact. Film atoms that do not undergo Ex-1, given by an effective probability ($1 - \beta_1'$), ultimately diffuse laterally to another surface position near the site of impact (represented by atoms 3,4,5 and 6). The surface diffusion process is activated mostly by the excess kinetic energy of the incident atom[22], whereas the latent heat of condensation[22,23] of the deposited film atoms can also contribute. The probability that a diffusing film atom stops on top of a substrate atom is equal to the coverage of the substrate atoms ($1 - \theta$), which is the fraction of surface area occupied by substrate atoms. At this point, the film atom can either exchange its position with the underlying substrate atom through the Ex-2 mechanism (represented by atom 3) or remain stationary until the next impact (represented by atom 4). Again, an effective probability (β_2') is assumed for the exchange Ex-2. Finally, the probability that a diffusing film atom stops on top of another film atom is equal to the coverage of the film atoms (θ), which is the fraction of surface area occupied by film atoms. Like in the previous situation, the film atom can either exchange its position with the underlying film atom through the Ex-2 mechanism (represented by atom 5) or remain stationary until the next impact (represented by atom 6). The effective probability of exchange Ex-2 between two film atoms is β_2''. It is important to note that out of all the 6 cases described here, only the fourth case (atom 4 in Figure 2.1) contributes to a change in the film layer coverage (θ). Consequently, the increment in film layer coverage ($d\theta$) for a small increment in deposition time (dt) can be expressed as:

$$d\theta = \frac{\phi}{N_{sd}^{f}}\, dt\ (1 - \beta_1')\,(1 - \theta)\,(1 - \beta_2') = \frac{\phi}{N_{sd}^{f}}\, dt\ \beta_1\,(1 - \theta)\,\beta_2, \tag{1}$$

where, ϕ is the deposition flux and N_{sd}^{f} is the surface atomic density of the film material; $\beta_1 = 1 - \beta_1'$ and $\beta_2 = 1 - \beta_2'$ for the sake of brevity. The deposited thickness (h) of the film layer for a deposition flux (ϕ), deposition time (t) and volume density of the film atoms (N_{vd}^{f}) is given by:

$$h = \frac{\phi\, t}{N_{vd}^{f}}\,. \tag{2}$$

From Eq. (1) and Eq. (2), the increment in film layer coverage for a small increment in the deposited film layer thickness (dh) can be expressed as:

$$d\theta = \frac{N_{vd}^{f}}{N_{sd}^{f}}\, dh\, \beta_1\, \beta_2\, (1 - \theta)\,. \tag{3}$$

We get the expression for film layer coverage as a function of the deposited film layer thickness by integrating Eq. (3):

$$\theta = 1 - e^{-\left(\frac{N_{vd}^{f}}{N_{sd}^{f}}\beta_1\,\beta_2\,h\right)}. \quad (4)$$

During the deposition process, the surface is continuously bombarded by energetic incoming film atoms. This leads to an increase in temperature near the site of impact by up to several thousand kelvin, which is dissipated within a few picoseconds.[15] The surface atomic exchange and diffusion processes activated by the impact of the incident film atom typically occur within the same timescale.[13] Therefore, considering a quasi-thermal equilibrium at the surface level[24,25] near the site of impact, for n_t^f number of deposited film atoms that did not undergo Ex-1 with substrate atoms, the ratio of number of these film atoms that move to the subsurface layer (n_2^f) and stay at the surface layer (n_1^f) because of exchange mechanism Ex-2 can be written as:

$$\frac{n_2^f}{n_1^f} = e^{-\left(\frac{\gamma_s - \gamma_f}{K_B T + \Delta E}\right)}, \quad (5)$$

where, γ_s and γ_f are the surface energies of substrate and film atoms, K_B is the Boltzmann constant, T is the growth temperature and ΔE is the additional energy available at the surface level because of the deposition process. Eq. (5) implies that when $\gamma_s \ll \gamma_f$, most of the film atoms will move to the subsurface layer via the Ex-2 mechanism, which is in qualitative agreement with the relative trends in the calculated energies of substitution reported by Roling et al[17]. According to the assumptions (3) and (4),

$$n_1^f + n_2^f = n_t^f. \quad (6)$$

The probability of a film atom staying at the surface without undergoing Ex-2 (β_2) is then given by:

$$\beta_2 = \frac{n_1^f}{n_t^f} = \frac{1}{1 + e^{-\left(\frac{\gamma_s - \gamma_f}{K_B T + \Delta E}\right)}}. \quad (7)$$

β_2 varies from 0 to 1 depending on the surface energies of film and substrate atoms. By substituting Eq. (7) in Eq. (4), the expression for the film thickness h_θ required to achieve a certain film layer coverage θ can be derived as:

$$h_\theta = -\ln(1-\theta)\left(\frac{N_{sd}^{f}}{N_{vd}^{f}\,\beta_1}\right)\left[1 + e^{-\left(\frac{\gamma_s - \gamma_f}{K_B T + \Delta E}\right)}\right]; \quad (8)$$

$$h_\theta = -\ln(1-\theta)\,A\left[1 + e^{-B\,(\gamma_s - \gamma_f)}\right], \quad (9)$$

where, $A = \left(\frac{N_{sd}^{f}}{N_{vd}^{f}\,\beta_1}\right)$ and $B = \left(\frac{1}{K_B T + \Delta E}\right)$ are the effective parameters with units of nm and $\frac{1}{eV}$, respectively. The parameter A denotes the intermixing due to ballistic collision and the parameter B, which is the inverse of the effective thermal energy of the surface atoms, dictates the importance of surface energy difference on the exchange mechanism Ex-2. When the effective thermal energy $K_B T +$

ΔE of the surface atoms increases, the surface energy difference between the film and substrate atoms becomes less significant. For instance, it has been reported that Pt atoms (high surface energy) submerge under a Ge substrate layer (low surface energy) during room temperature deposition, but emerge out at elevated temperatures.[26] Both the parameters may depend on several crystal structure properties like coordination number, nearest neighbor distance, lattice spacing, atomic packing and stacking sequence.

2.2.2. Interface Profile Model

The interface profile between two layers is often mathematically represented by exponential, linear, sinusoidal or error functions.[27] The most commonly used interface profile is the error function (ERF) profile[28] given by:

$$C(z) = \frac{1}{2}\left[1 - \mathrm{erf}\left(\frac{z - z_i}{\sigma\sqrt{2}}\right)\right], \tag{10}$$

where, C is the concentration of the deposited film atom at a depth z from the surface, z_i is the point of inflection of the error function and σ is the effective width of the interface. The integral of the concentration profile gives the deposited film layer thickness (h):

$$h = \int_0^\infty C\,(z)\,dz \tag{11}$$

The effectiveness of ERF to describe the interface profile in thin films has been recently reported by Coloma Ribera et al.[2] Nevertheless, it is complicated to analytically express the concentration (C) as a function of the deposited thickness (h). To overcome this problem, we propose to describe the interface profile by a logistic function (LGF)[29],

$$C(z) = \frac{1}{1 + e^{\left(\frac{z - z_i}{0.59\,\sigma}\right)}}, \tag{12}$$

whose shape is similar to that of an error function. The factor 0.59 within the exponent provides the best fit to the error function as shown in Figure 2.2. It is easier to integrate the LGF and express the concentration as a function of the deposited thickness. The deposited film layer thickness (h) can be obtained from the concentration profile according to Eq. (11):

$$h = 0.59\,\sigma \ln\left(1 + e^{\left(\frac{z_i}{0.59\,\sigma}\right)}\right). \tag{13}$$

Substituting z = 0 in Eq. (12) gives the expression for the film surface coverage (θ) and rearranging yields:

$$1 + e^{\left(\frac{z_i}{0.59\,\sigma}\right)} = \frac{1}{1 - \theta}. \tag{14}$$

Substituting Eq. (14) in Eq. (13) and rearranging yields:

$$\theta = 1 - e^{-\left(\frac{h}{0.59\,\sigma}\right)}. \tag{15}$$

Equating Eq. (4) and Eq. (15) and using Eq. (7), it is possible to express the effective interface width (σ) as a function of the surface energy difference between the layer materials:

$$\sigma = \frac{1}{0.59}\left(\frac{N_{sd}^{f}}{N_{vd}^{f}\,\beta_1}\right)\left[1 + e^{-\left(\frac{\gamma_s - \gamma_f}{K_B T + \Delta E}\right)}\right];$$

$$\sigma = \frac{1}{0.59}\,A\left[1 + e^{-B\,(\gamma_s - \gamma_f)}\right]. \tag{16}$$

The values of the effective parameters $A = \left(\frac{N_{sd}^{f}}{N_{vd}^{f}\,\beta_1}\right)$ and $B = \left(\frac{1}{K_B T + \Delta E}\right)$ can be extracted from the experimental dependence of σ on $\gamma_s - \gamma_f$. By understanding the relation between the effective parameters and the material properties, it must be possible to calculate the effective interface width for any TM-on-TM system with a given surface energy difference ($\gamma_s - \gamma_f$).

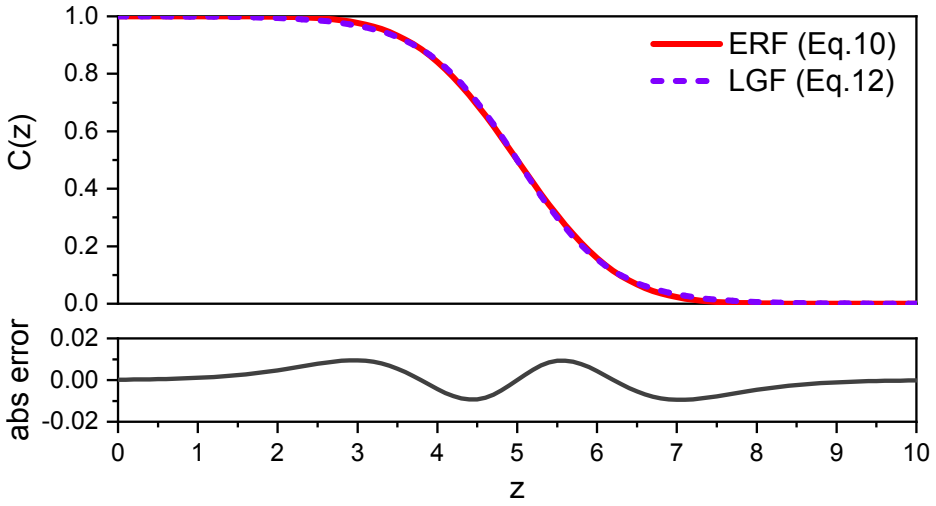

Figure 2.2. Comparison between an error function (ERF) curve according to Eq. (10) and a logistic function (LGF) curve according to Eq. (12). The values of z_i and σ are 5 and 1, respectively. The absolute error between the curves is shown in the bottom plot.

2.2.3. Surface Energy Values

Several theoretical calculations have been performed in the last decades to determine the crystal facet dependent surface energy values.[30,31] In contrast, experimental surface energy values for solid metals are usually obtained from the surface tension measurements of metals in liquid phase.[21] These surface energy values are independent of surface orientation and thus correspond to an averaged crystal plane orientation. Sputter deposited thin films are usually amorphous for the first few deposited monolayers, after which a polycrystalline growth with different surface facets is observed. Thus, the facet independent experimental surface energy values are more relevant to sputter deposited films than the calculated facet dependent values. For this reason, values of surface energies (J/m^2) for solids

obtained from surface tension measurements compiled by de Boer et al[21] are used in this work. The surface energy per atom (eV/atom) can be calculated from the surface energy per unit area (J/m^2) when the effective molar surface area (S_m) is known. The surface area of an atom is calculated from the molar volume (V_m) by assuming a certain shape for the atomic cell. For instance, the surface area (S) of a spherical atomic cell is given by[32]:

$$S = 4.8 \left(\frac{V_m}{N_0}\right)^{\frac{2}{3}}, \tag{17}$$

where, N_0 is Avogadro's number. However, only a fraction (f) of the surface area of a surface atom contributes to the effective surface area that is exposed to vacuum. The value of f depends on the number of nearest neighbors of an atom. As it is not trivial to express f as a function of coverage, we assume that effectively, one-third of the surface area of the spherical atomic cell is exposed to vacuum. The effective surface area of a mole of surface atoms (S_m) is then given by the equation:

$$S_m = f\, S\, N_0 = \frac{1}{3}\left[4.8 \left(\frac{V_m}{N_0}\right)^{\frac{2}{3}}\right] N_0 . \tag{18}$$

The surface energy values used in this work are listed in Table 2.1.

Table 2.1. List of surface energy values

Transition metal	Crystal structure at normal temperature and pressure	Surface energy from de Boer et al[21] $\left(\frac{J}{m^2}\right)$	Effective molar surface area, S_m x 10^4 $\left(\frac{m^2}{mol}\right)$	Surface energy $\left(\frac{eV}{atom}\right)$
Sc	hcp	1.28	8.22	1.09
Ti	hcp	2.10	6.54	1.42
V	bcc	2.55	5.75	1.52
Cr	bcc	2.30	5.05	1.20
Mn	bcc	1.60	5.13	0.85
Fe	bcc	2.48	4.99	1.28
Co	hcp	2.55	4.80	1.27
Ni	fcc	2.45	4.75	1.21
Cu	fcc	1.83	4.99	0.94
Zn	hcp	0.99	5.93	0.61
Y	hcp	1.13	9.89	1.15
Zr	hcp	2.00	7.89	1.63

Nb	bcc	2.70	6.63	1.85
Mo	bcc	3.00	6.02	1.87
Tc	hcp	3.15	5.63	1.84
Ru	hcp	3.05	5.54	1.75
Rh	fcc	2.70	5.54	1.55
Pd	fcc	2.05	5.80	1.23
Ag	fcc	1.25	6.40	0.83
Cd	hcp	0.74	7.51	0.58
La	hcp	1.02	10.2	1.08
Hf	hcp	2.15	7.70	1.71
Ta	bcc	3.15	6.64	2.17
W	bcc	3.68	6.07	2.31
Re	hcp	3.60	5.78	2.16
Os	hcp	3.45	5.62	2.01
Ir	fcc	3.00	5.65	1.75
Pt	fcc	2.48	5.89	1.51
Au	fcc	1.50	6.36	0.99

2.3. EXPERIMENT AND METHODOLOGY

TM-on-TM bilayer systems were deposited in an ultra-high vacuum sputter deposition chamber with *in vacuo* transfer to an IONTOF Qtac^{100} high-sensitivity low energy ion scattering (HS-LEIS) set up. Grazing incidence X-ray reflectivity (GIXRR) measurements were performed using a PANalytical Empyrean X-ray diffractometer (Cu-Kα: 0.154 nm). A Bruker Dimension Edge atomic force microscope (AFM) with a high-resolution tip (MikroMasch HiRes-C15/Cr-Au) was used for surface morphology characterization.

2.3.1. Deposition

All samples were deposited using dc magnetron sputtering with krypton as the sputter gas in a deposition chamber with $< 5\text{x}10^{-9}$ mbar base pressure and $1\text{x}10^{-3}$ mbar working pressure. The substrate-to-target distance was 8 cm. Single side polished Si(100) wafers with ~1 nm native oxide and 0.15 ± 0.05 nm root-mean-square (rms) roughness were used as substrates for deposition. The sputter voltage for the materials used was in the range of 300-600V, so similar particle energies can be expected for all the depositions. Each magnetron had a shutter in front to prevent cross-contamination and a quartz crystal microbalance (QCM) at close proximity to monitor the deposition rate and thickness. The deposition rates were calibrated by means of ex-situ GIXRR measurements on thick reference samples.

A bilayer architecture as shown in Figure 2.3 was used for all the TM-on-TM systems studied in this work. A 4 nm substrate layer was deposited directly on the Si wafer with native oxide and the film layer is grown on top. It is well-known that thin metal layers grown on SiO_2 tend to dewet and form islands at high temperatures.[33,34] Therefore, the native oxide is generally removed from the Si wafer prior to deposition. Since all the experiments presented in this work were carried out near room temperature, it was beneficial not to remove the native oxide as its presence can reduce the intermixing between the substrate layer and Si wafer.[2] To evaluate the effect of substrate layer morphology on film layer growth, the 4 nm substrate layers were studied using AFM. The rms roughness values are presented in Table 2.2. All materials except Cu show rms roughness in the range of ~ 0.2 nm, which represents a typical smooth substrate layer growth. The Cu substrate layer shows a factor 3 higher roughness, but no island formation was observed. Therefore, morphology of the substrate layers is expected to have no influence on the film layer growth.

Table 2.2. Surface rms roughness (nm) of 4 nm substrate layers deposited on Si wafer with native oxide.

Substrate layer	Co	Cr	Cu	Hf	Ir	Mo	Nb	Pd	Pt	Ru	Sc	Ta	Ti	W	Zr
rms roughness (± 0.05 nm)	0.16	0.17	0.57	0.15	0.12	0.18	0.25	0.18	0.24	0.13	0.18	0.16	0.14	0.27	0.19

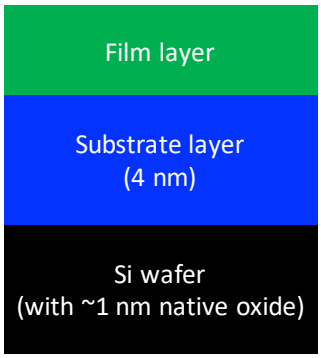

Figure 2.3. Schematic representation of the bilayer architecture used for the LEIS layer growth studies.

2.3.2. High Sensitivity Low Energy Ion Scattering (HS-LEIS)

In the LEIS technique, a noble gas primary ion with 1-8 keV energy is directed towards the sample surface at a fixed incidence angle. The energy of the backscattered ion provides information about the mass of the scattering surface atom according to the laws of conservation of energy and conservation of momentum. The advantage of HS-LEIS over conventional LEIS is the high LEIS signal to primary ion current ratio.[35] This allows us to use a low primary ion current and therefore, reduce the primary ion induced damage to the sample surface during LEIS measurement. HS-LEIS coupled with the *in vacuo* sample transfer provides the possibility to measure the surface composition

of as-deposited unaltered surfaces. More information about the LEIS technique can be found in the reference[36].

In this work, HS-LEIS measurements were performed using an IONTOF Qtac[100] tool with $1x10^{-10}$ mbar base pressure. A 5 keV Ne^+ primary ion beam with 1 nA ion current at normal incidence was used for the LEIS measurements. There are two main benefits of using Ne^+ primary ion instead of He^+: (1) higher mass resolution and (2) the effect of the background signal from a heavier element on the surface peak of a lighter element is reduced. An Ar^+ sputter gun operating at 0.5 keV ion energy and 59° incidence angle relative to the surface normal was used for the sputter depth profile measurements.

2.3.3. LEIS Growth Profile

Sputter depth profile measurement often induces strong intermixing of the layers under investigation. To avoid this, we use a non-destructive method called LEIS growth profile.[2] The procedure for recording a growth profile is described below with Mo-on-Pt as an example system. The same methodology was used for all other TM-on-TM systems presented in this work.

(1) 4 nm Pt layer was deposited on the Si wafer followed by 0.3 nm of Mo layer

(2) Sample was transferred *in vacuo* to the LEIS chamber, and LEIS spectrum was collected using Ne^+ primary ions

(3) 4 nm Pt layer was deposited on a new Si wafer followed by the Mo layer with a sub-nanometer increase in the thickness

(4) Steps 2 and 3 were repeated until the Mo layer signal saturates, which corresponds to 100% Mo film layer coverage

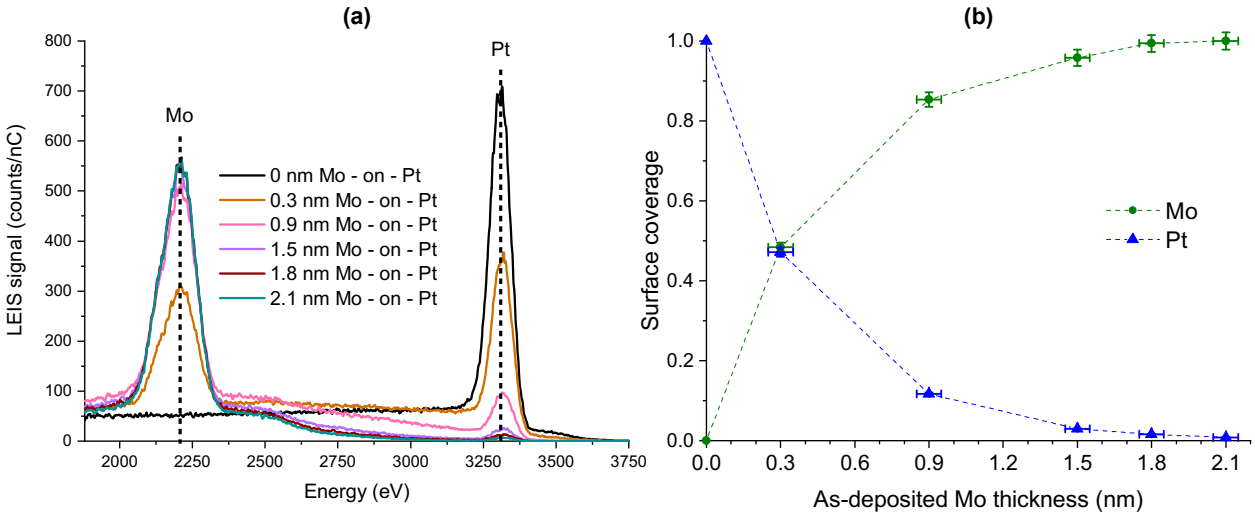

Figure 2.4. (a) LEIS spectra of Mo-on-Pt growth for various as-deposited Mo thicknesses and (b) surface coverage evolution of Mo and Pt atoms as a function of as-deposited Mo thickness

Typical LEIS spectra of Mo-on-Pt are shown in Figure 2.4a. The LEIS surface peaks that correspond to Mo and Pt are labelled in the figure. The integral area of the surface peaks is a direct measure of the number of Mo and Pt atoms present at the surface. The surface coverage of Mo and Pt for each growth step can be calculated from the ratio of integral peak areas of the investigated sample and the respective reference layers. The surface coverage evolution as a function of as-deposited film thickness (Figure 2.4b) can be used to obtain the effective interface width and to reconstruct the in-depth profile. Because LEIS cannot differentiate between intermixing and island formation, it is important to evaluate the surface morphology of the deposited film layer using an ex-situ AFM. Additionally, LEIS sputter depth profile is performed at various film thicknesses to qualitatively check if the evolution of the surface coverage is influenced by surface segregation effects.

2.4. RESULTS AND DISCUSSION

2.4.1. Growth Profile Types of TM-on-TM Systems

According to the proposed surface exchange model, the evolution of the film coverage as a function of as-deposited film layer thickness is directly related to the intermixing process during growth and hence, the LEIS growth profile can be defined by a simple logistic function (LGF) like interface model. We observe that this is true for most of the investigated TM-on-TM systems. However, in some systems an LGF-like interface model cannot fully describe the LEIS growth profile. We will show that in these cases the LEIS growth profile can be explained by considering contributions from the surface segregation of substrate or film atoms to the growth profile, in addition to the intermixing process. The definition of surface segregation in our work is tailored for the surface composition changes during thin film growth. We define it as the enrichment of the surface by film or substrate atoms during growth in comparison to the surface composition due to the intermixing process described by Ex-1 and Ex-2 mechanisms. Further details are discussed later in this section. We categorize all the TM-on-TM systems studied in this work into one of the following growth profile types based on the observed intermixing and segregation characteristics:

(1) Type-I growth profile: only intermixing process and no segregation of film or substrate atoms
(2) Type-II growth profile: segregation of substrate atoms in addition to the intermixing process
(3) Type-III growth profile: segregation of film atoms in addition to the intermixing process
(4) Type-IV growth profile: strong segregation of substrate atoms in addition to the intermixing process

We will first explain each growth profile type with example systems followed by the overall discussion at the end of the section.

Type-I growth profile, the most commonly observed growth type, is exhibited by TM-on-TM systems in which the evolution of surface coverage as a function of as-deposited film layer thickness

is defined purely by the surface exchange processes (Ex-1 and Ex-2) during growth according to Eq. (4). LEIS growth profiles of Zr-on-Pt and Zr-on-Ta, representatives of type-I growth profile, are shown in Figure 2.5. The effective interface width (σ) can be obtained by fitting the growth profile using a logistic function (LGF) like interface model given by Eq. (15). AFM images (not presented here) show a 2D growth with rms surface roughness value in the range of 0.2 nm. This means that the evolution of film layer coverage is a direct effect of intermixing during growth and not due to island formation.

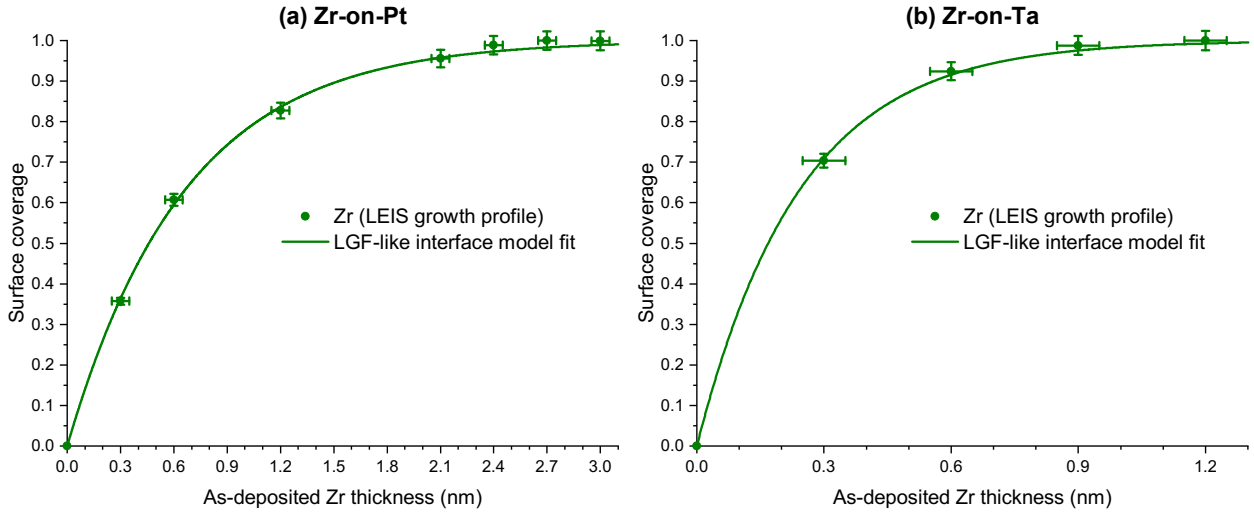

Figure 2.5. Representatives of type-I growth profile: (a) LEIS growth profile of Zr-on-Pt with LGF-like interface model fit and (b) LEIS growth profile of Zr-on-Ta with LGF-like interface model fit.

An overview of all investigated TM-on-TM systems exhibiting type-I growth profile is presented in Table 2.3. An asymmetry in the interfaces between two materials, as previously observed in Cr/Sc multilayer[4], can be seen in the investigated TM-on-TM systems. For example, the W-on-Pd interface width is 4 times larger than the Pd-on-W interface width. In general, this phenomenon can be explained by the surface energy difference between the film and substrate atoms. When the surface energy of the substrate atom is lower than that of the film atom, the probability of Ex-2 during growth increases, resulting in a wide interface. In contrast, the interface width is comparatively sharper when the film atom surface energy is lower than that of the substrate atom.

Table 2.3. Overview of all investigated TM-on-TM systems exhibiting type-I growth profile and the corresponding surface energy difference ($\gamma_s - \gamma_f$), effective interface width (σ) and rms roughness values. The rms roughness values are obtained from the AFM measurements of 0.9 nm TM – on – (4 nm) TM samples and the exceptions are mentioned within the brackets.

TM-on-TM	$\gamma_s - \gamma_f$ $\left(\frac{\text{eV}}{\text{atom}}\right)$	σ (nm)	rms roughness ± 0.05 nm
Mo-on-Nb	-0.02	$0.37^{+0.04}_{-0.04}$	0.16
Nb-on-Mo	0.02	$0.25^{+0.04}_{-0.04}$	0.17 (0.6nm Nb – on - Mo)
Ru-on-W	0.56	$0.36^{+0.02}_{-0.02}$	0.21

W-on-Ru	-0.56	$0.75^{+0.02}_{-0.02}$	0.21
W-on-Ti	-0.89	$1.00^{+0.02}_{-0.02}$	0.16
Ti-on-W	0.89	$0.39^{+0.02}_{-0.02}$	0.16
Pd-on-W	1.08	$0.38^{+0.02}_{-0.02}$	0.16
W-on-Pd	-1.08	$1.65^{+0.03}_{-0.03}$	0.16
Cr-on-W	1.11	$0.23^{+0.02}_{-0.02}$	0.18
W-on-Cr	-1.11	$0.69^{+0.02}_{-0.02}$	0.18
Pt-on-Ta	0.66	$0.64^{+0.06}_{-0.06}$	0.14 (1.5nm Pt – on – Ta)
Ta-on-Pt	-0.66	$1.03^{+0.09}_{-0.09}$	0.19 (1.5nm Ta – on – Pt)
Mo-on-Ta	0.30	$0.40^{+0.02}_{-0.02}$	0.17
Ta-on-Mo	-0.30	$0.36^{+0.02}_{-0.02}$	0.17
Mo-on-Pt	-0.36	$0.77^{+0.02}_{-0.02}$	0.43
Pt-on-Mo	0.36	$0.48^{+0.02}_{-0.02}$	0.17
Ru-on-Pt	-0.24	$0.98^{+0.02}_{-0.02}$	0.18
Pt-on-Ru	0.24	$0.72^{+0.02}_{-0.02}$	0.19 (1.5nm Pt – on – Ru)
Zr-on-Ta	0.53	$0.41^{+0.02}_{-0.02}$	0.19
Zr-on-Pt	-0.12	$1.12^{+0.03}_{-0.02}$	0.19 (1.2nm Zr – on – Pt)
Zr-on-Mo	0.24	$0.51^{+0.06}_{-0.06}$	0.12

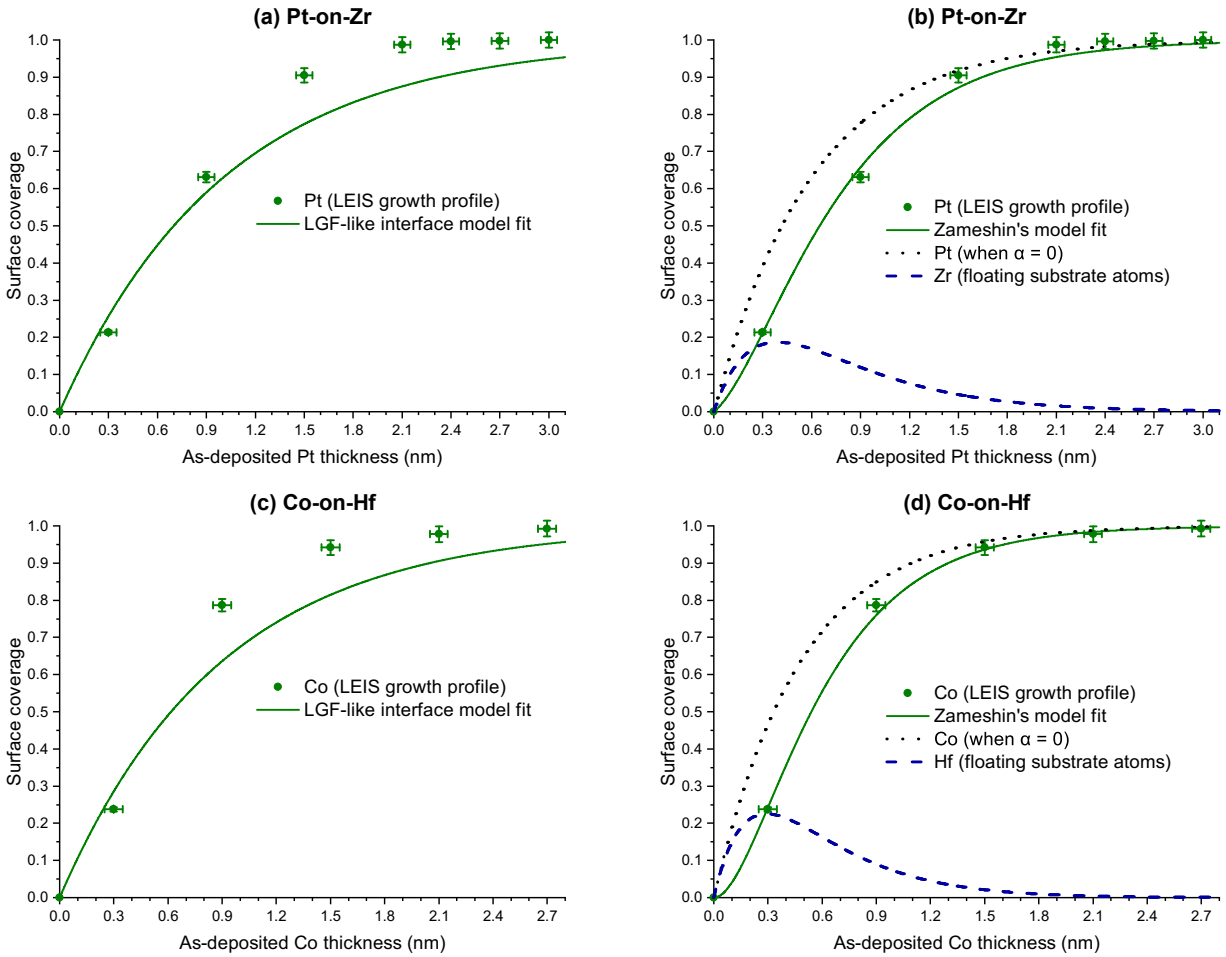

Figure 2.6. Representatives of type-II growth profile: LEIS growth profile of Pt-on-Zr with (a) LGF-like interface model fit and (b) Zameshin's segregation model fit, and LEIS growth profile of Co-on-Hf with (c) LGF-like interface model fit and (d) Zameshin's segregation model fit.

LEIS growth profiles of Pt-on-Zr and Co-on-Hf, representatives of type-II growth profile, are shown in Figure 2.6. Type-II growth profile is exhibited by TM-on-TM systems in which there is an additional drive, besides Ex-1 and Ex-2, for substrate atoms to move to the surface. Additional segregation of substrate atoms to the surface results in higher surface coverage of substrate atoms (lower surface coverage of film atoms) than what it should have been with only Ex-1 and Ex-2 processes. The LEIS growth profile fit (Figure 2.6a and Figure 2.6c) based on an LGF-like interface model (Eq. (15)) clearly cannot describe the surface coverage evolution of the film atoms. Recently, Zameshin et al[29] have developed a model that separates intermixing and segregation phenomena in the growth of Ru films on Si, B, C and B_4C layers. According to this model, additional segregation of substrate atoms during layer growth is purely a surface effect ("floating segregation") that does not affect the sub-surface composition. We consider that the floating substrate atoms are removed from the surface only via defect sites or grain boundaries as subsequent layers are being deposited. As a result, the floating segregation of substrate atoms affects only the surface coverage during growth, while the in-depth LGF-like interface profile is not affected significantly. The surface coverage of the film layer according to Zameshin's segregation model is:

$$C(z = 0, h, \alpha, \lambda) = \theta(h, \alpha, \lambda) = \left(1 - e^{\left(\frac{-h}{0.59\,\sigma}\right)}\right) - \left(\frac{\alpha}{0.59\,\sigma\,\lambda - 2}\left(e^{-\frac{2h}{0.59\,\sigma}} - e^{-\lambda h}\right)\right). \quad (19)$$

The dimensionless parameter α can be called the strength of floating segregation of substrate atoms as it indicates the addition of newly segregated atoms during growth. The parameter λ, with an inverse length unit, denotes the effectiveness of removal of the segregated atoms. In the simplest case of no floating segregation (α = 0), the model simplifies to type-I growth. The effective interface width (σ) and the segregation parameters (α and λ) for type-II TM-on-TM systems can be obtained by fitting the growth profile according to Eq. (19). We use the following constraints while fitting to obtain a physically realistic profile and reasonable values for the fit parameters: the rate of increase of film coverage is always positive $\left(\frac{d\theta}{dh} \geq 0\right)$ and the film coverage is between 0 and 1 ($0 \leq \theta \leq 1$).

Type-II growth profiles fitted using Zameshin's model are shown in Figure 2.6b and Figure 2.6d. Zameshin's model, with corresponding contributions from the film coverage in the absence of floating segregation (first term in Eq. (19), dotted line) and the floating substrate atoms (second term in Eq. (19), dashed line), explains the growth profile better than the standard LGF-like interface model. The coverage of floating substrate atoms increases initially as more film atoms arrive at the surface of the pure substrate layer. The segregated atom coverage reaches a maximum as all the exchange sites are covered and further segregation of substrate atoms from the buried substrate layer is strongly hindered. Some of the floating substrate atoms segregate further as subsequent atoms are deposited while the rest are removed via defect sites or grain boundaries, without significantly impacting the in-depth concentration of the film atoms. This results in a decrease in the coverage of the floating substrate atoms as a function of as-deposited film thickness and it eventually reaches zero when there are no more floating atoms.

An overview of all investigated TM-on-TM systems exhibiting type-II growth profile is presented in Table 2.4. Floating segregation of substrate atoms does not seem to depend on the surface roughness as it occurs in both the cases of standard (~ 0.2 nm) and increased (~ 0.4 nm) rms roughness. The floating segregation of substrate atoms occurs even when the film atom surface energy is lower than that of the substrate atom as seen in the case of Pt-on-Zr and Co-on-Hf. This clearly indicates that another energy term, besides surface energy, plays a dominant role in type-II systems, whereas it has no impact on type-I systems. Furthermore, when a system shows type-II growth profile, it does not automatically make the inverse system also type-II. For instance, Mo-on-Zr and Pt-on-Zr show type-II growth profile, whereas Zr-on-Mo and Zr-on-Pt show type-I growth. Nevertheless, the asymmetry in the interface width is still valid and can be explained by the surface energy difference.

Table 2.4. Overview of all investigated TM-on-TM systems exhibiting type-II growth profile and the corresponding surface energy difference ($\gamma_s - \gamma_f$), Zameshin's segregation model parameters (α and λ), effective interface width (σ) and rms roughness values. The rms roughness values are obtained from the AFM measurements of 0.9 nm TM – on – (4 nm) TM samples.

TM-on-TM	$\gamma_s - \gamma_f$ $\left(\frac{eV}{atom}\right)$	Zameshin's model parameters		σ (nm)	rms roughness (± 0.05 nm)
		α	λ (nm^{-1})		
Mo-on-Zr	-0.24	$0.98^{+0.02}_{-0.23}$	$2.8^{+1.8}_{-0.8}$	$0.7^{+0.1}_{-0.1}$	0.48
Pt-on-Zr	0.12	$0.79^{+0.06}_{-0.10}$	$1.9^{+0.5}_{-0.3}$	$1.02^{+0.09}_{-0.09}$	0.15
Co-on-Hf	0.45	$1.00^{+0.00}_{-0.02}$	$2.7^{+0.7}_{-0.6}$	$0.81^{+0.06}_{-0.06}$	0.14
Pd-on-Cu	-0.29	$0.36^{+0.10}_{-0.08}$	$1.2^{+0.8}_{-0.4}$	$1.6^{+0.2}_{-0.2}$	0.42
Pt-on-Cu	-0.57	$0.8^{+0.2}_{-0.2}$	$1.0^{+0.3}_{-0.2}$	$1.9^{+0.2}_{-0.2}$	0.36

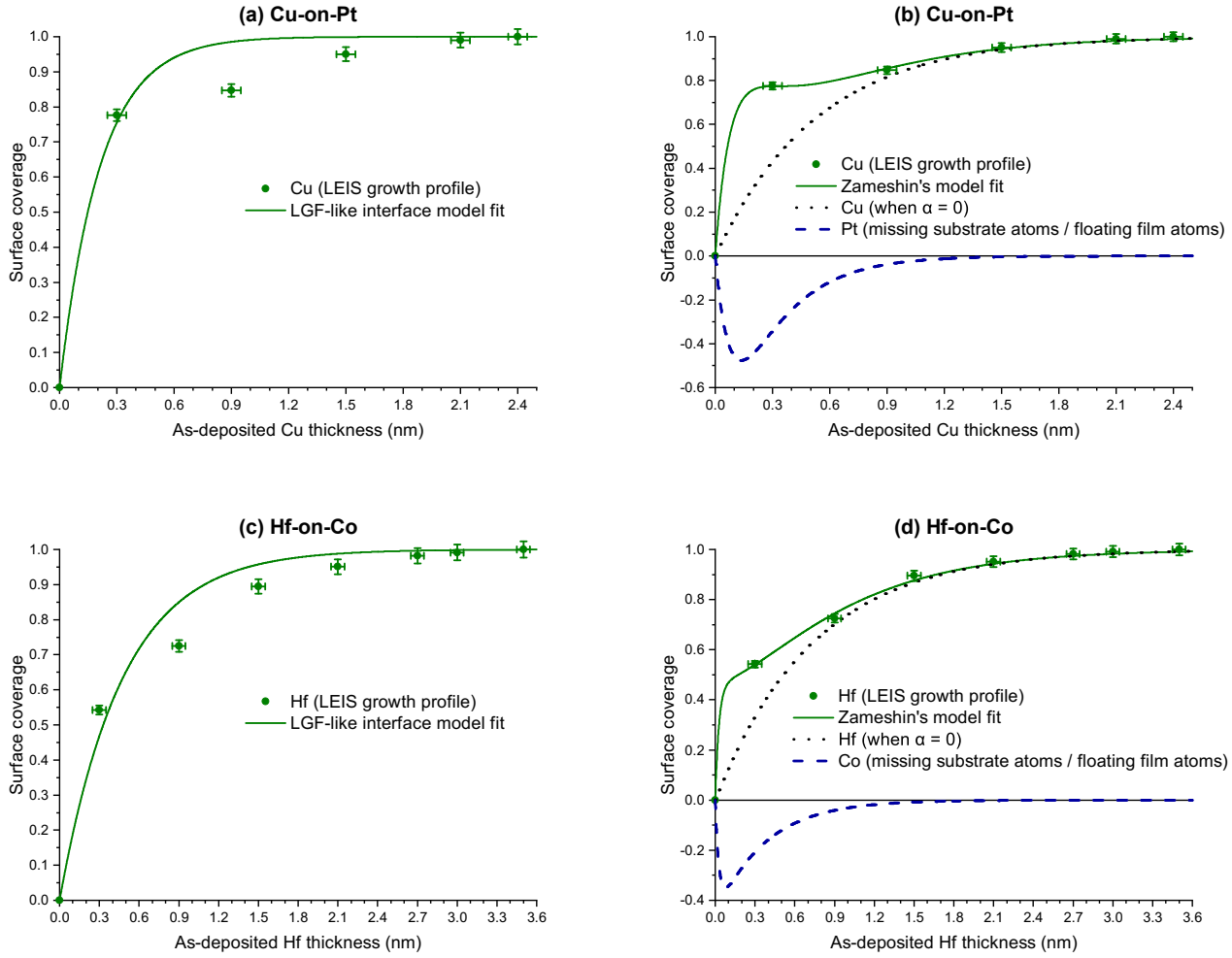

Figure 2.7. Representatives of type-III growth profile: LEIS growth profile of Cu-on-Pt with (a) LGF-like interface model fit and (b) Zameshin's segregation model fit, and LEIS growth profile of Hf-on-Co with (c) LGF-like interface model fit and (d) Zameshin's segregation model fit.

LEIS growth profiles of Cu-on-Pt and Hf-on-Co, representatives of type-III growth profile, are shown in Figure 2.7. Type-III growth profile is exhibited by TM-on-TM systems in which there is an additional drive for film atoms to stay at the surface, which is the exact opposite of type-II growth

where substrate atoms float at the surface. LEIS growth profile fit (Figure 2.7a and Figure 2.7c) based on an LGF-like interface model (Eq. (15)) once again cannot describe the surface coverage evolution of the film atoms. Also, Zameshin's segregation model is derived for the segregation of substrate atoms during growth and not for film atoms. Currently, we do not have a model to describe the floating segregation of film atoms. For this reason, we use Zameshin's model with a negative α to represent the reverse segregation of substrate atoms, in other words segregation of film atoms. The effective interface width (σ) and the segregation parameters (α and λ) for type-III TM-on-TM systems are obtained by fitting the growth profile using Zameshin's model according to Eq. (19).

Type-III growth profiles fitted using Zameshin's model are shown in Figure 2.7b and Figure 2.7d. Zameshin's model with a negative α describes the observed growth profile data well. The floating segregation of film atoms increases in the initial stages of growth and eventually goes to zero similar to the type-II growth. However, the effectiveness of removal of the segregated atoms is significantly greater in type-III growth, which can be explained by the fact that the film and segregating atoms are the same element.

An overview of all investigated TM-on-TM systems exhibiting type-III growth profile is presented in Table 2.5. A correlation is observed between the parameters α and λ, which allows for a wide range of possible solutions. The values of α and λ given in Table 2.5 are just an example from the several possible solutions. The effective interface width (σ) is however not affected by the correlation between α and λ and hence, the mean and the uncertainty values of σ obtained from the fits are reliable. It is important to note that the floating segregation of film atoms in type-III systems occurs even when the substrate atom surface energy is lower than that of the film atoms as observed for Hf-on-Co and Sc-on-Cu. Similar to the case of type-II systems, another energy term besides surface energy is expected to influence the segregation process in type-III systems. Finally, surface roughness does not seem to have a strong influence on type-III growth also.

Table 2.5. Overview of all investigated TM-on-TM systems exhibiting type-III growth profile and the corresponding surface energy difference ($\gamma_s - \gamma_f$), Zameshin's segregation model parameters (α and λ), effective interface width (σ) and rms roughness values. The rms roughness values are obtained from the AFM measurements of 0.9 nm TM – on – (4 nm) TM samples.

TM-on-TM	$\gamma_s - \gamma_f$ $\left(\frac{\text{eV}}{\text{atom}}\right)$	Zameshin's model parameters		σ (nm)	rms roughness (± 0.05 nm)
		α	λ (nm^{-1})		
Sc-on-Ru	0.66	-1.94	16.51	$0.64^{+0.35}_{-0.08}$	0.16
Sc-on-Cu	-0.14	-11.99	28.19	$1.12^{+0.09}_{-0.08}$	0.94
Sc-on-Ir	0.67	-5.13	18.13	$0.69^{+0.21}_{-0.09}$	0.14
Hf-on-Co	-0.45	-11.42	35.80	$1.26^{+0.06}_{-0.06}$	0.18
Cu-on-Cr	0.26	-1.96	18.02	$0.60^{+0.24}_{-0.05}$	0.25
Cu-on-W	1.37	-5.23	24.01	$0.46^{+0.07}_{-0.04}$	0.58

Cu-on-Ru	0.81	-7.24	47.64	$0.71^{+0.05}_{-0.05}$	0.16
Cu-on-Pd	0.29	-4.99	25.18	$1.02^{+0.10}_{-0.05}$	0.17
Cu-on-Pt	0.57	-5.29	12.48	$0.90^{+0.08}_{-0.07}$	0.22

LEIS growth profiles of Ru-on-Sc and Ta-on-Zr, representatives of type-IV growth profile, are shown in Figure 2.8. Type-IV growth profile is exhibited by TM-on-TM systems in which there is an additional drive for substrate atoms to segregate to the surface as in the case of type-II systems, but with a much stronger effect of floating segregation. At first glance, the fit based on the LGF-like interface model (Eq. (15)) seems to describe the type-IV growth profile reasonably well. However, the LEIS sputter profiles showed a surprising observation in contrast to what was observed for type-I, II and III systems. When the samples were sputtered, the substrate atom coverage decreased substantially while the film atom coverage increased by a similar magnitude. Later it will be shown that this effect can be explained only by strong floating segregation of substrate atoms. The fit obtained using the LGF-like interface model is therefore not valid. Moreover, a unique fit using Zameshin's segregation model is also not possible because of a strong correlation among the model parameters as a result of strong floating segregation.[29] Hence, it is not possible to obtain a reliable value for the effective interface width from the LEIS growth profiles of type-IV systems.

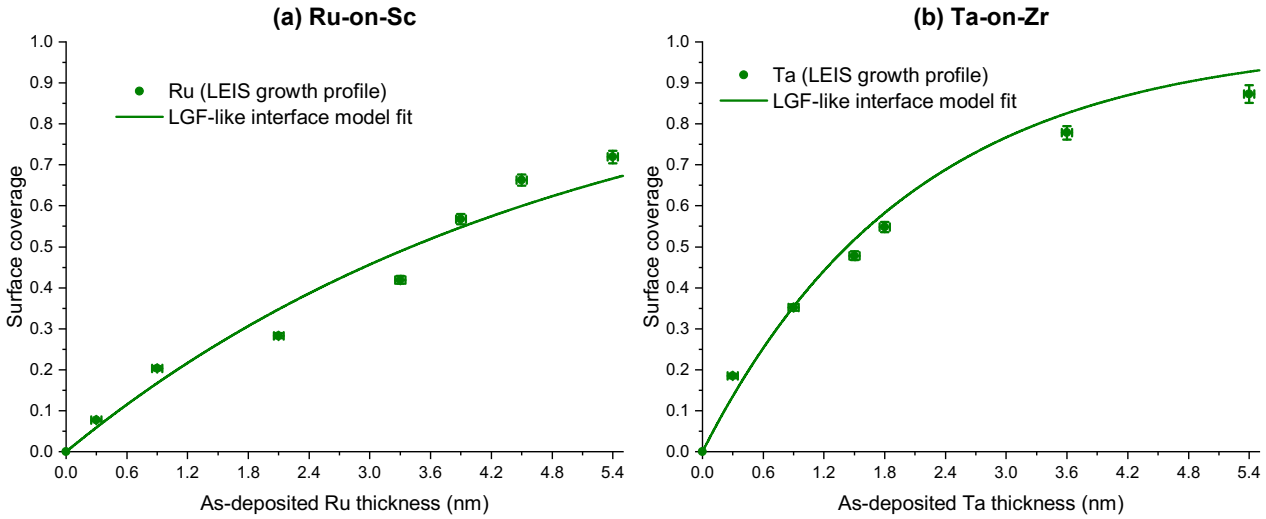

Figure 2.8. Representatives of type-IV growth profile: LEIS growth profile of Ru-on-Sc with LGF-like interface model fit and (b) LEIS growth profile of Ta-on-Zr with LGF-like interface model fit.

It should be emphasized that strong floating segregation does not actually mean a large effective interface width, as suggested by the growth profile (Figure 2.8). The floating segregation in type-IV systems can still be considered a surface effect as in the case of type-II systems. The main difference between type-II and type-IV systems is that the floating segregation of substrate atoms in type-II is removed within the intermixed zone, whereas in type-IV the effect of floating segregation continues further into the film layer. The effective interface width due to intermixing in type-IV systems is however expected to remain unaffected by the floating segregation, although it cannot be directly extracted from the LEIS growth profiles.

The schematic representations and the LEIS sputter profiles of an intermixed interface with no or limited segregation (type-I, type-II and type-III systems) and an intermixed interface with strong floating segregation of substrate atoms (type-IV systems) are shown in Figure 2.9. The LEIS sputter depth of 1.2 nm Zr – on – Ta (Figure 2.9b), representative of an intermixed interface, clearly shows the expected decrease in film (Zr) coverage and increase in substrate (Ta) coverage as a function of Ar sputter ion fluence. The coverage of Zr eventually reaches 0% (and 100% for Ta) as we sputter away the intermixed zone completely and enter the Ta substrate layer. The LEIS sputter profile of the inverse system, 5.4 nm Ta – on – Zr, representative of an intermixed interface with strong floating segregation of substrate atoms, is shown in Figure 2.9d. The film (Ta) coverage increases initially as the floating substrate (Zr) atoms are sputtered away. The growth of a pure film (Ta) layer under the floating substrate (Zr) atoms is evident from the LEIS sputter profile. As we sputter away the pure Ta film layer completely and enter the intermixed zone, the Ta coverage starts to decrease while Zr coverages increases.

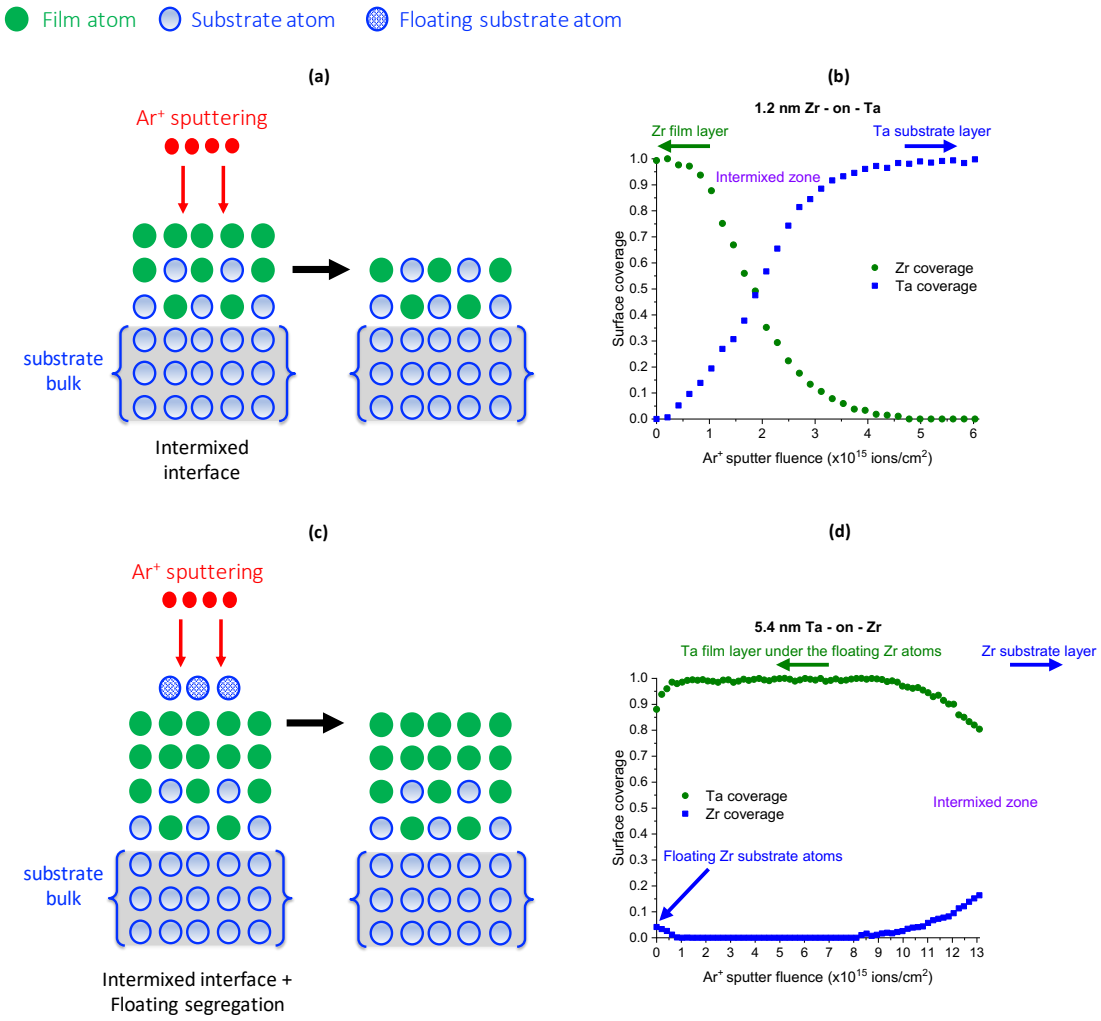

Figure 2.9. (a) Schematic representation of the intermixed interface exhibited by type-I, type-II and type-III systems and (b) LEIS sputter profile of 1.2 nm Zr – on – Ta. (c) Schematic representation of strong floating segregation of substrate atoms in addition to an intermixed interface exhibited by type-IV systems and (d) LEIS sputter profile of 5.4 nm Ta – on – Zr.

Apart from the cases with strong floating segregation of substrate atoms, type-IV growth profile also includes cases where island formation affects the growth profile. Though, island formation during growth alters the intermixing process such that an LGF-like interface profile is no longer valid. LEIS growth profile and AFM images of W-on-Cu, representative of type-IV growth profile with island formation, are shown in Figure 2.10. The surface coverage of W increases initially from 0% to 10% for 0.3nm W – on – Cu for which a 2D growth mode is observed. The growth changes to a 3D island mode at 0.6nm W – on – Cu. This change in growth mode from 2D to 3D with an increment of 0.3 nm shows the high surface mobility even near-room temperature. Further increase in the W thickness results in increase in both island density and height of each island, whereas the surface coverage of W (and Cu) remains unchanged, indicating a strong floating segregation of Cu in the islands. Ultimately, around 3.3nm W – on – Cu, the growth changes back to 2D growth as the islands coalesce together. After this point, the surface coverage of W starts to increase (and Cu coverage decreases) because of the removal of floating Cu atoms via defect sites or grain boundaries. LEIS sputter profile of 7.8 nm W – on – Cu sample, showed an increase in the W surface coverage from 76% to 100%, which means that the pure W film layer growth begins around this point.

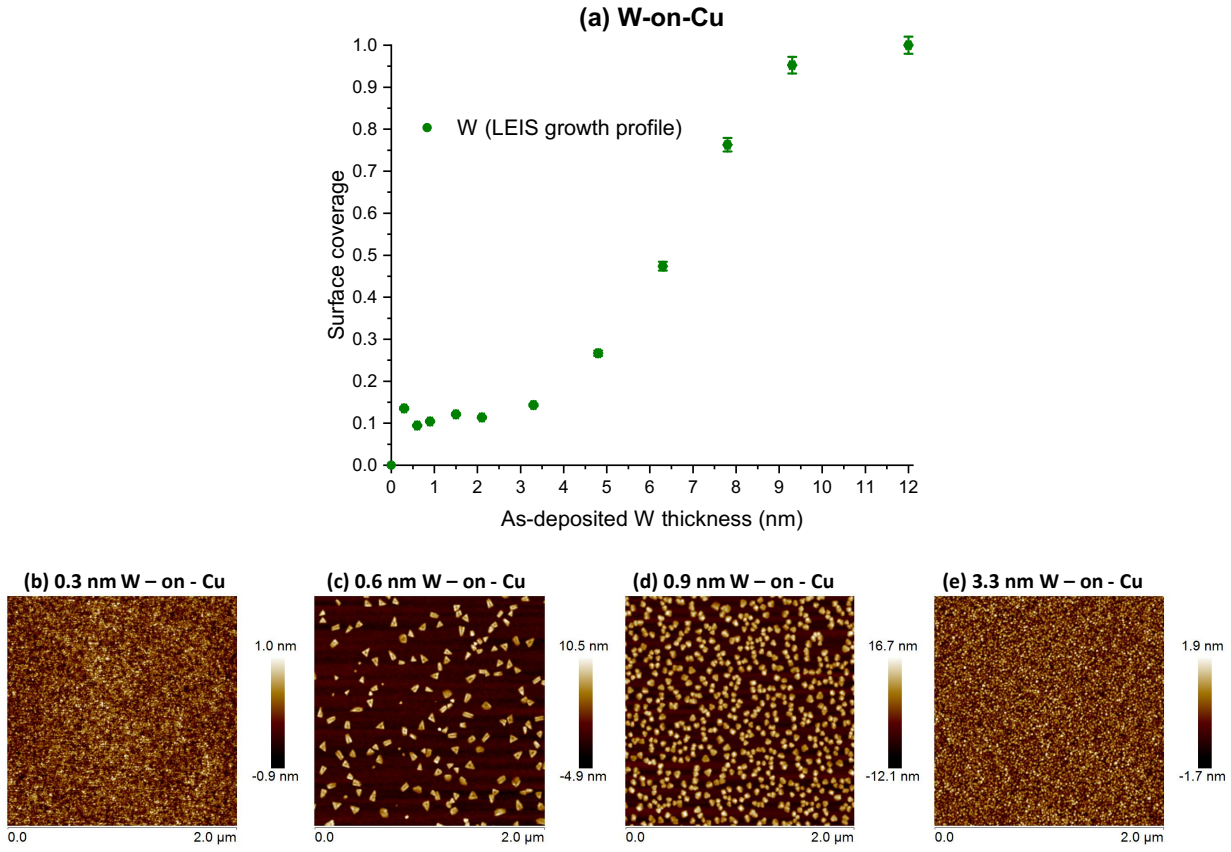

Figure 2.10. (a) LEIS growth profile of Won-Cu and (b - e) AFM images of 0.3 nm, 0.6 nm, 0.9 nm and 3.3 nm W – on – Cu, respectively.

An overview of all investigated TM-on-TM systems exhibiting type-IV growth profile is presented in Table 2.6. It is not possible to extract reliable values for the interface parameters (σ, α and

λ) from the LEIS growth profiles of type-IV systems because of strong floating segregation. The inverse combinations of all type-IV systems show either type-I or type-III growth. For instance, Ta-on-Zr shows type-IV growth, whereas Zr-on-Ta shows type-I growth.

Table 2.6. Overview of all investigated TM-on-TM systems exhibiting type-IV growth profile and the corresponding surface energy difference ($\gamma_s - \gamma_f$) and rms roughness values. The rms roughness values are obtained from the AFM measurements of 0.9 nm TM – on – (4 nm) TM samples. * W-on-Cu exhibits 3D growth between 0.6 nm – 3.3 nm W and 2D growth after that. Hence, the rms value does not represent the surface roughness of other as-deposited W thicknesses.

TM-on-TM	$\gamma_s - \gamma_f \left(\frac{eV}{atom}\right)$	rms roughness (± 0.05 nm)
Ir-on-Sc	-0.67	0.15
Ru-on-Sc	-0.66	0.16
Cu-on-Sc	0.14	0.88
W-on-Cu	-1.37	5.87*
Ru-on-Cu	-0.81	0.47
Cr-on-Cu	-0.26	0.30
Ta-on-Zr	-0.53	0.20

As shown earlier, surface energy is not the only driving factor for floating segregation as it occurs even when the surface energy of the floating atom is not favorable for segregation. Surface roughness also does not seem to contribute to floating segregation, although 3D growth can alter the intermixing process. Because all investigated materials were sputter deposited under similar conditions, it is unlikely that the deposition process affects floating segregation of atoms during growth. The only noticeable connection between floating segregation in type-II, type-III and type-IV systems is the elements that tend to segregate to the surface. Out of all the 15 investigated transition metals, only Zr, Hf, Sc and Cu show floating segregation behavior. In terms of the atomic size (metallic radius), Sc, Zr and Hf are the largest, whereas Co, Cu and Cr are the smallest among the transition metals studied in this work. Large size difference between film and substrate atoms can induce strain during intermixing. Because we do not consider strain energy in the surface exchange model, we are unable to provide a quantitative analysis for the floating segregation observed during growth. Also, it is possible that the strain energy on the surface, especially during growth, is different from that of the bulk. Nevertheless, the effect of size difference on growth types can still be considered qualitatively.

The difference in atomic radii between substrate and film atoms ($r_s - r_f$) for all the investigated TM-on-TM systems is shown in Figure 2.11. The difference in atomic radii of all type-I systems is mostly close to zero, which explains why the size related effects in type-I growth are negligible. For type-II systems we observe two cases: (i) systems with large positive atomic radii difference, where the substrate atom is much larger than the film atom, (ii) systems with size difference

comparable to type-I systems. For type-III systems we observe two cases: (i) systems with large negative atomic radii difference, where the film atom is much larger than the substrate atom, (ii) systems with size difference comparable to type-I systems. For type-IV systems, which are similar to type-II but with stronger driver for floating segregation, we again observe two cases: (i) systems with large positive atomic radii difference, where the substrate atom is much larger than the film atom, (ii) systems with size difference comparable to type-I systems.

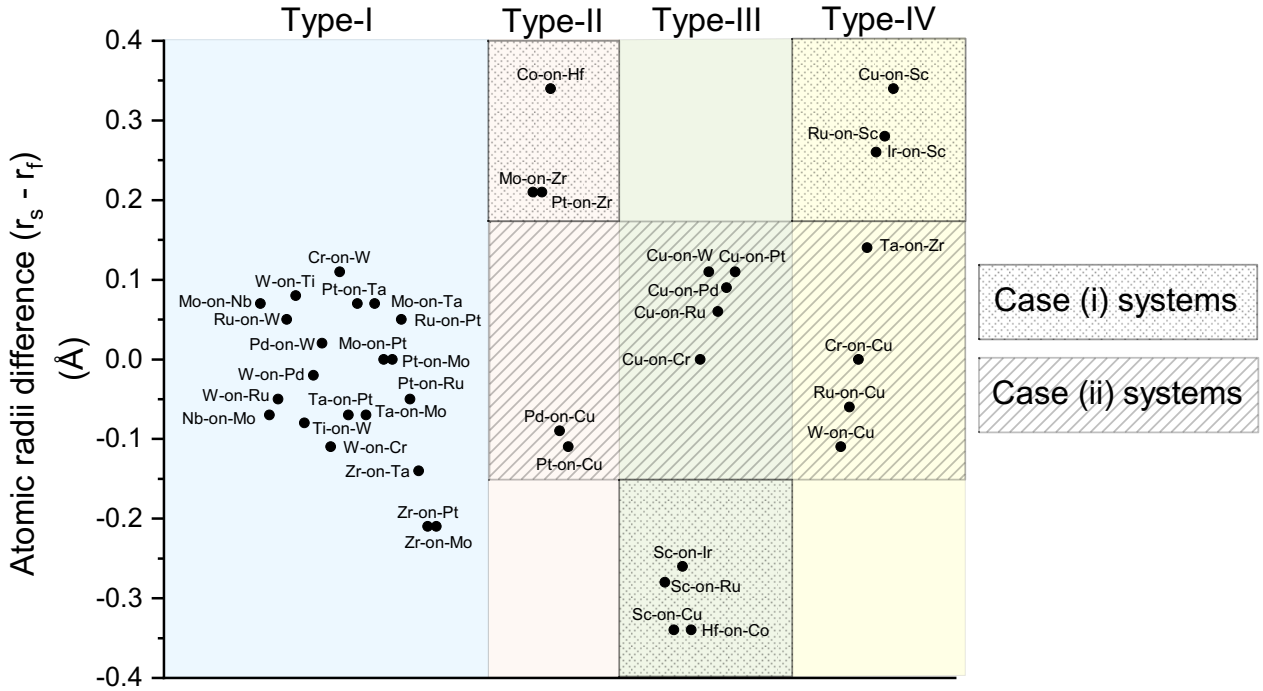

Figure 2.11. Atomic radii difference ($r_s - r_f$) of all investigated TM-on-TM systems.

In type-II and type-IV systems, for large positive atomic radii difference (case i), the largest atom (Hf, Zr, Sc in our case) always tends to float at the surface, consequently reducing the strain energy in the surface layer. It is important to note that although Co-on-Hf and Cu-on-Sc have the same atomic radii difference, they exhibit different growth profile types: type-II and type-IV, respectively. This can be explained by the surface energy difference between Co-Hf (0.45 eV/atom) and Cu-Sc (0.14 eV/atom). In Co-on-Hf, the large size difference drives the floating segregation of the substrate Hf atom, but the low surface energy of Co film atom limits the floating segregation, resulting in a type-II growth profile. For Cu-on-Sc, the large size difference drives the floating segregation of substrate Sc atom and the small difference in surface energy does not hinder the floating segregation, resulting in a type-IV growth profile. In effect, the interplay between surface energy difference and atomic size difference determines if a TM-on-TM system exhibits type-II or type-IV growth profile. Similarly, in type-III systems, for large negative atomic radii difference (case i), the largest atom (Hf and Sc in our case) tends to float. Note that Zr-on-Ta, Zr-on-Mo and Zr-on-Pt have larger negative atomic radii difference when compared to other type-I systems and may exhibit floating segregation of Zr in the

initial stages of growth. However, the effect is not significant enough to affect the growth at a film thickness of 0.3 nm or later. This is why these systems show a typical type-I growth profile.

All case (ii) TM-on-TM systems in type-II and type-III have Cu as the element that exhibits floating segregation. Atomic size difference in these systems is comparable to type-I systems and hence, does not seem to play an important role. The magnitude of segregation is however influenced by the surface energy difference. For example, floating segregation of Cu in Pt-on-Cu is stronger than in Pd-on-Cu because of larger negative surface energy difference (Table 2.4). Interestingly, in Sc-on-Cu and Cu-on-Sc, Sc is the element that exhibits floating segregation. This means Cu tends to float at the surface in Cu-on-TM and TM-on-Cu systems provided the TM is not a large atom like Sc, where size effects dominate. It is not clear what drives the floating segregation of Cu during layer growth. The low melting point of Cu (the lowest of all TMs studies in this work) suggests a low activation energy for self-diffusion[37], which can possibly explain its preference to float at the surface. The effect of high surface mobility can also be seen in W-on-Cu where the growth changes from 2D to 3D with an increment of 0.3 nm W thickness (Figure 2.10). This means, other TMs with low melting point[37] such as Ag and Au can also be expected to show floating segregation behavior. Nevertheless, further work is required to understand the floating behavior of Cu in detail.

The case (ii) TM-on-TM systems in type-IV show no size dependence either. A unique relation among these systems is that they all have positive enthalpy of mixing[19,21]: Cu-Cr (+12.39 kJ/mol), Zr-Ta (+2.74 kJ/mol), Cu-W (+22.33 kJ/mol), and Cu-Ru (+6.98 kJ/mol). All other investigated TM-on-TM systems have negative enthalpy of mixing[19,21], with one exception: W-Cr has positive enthalpy of mixing (+0.95 kJ/mol), but both W-on-Cr and Cr-on-W show type-I growth profile. On this basis, it is possible to conclude that the positive enthalpy of mixing seems to affect only those TM-on-TM systems with substrate atoms that tend to float. W-on-Cu, Ru-on-Cu and Cr-on-Cu are expected to show type-II growth profile (floating segregation of substrate atoms) like Pd-on-Cu and Pt-on-Cu, but the positive mixing energy drives the floating segregation of Cu to a larger extent such that it becomes type-IV growth profile with Cu atoms floating beyond the intermixed zone. This explanation is valid for Ta-on-Zr system also. The inverse systems Zr-on-Ta, Cu-on-W, Cu-on-Ru and Cu-on-Cr, where the film atom exhibits floating segregation, are not affected by the positive mixing enthalpy. Cr and Cu are similar in size and still Cr does not show floating behavior in W-on-Cr and Cr-on-W systems even when there is positive mixing energy. This suggests that the floating behavior of Cu is its inherent property and not due to its small atomic radius. Large positive mixing enthalpy of W-Cu also explains the 3D island growth in W-on-Cu system. An interplay between surface energy and mixing enthalpy determines if the layer growth will be 2D or 3D.

The layer materials for TM-on-TM growth studies were chosen to have a diverse combination from different groups and periods within the transition metal block. Therefore, the layer growth results presented here are believed to be of relevance for all TM-on-TM combinations in general. On the basis of current data set, we propose a general rule to predict the growth type of a TM-on-TM system as given in Table 2.7.

Table 2.7. Empirical rules to predict the probable growth profile type in TM-on-TM systems based on the atomic radii difference ($r_s - r_f$), enthalpy of mixing and surface energy difference. *Note: Ag and Au may show similar behavior as Cu because of their low melting point.

System	$r_s - r_f$ (Å)	Enthalpy of mixing $\left(\frac{kJ}{mol}\right)$	Probable growth profile type	Element expected to segregate
TM-on-TM	– 0.22 to + 0.12	+ or –	Type-I	-
	> + 0.12	–	Type-II or Type-IV (depending on surface energy difference and size difference)	Substrate
		+	Type-IV	Substrate
	< – 0.22	+ or –	Type-III	Film
Cu*-on-TM	– 0.22 to + 0.12	+ or –	Type-III	Cu*
	> + 0.12	–	Type-II or Type-IV (depending on surface energy difference and size difference)	Substrate
		+	Type-IV	Substrate
TM-on-Cu*	– 0.22 to + 0.12	–	Type-II	Cu*
		+	Type-IV	Cu*
	< – 0.22	+ or –	Type-III	Film

In summary, floating segregation during growth is purely a surface effect and it does not fundamentally affect the intermixing process or the interface profile. It is caused by the large size difference and influenced by the surface energy difference and enthalpy of mixing. Weak floating segregation in the case of type-II and type-III systems is limited to the intermixed zone and the floating atoms are removed via defect sites or grain boundaries before the growth of a pure film layer begins. In type-IV systems, floating segregation is much stronger than in type-II systems and its effect on the growth profile continues beyond the intermixed zone into the film layer. When the atomic radii difference is large, the largest atom always segregates to the surface. Cu tends to segregate to the surface in both TM-on-Cu and Cu-on-TM systems except when TM is a large atom like Sc.

2.4.2. Scaling Law for Intermixing in TM-on-TM Systems

According to the surface exchange model and interface profile model explained in the theoretical background section, the effective interface width (σ) between two TM layers is related to the surface energies of the film and substrate atoms as given by Eq. (16). The values of parameter A $\left(\frac{N_{sd}^{f}}{N_{vd}^{f}\,\beta_1}\right)$, which denotes intermixing due to ballistic collision and parameter B, the inverse of effective thermal energy of surface atoms $\left(\frac{1}{K_B T + \Delta E}\right)$, can be extracted from the experimental data. As mentioned in the previous section, both A and B can depend on several crystal structure properties of the film and substrate layers, such as coordination number, nearest neighbor distance, lattice spacing, atomic packing and stacking sequence. It is important to note that both amorphous and crystalline materials have been shown to exhibit similar short range order and nearest neighbor properties.[38–40] Therefore, A and B must predominantly depend on the preferred crystal structure of the layer materials, irrespective of the crystallinity (amorphous or crystalline). Hence, we categorize the TM-on-TM systems according to their crystal structure combination and evaluate the values of parameters A and B for different structure combinations. All transition metals except mercury (Hg) have one of the following three crystal structures at room temperature: bcc, hcp and fcc. Thus, there are six possible structure combinations for TM-on-TM systems: bcc-bcc, hcp-hcp, fcc-fcc, bcc-hcp, bcc-fcc and hcp-fcc. Figure 2.12 shows the effective interface width values of type-I, type-II and type-III TM-on-TM systems plotted as a function of surface energy difference ($\gamma_s - \gamma_f$) and grouped according to the structure combinations. Interface width values of each structure combination are fitted independently using Eq. (16) and the values of parameters A and B obtained from the respective fits are presented in Table 2.8. The fact that all the σ values for a given structure combination, irrespective of the TM-on-TM growth type, can be fitted with a single exponential function signifies that A and B predominantly depend on the crystal structure of the film and substrate layers. This also proves that Zameshin's segregation model can provide accurate effective interface width values for type-II and type-III systems by separating the intermixing and segregation processes.

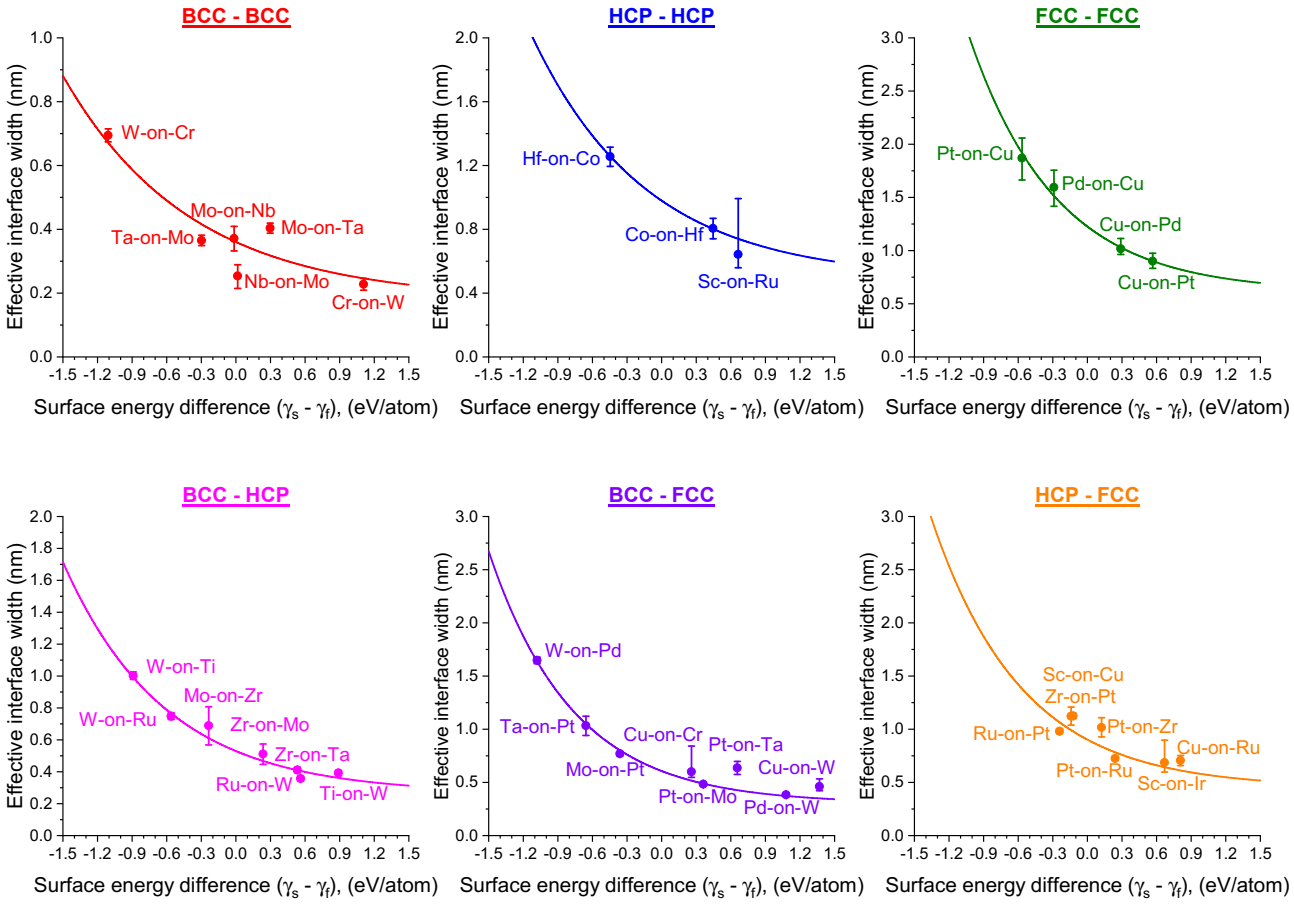

Figure 2.12. Effective interface width of all investigated TM-on-TM systems plotted as a function of difference in surface energy ($\gamma_s - \gamma_f$) and categorized according to the crystal structure combination. The exponential fit for each structure combination is based on Eq. (16).

Table 2.8. The values of effective parameters A and B for each structure combination obtained by fitting the experimental effective interface width data.

TM-on-TM structure combination	A (nm)	B $\left(\frac{1}{\text{eV}}\right)$
BCC-BCC	0.11 ± 0.01	0.9 ± 0.2
HCP-HCP	0.29 ± 0.02	1.0 ± 0.2
FCC-FCC	0.36 ± 0.01	1.3 ± 0.1
BCC-HCP	0.16 ± 0.01	1.13 ± 0.07
BCC-FCC	0.18 ± 0.01	1.37 ± 0.06
HCP-FCC	0.27 ± 0.02	1.3 ± 0.5

A clear correlation is found between the parameter A and the structure combination. In general, the bond energies follow the order bcc > hcp > fcc.[41] This explains why the value of A is the smallest for bcc-bcc and largest for fcc-fcc. The values of parameter B indicate that the effective thermal energy

of surface atoms in bcc structure is greater than those in hcp and fcc structures. Thus, the dependence of intermixing on surface energy is stronger in fcc-based structure combinations and weaker in bcc-based combination. Because the exponential trend is unique for each structure combination, they can be used as a scaling law to predict the intermixing in TM-on-TM systems. The effective interface width of any given TM-on-TM can thus be calculated using Eq. (16) by substituting the appropriate values for surface energies (Table 2.1) and the parameters A and B (Table 2.8). By using Eq. (9) instead of Eq. (16), it is possible to calculate the film layer thickness that is required to achieve a certain film coverage or the film coverage for a certain as-deposited film thickness. This is useful for applications in which it is important to have a closed film layer to prevent the exposure of substrate layer. Note that the film coverage will be strongly affected by the floating segregation in type-IV growth where the film layer grows under the floating substrate atoms. In such cases, it is possible to remove the floating substrate atoms by physically sputtering or etching the top surface and obtain a pure film surface as shown in Figure 2.9d.

Finally, it is important to realize that parameters A and B depend on the total energy contribution from the deposition process such as the energy of the incident film atom, substrate temperature, and ion bombardment. Actual values of the effective interface width can deviate from those predicted by the scaling law if the particle energies are considerably different than those typically encountered in magnetron sputtering. However, the relative trends based on crystal structure and surface energy difference are expected to be valid for all TM-on-TM systems deposited under similar conditions. Further understanding on the dependence of A and B on the incident atom energy and substrate temperature will enable the quantitative prediction of the interface characteristics for a wide range of deposition conditions.

2.5. SUMMARY AND CONCLUSIONS

Intermixing during layer growth in sputter-deposited transition metal – on – transition metal (TM-on-TM) systems was studied using high sensitivity low energy ion scattering (HS-LEIS). *In vacuo* LEIS growth profiles were obtained by measuring the surface coverage of film atoms as a function of increasing film layer thickness. The effective interface width values were extracted from the LEIS growth profile fit based on a logistic function (LGF) like interface profile model. Segregation of substrate or film atoms to the surface (floating segregation) in addition to the standard intermixing process was observed in several TM-on-TM systems. A segregation model developed by Zameshin et al that separates the intermixing and segregation effects was used to extract the interface width values for such systems. In some TM-on-TM systems, the drive for floating segregation was much stronger and it was not possible to extract the interface width values by fitting the LEIS growth profile. Overall, we were able to categorize all the investigated TM-on-TM systems into four different growth profile

types based on the type and strength of segregation observed. Finally, we confirm the exponential dependence of effective interface width on surface energy difference according to the proposed surface exchange model and show that there is a subtrend for each crystal structure combination of TM-on-TM systems. The model parameters extracted from the experimental data can be used to calculate the effective interface width for any TM-on-TM system.

The following conclusions are derived:

1. Intermixing in TM-on-TM systems can be described by the following surface exchange mechanisms: deposition induced exchange (Ex-1) and surface-energy minimization induced exchange (Ex-2). The effective interface width can be obtained based on an LGF-like interface model. The interface width is large when the surface energy of the substrate atom is lower than that of the film atoms and comparatively sharper for the reverse situation.
2. A large size difference between the film and substrate atoms results in floating segregation of the largest atom during growth. The strength of floating segregation is determined by an interplay between surface energy difference, size difference and mixing energy. Essentially, floating segregation is shown to be an effect that is limited to the surface, which occurs in addition to the Ex-1 and Ex-2 mechanisms during growth, and it does not affect the final interface profile of the layered structure. As a special case, Cu exhibits floating segregation behavior in both TM-on-Cu and Cu-on-TM systems, as long as the TM is not a large atom like Sc.
3. There is a unique exponential trend in the interface width as a function of surface-energy difference for each crystal structure combination, which serves as a scaling law to predict the intermixing in TM-on-TM systems. In general, bcc TMs intermix less when compared to hcp and fcc TMs because of higher bond strength of bcc atoms.

As an overall conclusion, the proposed general rule for predicting the growth profile type and the proposed scaling law for predicting the effective interface width, together provide the possibility to predict the growth and interface characteristics in TM-on-TM systems. This opens a new field of possibilities in controlling the quality of interfaces in thin film structures, and it is expected to have a direct impact on the development of applications where the interfaces are critical for the device performance.

2.6. REFERENCES

(1) Buchanan, J. D. R.; Hase, T. P. A.; Tanner, B. K.; Chen, P. J.; Gan, L.; Powell, C. J.; Egelhoff, W. F. Anomalously Large Intermixing in Aluminum–Transition-Metal Bilayers. *Phys. Rev. B* **2002**, *66* (10), 104427. https://doi.org/10.1103/PhysRevB.66.104427.

(2) Coloma Ribera, R.; van de Kruijs, R. W. E.; Sturm, J. M.; Yakshin, A. E.; Bijkerk, F. In Vacuo

Growth Studies of Ru Thin Films on Si, SiN, and SiO 2 by High-Sensitivity Low Energy Ion Scattering. *J. Appl. Phys.* **2016**, *120* (6), 065303. https://doi.org/10.1063/1.4960577.

(3) Keavney, D. J.; Park, S. K.; Falco, C. M.; Slaughter, J. M. Specular and Diffuse Electron Scattering at Interfaces in Metal Spin-Valve Structures. *J. Appl. Phys.* **1999**, *86* (1), 476–479. https://doi.org/10.1063/1.370755.

(4) Haase, A.; Bajt, S.; Hönicke, P.; Soltwisch, V.; Scholze, F. Multiparameter Characterization of Subnanometre Cr/Sc Multilayers Based on Complementary Measurements. *J. Appl. Crystallogr.* **2016**, *49* (6), 2161–2171. https://doi.org/10.1107/S1600576716015776.

(5) Zameshin, A.; Makhotkin, I. A.; Yakunin, S. N.; van de Kruijs, R. W. E.; Yakshin, A. E.; Bijkerk, F. Reconstruction of Interfaces of Periodic Multilayers from X-Ray Reflectivity Using a Free-Form Approach. *J. Appl. Crystallogr.* **2016**, *49* (4), 1300–1307. https://doi.org/10.1107/S160057671601044X.

(6) Nützel, J. F.; Abstreiter, G. Segregation and Diffusion on Semiconductor Surfaces. *Phys. Rev. B* **1996**, *53* (20), 13551–13558. https://doi.org/10.1103/PhysRevB.53.13551.

(7) Arnold, C. B.; Aziz, M. J. Unified Kinetic Model of Dopant Segregation during Vapor-Phase Growth. *Phys. Rev. B* **2005**, *72* (19), 195419. https://doi.org/10.1103/PhysRevB.72.195419.

(8) Hellman, F. Surface-to-Surface Segregation during Growth of Polycrystalline Thin Films. *Appl. Phys. Lett.* **1987**, *51* (12), 948–950. https://doi.org/10.1063/1.98811.

(9) Jorke, H. Surface Segregation of Sb on Si(100) during Molecular Beam Epitaxy Growth. *Surf. Sci.* **1988**, *193* (3), 569–578. https://doi.org/10.1016/0039-6028(88)90454-2.

(10) Rockett, A.; Drummond, T. J.; Greene, J. E.; Morkoc, H. Surface Segregation Model for Sn-Doped GaAs Grown by Molecular Beam Epitaxy. *J. Appl. Phys.* **1982**, *53* (10), 7085–7087. https://doi.org/10.1063/1.330013.

(11) Harris, J. J.; Ashenford, D. E.; Foxon, C. T.; Dobson, P. J.; Joyce, B. A. Kinetic Limitations to Surface Segregation during MBE Growth of III-V Compounds: Sn in GaAs. *Appl. Phys. A Solids Surfaces* **1984**, *33* (2), 87–92. https://doi.org/10.1007/BF00617613.

(12) Zhou, X. W.; Wadley, H. N. G. Mechanisms of Inert Gas Impact Induced Interlayer Mixing in Metal Multilayers Grown by Sputter Deposition. *J. Appl. Phys.* **2001**, *90* (7), 3359–3366. https://doi.org/10.1063/1.1398073.

(13) Zhou, X. W.; Wadley, H. N. G. Atomistic Simulations of the Vapor Deposition of Ni/Cu/Ni Multilayers: The Effects of Adatom Incident Energy. *J. Appl. Phys.* **1998**, *84* (4), 2301–2315. https://doi.org/10.1063/1.368297.

(14) Gilmore, C. M.; Sprague, J. A. A Molecular Dynamics Analysis of Low Energy Atom—Surface Interaction during Energetic Deposition of Silver Thin Films. *Surf. Coatings Technol.* **1992**, *51* (1–3), 324–327. https://doi.org/10.1016/0257-8972(92)90258-C.

(15) Villarba, M.; Jónsson, H. Atomic Exchange Processes in Sputter Deposition of Pt on Pt(111). *Surf. Sci.* **1995**, *324* (1), 35–46. https://doi.org/10.1016/0039-6028(94)00631-8.

(16) Evans, J. W.; Sanders, D. E.; Thiel, P. A.; DePristo, A. E. Low-Temperature Epitaxial Growth of Thin Metal Films. *Phys. Rev. B* **1990**, *41* (8), 5410–5413. https://doi.org/10.1103/PhysRevB.41.5410.

(17) Roling, L. T.; Mavrikakis, M. Toward Rational Nanoparticle Synthesis: Predicting Surface Intermixing in Bimetallic Alloy Nanocatalysts. *Nanoscale* **2017**, *9* (39), 15005–15017. https://doi.org/10.1039/C7NR04779G.

(18) Zhou, X. W.; Wadley, H. N. G. Hyperthermal Vapor Deposition of Copper: Reflection and Resputtering Effects. *Surf. Sci.* **1999**, *431* (1–3), 58–73. https://doi.org/10.1016/S0039-6028(99)00336-2.

(19) Debski, A.; Debski, R.; Gasior, W. New Features of Entall Database: Comparison of Experimental and Model Formation Enthalpies. *Arch. Metall. Mater.* **2014**, *59* (4), 1337–1343. https://doi.org/10.2478/amm-2014-0228.

(20) Chelikowsky, J. R. Predictions for Surface Segregation in Intermetallic Alloys. *Surf. Sci.* **1984**, *139* (2–3), L197–L203. https://doi.org/10.1016/0039-6028(84)90047-5.

(21) de Boer, F. R.; Boom, R.; Mattens, W. C. M.; Miedema, A. R.; Niessen, A. K. *Cohesion in Metals: Transition Metal Alloys*; 1988.

(22) Zhou, X. W.; Wadley, H. N. G. Hyperthermal Vapor Deposition of Copper: Athermal and Biased Diffusion Effects. *Surf. Sci.* **1999**, *431* (1–3), 42–57. https://doi.org/10.1016/S0039-6028(99)00335-0.

(23) Egelhoff, W. F.; Jacob, I. Reflection High-Energy Electron Diffraction (RHEED) Oscillations at 77 K. *Phys. Rev. Lett.* **1989**, *62* (8), 921–924. https://doi.org/10.1103/PhysRevLett.62.921.

(24) Brandbyge, M.; Hedegård, P.; Heinz, T. F.; Misewich, J. A.; Newns, D. M. Electronically Driven Adsorbate Excitation Mechanism in Femtosecond-Pulse Laser Desorption. *Phys. Rev. B* **1995**, *52* (8), 6042–6056. https://doi.org/10.1103/PhysRevB.52.6042.

(25) Bonn, M.; Funk, S.; Hess, C.; Denzler, D. N.; Stampfl, C.; Scheffler, M.; Wolf, M.; Ertl, G. Phonon- versus Electron-Mediated Desorption and Oxidation of CO on Ru(0001). *Science (80-.).* **1999**, *285* (5430), 1042–1045. https://doi.org/10.1126/science.285.5430.1042.

(26) Fischer, M.; van Houselt, A.; Kockmann, D.; Poelsema, B.; Zandvliet, H. J. W. Formation of Atomic Pt Chains on Ge(001) Studied by Scanning Tunneling Microscopy. *Phys. Rev. B* **2007**, *76* (24), 245429. https://doi.org/10.1103/PhysRevB.76.245429.

(27) Windt, D. L. IMD—Software for Modeling the Optical Properties of Multilayer Films. *Comput. Phys.* **1998**, *12* (4), 360. https://doi.org/10.1063/1.168689.

(28) Nevot, L.; Pardo, B.; Corno, J. Characterization of X-UV Multilayers by Grazing Incidence X-Ray Reflectometry. *Rev. Phys. Appliquée* **1988**, *23* (10), 1675–1686. https://doi.org/10.1051/rphysap:0198800230100167500.

(29) Zameshin, A. Probing Atomic Scale Interface Processes Using X-Rays and Ions (Doctoral Dissertation), University of Twente: Enschede, The Netherlands, 2018. https://doi.org/10.3990/1.9789036546508.

(30) L. Vitos; A. V. Ruban; H. L. Skriver; J. Kollár. The Surface Energy of Metals. *Surf. Sci.* **1998**, *411* (1–2), 186–202. https://doi.org/10.1016/S0039-6028(98)00363-X.

(31) Tran, R.; Xu, Z.; Radhakrishnan, B.; Winston, D.; Sun, W.; Persson, K. A.; Ong, S. P. Data Descriptor: Surface Energies of Elemental Crystals. *Sci. Data* **2016**, *3* (1), 160080. https://doi.org/10.1038/sdata.2016.80.

(32) Miedema, A. R.; Dorleijn, J. W. F. Quantitative Predictions of the Heat of Adsorption of Metals on Metallic Substrates. *Surf. Sci.* **1980**, *95* (2–3), 447–464. https://doi.org/10.1016/0039-6028(80)90189-2.

(33) Kim, D.; Giermann, A. L.; Thompson, C. V. Solid-State Dewetting of Patterned Thin Films. *Appl. Phys. Lett.* **2009**, *95* (25), 251903. https://doi.org/10.1063/1.3268477.

(34) Boragno, C.; Buatier De Mongeot, F.; Felici, R.; Robinson, I. K. Critical Thickness for the Agglomeration of Thin Metal Films. *Phys. Rev. B - Condens. Matter Mater. Phys.* **2009**, *79* (15), 1–7. https://doi.org/10.1103/PhysRevB.79.155443.

(35) ter Veen, H. R. J.; Kim, T.; Wachs, I. E.; Brongersma, H. H. Applications of High Sensitivity-Low Energy Ion Scattering (HS-LEIS) in Heterogeneous Catalysis. *Catal. Today* **2009**, *140* (3–4), 197–201. https://doi.org/10.1016/j.cattod.2008.10.012.

(36) Brongersma, H. H.; Draxler, M.; de Ridder, M.; Bauer, P. Surface Composition Analysis by Low-Energy Ion Scattering. *Surf. Sci. Rep.* **2007**, *62* (3), 63–109. https://doi.org/10.1016/j.surfrep.2006.12.002.

(37) Brown, A. M.; Ashby, M. F. Correlations for Diffusion Constants. *Acta Metall.* **1980**, *28* (8), 1085–1101. https://doi.org/10.1016/0001-6160(80)90092-9.

(38) Chu, J. J.; Steeves, C. A. Thermal Expansion and Recrystallization of Amorphous Al and Ti: A Molecular Dynamics Study. *J. Non. Cryst. Solids* **2011**, *357* (22–23), 3765–3773. https://doi.org/10.1016/j.jnoncrysol.2011.07.019.

(39) Shyam, B.; Stone, K. H.; Bassiri, R.; Fejer, M. M.; Toney, M. F.; Mehta, A. Measurement and Modeling of Short and Medium Range Order in Amorphous Ta2O5 Thin Films. *Sci. Rep.* **2016**, *6* (April), 1–7. https://doi.org/10.1038/srep32170.

(40) Zalden, P.; Bichara, C.; van Eijk, J.; Braun, C.; Bensch, W.; Wuttig, M. Atomic Structure of Amorphous and Crystallized Ge15Sb85. *J. Appl. Phys.* **2010**, *107* (10), 104312. https://doi.org/10.1063/1.3380667.

(41) Eberhart, J. G.; Horner, S. Bond-Energy and Surface-Energy Calculations in Metals. *J. Chem. Educ.* **2010**, *87* (6), 608–612. https://doi.org/10.1021/ed100189v.

CHAPTER 3

Intermixing and Segregation during Growth of Transition Metal Thin Films on Si and Al Substrate Layers

In this chapter, we present the layer growth characteristics of several transition metal on Si and Ru-on-Al bilayer systems. The change in surface atomic composition during the growth of TM on Si and Ru-on-Al (LEIS growth profile) is studied using i*n vacuo* high-sensitivity low energy ion scattering (HS-LEIS). The intermixing and segregation characteristics of TM-on-Si and Ru-on-Al systems obtained from their corresponding LEIS growth profile data are compared to the expected characteristics based on the scaling law for intermixing and layer growth models presented in the previous chapter. Al exhibits segregation behavior during Ru-on-Al growth as expected based on the empirical growth model. The effective interface width of Ru-on-Al system follows the scaling law for intermixing. Si shows segregation behavior in all investigated TM-on-Si systems. Nevertheless, the effective interface width values of the investigated TM-on-Si systems, except Zr-on-Si and Ta-on-Si systems, are similar to the predicted values based on the scaling law intermixing. Simultaneous segregation of Si and (Zr, Ta) in Zr-on-Si and Ta-on-Si systems, respectively, results in a thinner interface width than the corresponding values predicted from the scaling law for intermixing.

3.1. INTRODUCTION

Transition metal (TM) thin films are integral components of several electronic and optical devices. The miniaturization trend in these technological devices has been pushing the limits of fabricating TM thin films with nanometer and sub-nanometer thicknesses. The decrease in layer thicknesses from hundreds of nanometers to sub-nanometers has increased the importance of layer growth techniques and intermixing during growth with the underlying layer. Layer materials are usually chosen according to theoretical calculations based on the functional properties of the materials, or they are selected based on known "bulk" material properties. However, it is important to realize that the layer growth properties (roughness, intermixing, and segregation) of the chosen film-substrate layer material combination may strongly influence the final device performance, especially in the case of nanoscale thin film structures.

In our previous work,[1] we have proposed a semi-empirical model to describe the intermixing process during layer growth. The model parameters were extracted from the experimental data of TM-on-TM growth studies. An exponential dependence of interface width on surface energy difference between the film and substrate TM layers, and a sub-trend based on their crystal structure, was revealed. These results serve as a scaling law to predict the effective interface width and intermixing thickness in TM-on-TM systems in general. Furthermore, in addition to the intermixing processes occurring during layer growth, for TM-on-TM systems with large atomic radii differences a strong segregation of larger atoms was observed. In this work, we have investigated the possibilities of extending the growth and interface prediction rules of TM-on-TM systems, to TM growth on other elements such as Al and Si, and discuss the layer growth phenomena involved in these systems. This can be of direct relevance for applications such as gate metal in semiconductor devices, oxidation resistant layers, and radiative emissive layers on nano-membranes.[2–6]

The TM-on-(Al or Si) bilayer samples for layer growth studies were prepared using dc magnetron sputtering in a UHV deposition chamber. The freshly prepared samples were transferred *in vacuo* to a high-sensitivity low energy ion scattering (HS-LEIS) setup to measure the surface atomic composition. The surface coverage evolution as a function of as-deposited film layer thickness ("growth profile") provides key information about the intermixing and segregation processes. More information on the experimental techniques, LEIS growth profile methodology and analysis can be found in the references[1,7,8].

3.2. RESULTS AND DISCUSSION

The LEIS growth profiles for Ru-on-Al and TM-on-Si (TM: Zr, Ta, Mo, Ru, Ir, Pt) systems are shown in Figure 3.1. The growth profile fits are based on Zameshin's segregation model[1,9], with corresponding contributions from film atoms in the absence of substrate segregation and from

segregating substrate atoms. In all the investigated systems, segregation of substrate atoms is observed in addition to the intermixing process. The segregation process can be considered purely a surface effect (floating segregation), as described in the reference[1]. The surface coverage of the segregated substrate atoms increases initially because of the increasing number of arriving film atoms that can initiate the segregation process and it eventually saturates when all the surface exchange sites are covered and additional segregation from the buried substrate layer is hindered. With further increase in film thickness, some of the floating substrate atoms continue to segregate, whereas the rest are removed via grain boundaries and defect sites. This results in decreasing segregated atom coverage with increasing film thickness until there are no more floating substrate atoms. This type of layer growth process, where segregation of substrate atoms (Al and Si in this study) is observed in addition to the intermixing process, is categorized as "type-II" growth (segregation of substrate atoms in addition to intermixing process) in reference[1]. Therefore, all the systems investigated in this work can be considered to show a type-II growth.

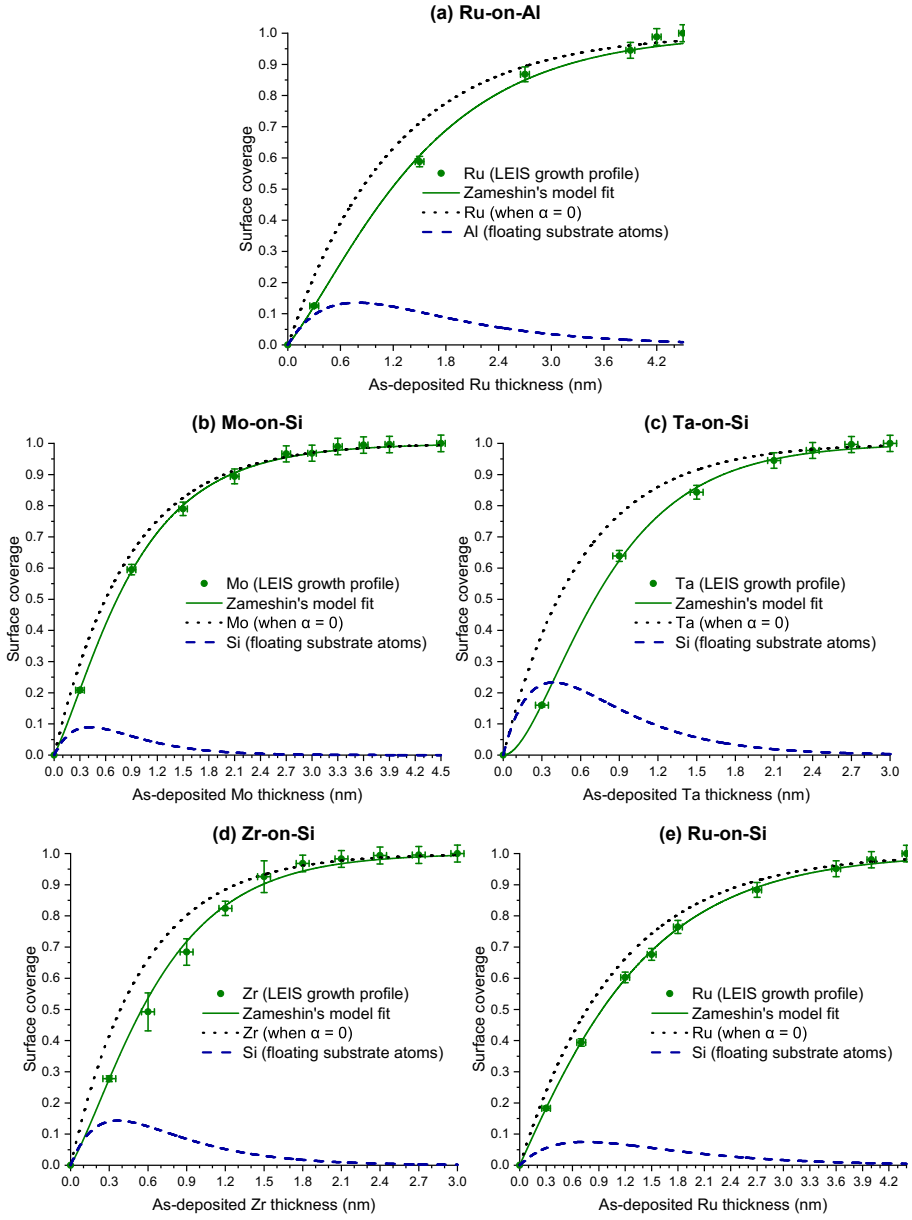

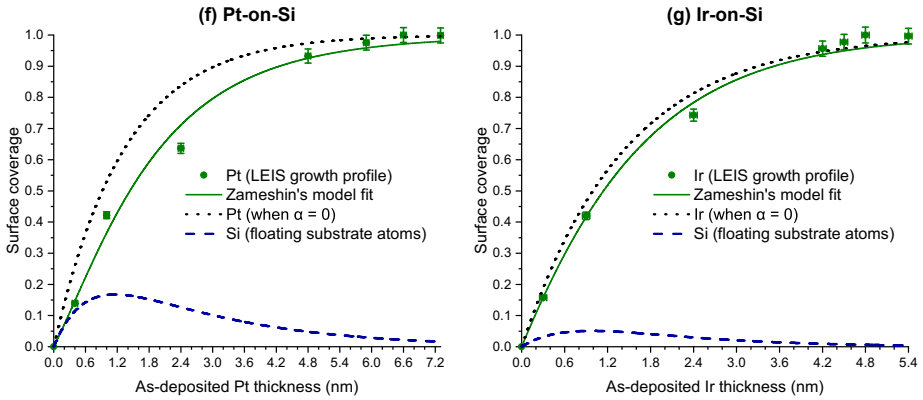

Figure 3.1. LEIS growth profiles of (a) Ru-on-Al system, and (b-g) TM-on-Si systems

In our previous work,[1] an empirical rule (Table 1) was proposed to predict the probable growth profile type in TM-on-TM systems based on the substrate-film atomic radii difference ($r_s - r_f$), enthalpy of mixing, and surface-energy difference between substrate and film atoms. We will now verify if the empirical rules to predict the growth profile of TM-on-TM systems, can explain the type-II growth profile (segregation of substrate atoms in addition to intermixing process) observed for the investigated Ru-on-Al and TM-on-Si systems.

Table 3.1. Empirical rules to predict the probable growth profile type in TM-on-TM systems based on the atomic radii difference ($r_s - r_f$), enthalpy of mixing and surface energy difference, reproduced from Chandrasekaran et al, 2019[1]
*Note: Ag and Au are based on the hypothesis that low melting of Cu is the reason for its floating behavior and not based on experimental evidence.

System	$r_s - r_f$ (Å)	Enthalpy of mixing $\left(\frac{kJ}{mol}\right)$	Probable growth profile type	Element expected to segregate
TM-on-TM	– 0.22 to + 0.12	+ or –	Type-I	-
	> + 0.12	–	Type-II or Type-IV (depending on surface energy difference and size difference)	Substrate
		+	Type-IV	Substrate
	< – 0.22	+ or –	Type-III	Film
Cu(Ag*,Au*)-on-TM	– 0.22 to + 0.12	+ or –	Type-III	Cu(Ag*,Au*)
	> + 0.12	–	Type-II or Type-IV (depending on surface energy difference and size difference)	Substrate
		+	Type-IV	Substrate
TM-on-Cu(Ag*,Au*)	– 0.22 to + 0.12	–	Type-II	Cu(Ag*,Au*)
		+	Type-IV	Cu(Ag*,Au*)
	< – 0.22	+ or –	Type-III	Film

In the case of Ru-on-Al, the substrate-film atomic size difference ($r_s - r_f$) is 0.09 and the enthalpy of mixing[10,11] is negative. It is important to note that the melting temperature of Al (~660°C) is much lower than Cu (~1085°C), which is expected to segregate readily because of the low activation energy for self-diffusion.[12] Therefore, Ru-on-Al should be considered in the TM-on-Cu system category. Based on the empirical rules given in Table 3.1, a type-II growth with segregation of substrate Al atoms is expected for Ru-on-Al system, which is in accordance with the observed LEIS growth profile result.

In the case of Zr-on-Si and Ta-on-Si systems, with $r_s - r_f << -0.22$ Å and a negative enthalpy of mixing, the TM-on-TM empirical rules for growth profile suggests segregation of large atoms (Zr and Ta) in addition to intermixing ("type-III" growth) as it can reduce the strain energy in the system. However, contrary to the prediction, the LEIS growth profile data of these systems show segregation of Si substrate atoms during growth ("type-II" growth). In the case of Mo-on-Si, Ru-on-Si, Ir-on-Si and Pt-on-Si systems, with $-0.16 \text{ Å} > r_s - r_f > -0.22$ Å and a negative enthalpy of mixing, segregation of Si atoms during growth ("type-II" growth) is observed, whereas a type-I growth is expected based on the TM-on-TM empirical rules for growth profile. Similarly, Zameshin et al[13] recently reported segregation of Si in W-on-Si system ("type-II" growth), whereas the empirical rules suggest a type-I growth with no segregation.

It is apparent from the observed results that the growth profile of TM-on-Si systems does not in general follow the empirical rules derived from TM-on-TM growth studies. The atomic size of Si is smaller than TM atoms, and therefore, the segregation behavior of Si in the investigated TM-on-Si systems cannot be explained by strain induced by large atomic size of substrate atoms. The melting temperature of Si (~ 1400°C) is comparatively lower than most TM, which can in principle suggest a low activation energy for self-diffusion. However, is it important to note that Cu, with a lower melting temperature than Si, does not show segregation behavior in Sc-on-Cu system with $r_s - r_f << -0.22$ Å, where the large atomic size difference dominates.[1] Therefore, the fact that Si segregates in Zr-on-Si and Ta-on-Si systems, with $r_s - r_f << -0.22$ Å, suggests that the segregation behavior of Si is not primarily induced by its comparatively lower melting temperature. Although it is clear from the experimental data that Si segregates during growth in TM-on-Si systems, it is not fully obvious what drives the segregation behavior of Si atoms. Further research is required to understand the segregation behavior of Si during growth in TM-on-Si systems, and the physical phenomena involved in Si-on-TM systems.

We will now investigate the possibility of using the TM-on-TM scaling law proposed in reference[1] to predict the effective interface width of Ru-on-Al and TM-on-Si systems, based on the surface energy values and the preferred crystal structures of TMs, Al and Si at normal temperature and

pressure. The surface energy values of Al and Si, taken from de Boer et al, are 1.16 J/m^2 and 1.25 J/m^2, respectively.[11] The surface energies are calculated to be 0.75 eV/atom and 0.92 eV/atom for Al and Si, respectively, according to the method described in reference[1]. The preferred crystal structure of both Al and Si is fcc at normal temperature and pressure. Although Si layers used in this study are amorphous, the scaling law should still be valid because both amorphous and crystalline layers show similar crystal structure properties in short-range order.[14–16] The effective interface width values of Ru-on-Al and TM-on-Si (TM: Zr, Ta, Mo, Ru, Ir, Pt) systems, obtained from their LEIS growth profile fits, are added to the corresponding crystal structure combination chart (fcc-fcc or bcc-fcc or hcp-fcc), as reproduced from reference[1]. It can be clearly seen that the effective interface width values of all investigated systems, except Zr-on-Si and Ta-on-Si, follow the existing exponential trend reasonably well. The effective interface width values of Zr-on-Si and Ta-on-Si systems are significantly lower than the predicted values based on the scaling law. Experimental errors in determining the interface widths can be ruled out especially in the case of Zr, because transmission electron microscope images, X-ray photoelectron spectra, and X-ray reflectivity data of the Zr-on-Si system support the LEIS results presented here.

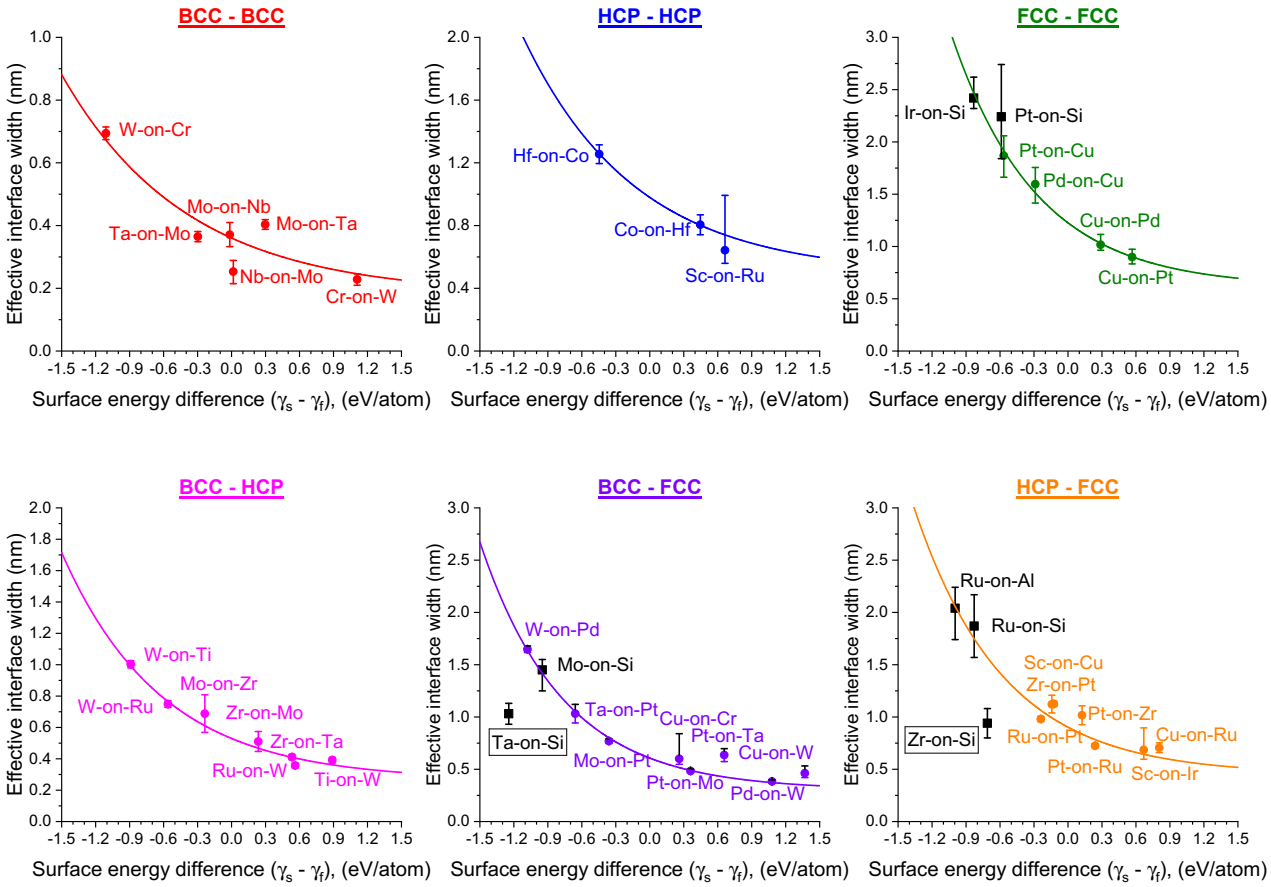

Figure 3.2. Scaling law for effective interface width, reproduced from Chandrasekaran et al, 2019[1].

A possible explanation for the deviation of Zr-on-Si and Ta-on-Si systems from the exponential trend can be based on their growth characteristics. LEIS data of these systems show a type-II growth,

where Si atoms segregate during growth. However, based on the empirical rules given in reference[1], Zr-on-Si and Ta-on-Si systems are expected to exhibit a type-III growth, with segregation of Zr and Ta mainly in the initial stages of growth, up to 0.6-0.9 nm as-deposited film thickness. Although not directly visible in the LEIS growth profile, a simultaneous segregation of TM (Zr, Ta) and Si atoms in the early stages of growth can reduce the number of Si atoms available for further intermixing, which can result in a sharper interface width when compared to a standard intermixing process. The existing model[9] cannot describe segregation of both film and substrate atoms during growth, and therefore, a quantitative analysis is not possible at this moment. Note that also Mo-on-Si, Ru-on-Si, Ir-on-Si and Pt-on-Si show a different growth type (type-II) with segregating Si atoms, compared to the type-I growth with no segregation of atoms expected based on TM-on-TM empirical growth rules. However, in contrast to the case for Zr-on-Si and Ta-on-Si, segregating Si atoms in these systems fundamentally do not affect the intermixing process, and therefore, the effective interface width values follow the scaling law.

3.3. SUMMARY

In summary, layer growth phenomena for a limited number of TM-on-(Al or Si) systems were studied *in vacuo* using LEIS. From the results it is concluded that the prediction rules for growth characteristics and the scaling law for effective interface width obtained from the TM-on-TM data are valid also for the Ru-on-Al system. Additional experiments are required to confirm if all TM-Al systems in general follow the TM-on-TM scaling law and empirical growth rules. For all investigated TM-on-Si systems, Si was observed to exhibit segregation behavior during growth. This suggests a type-II growth for all TM-on-Si systems in general. From the results presented here, it is expected that the effective interface width of TM-on-Si systems in general will follow the scaling law trend except when $r_s - r_f < -0.22$ Å (as in the case of Zr-on-Si and Ta-on-Si), for which the interface width will be sharper than the predicted value because of limited intermixing induced by competing segregation of TM and Si atoms in the early stages of growth. Further studies are required to understand the growth characteristics and segregation behavior of Si in combination with low melting temperature elements, such as Cu, Ag, Au, Al.

3.4. REFERENCES

(1) Chandrasekaran, A.; van de Kruijs, R. W. E.; Sturm, J. M.; Zameshin, A. A.; Bijkerk, F. Nanoscale Transition Metal Thin Films: Growth Characteristics and Scaling Law for Interlayer Formation. *ACS Appl. Mater. Interfaces* **2019**, *11* (49), 46311–46326. https://doi.org/10.1021/acsami.9b14414.

(2) Wang, M. C.; Chang, T.-C.; Liu, P.-T.; Li, Y. Y.; Xiao, R. W.; Lin, L. F.; Chen, J. R. Cu/CuMg Gate Electrode for the Application of Hydrogenated Amorphous Silicon Thin-Film Transistors.

Electrochem. Solid-State Lett. **2007**, *10* (8), J83. https://doi.org/10.1149/1.2739209.

(3) Shim, J. Y.; Kwak, J. S.; Chi, E. J.; Baik, H. K.; Lee, S. M. Formation of Amorphous and Crystalline Phases, and Phase Transition by Solid-State Reaction in Zr Si Multilayer Thin Films. *Thin Solid Films* **1995**, *269* (1–2), 102–107. https://doi.org/10.1016/0040-6090(95)06744-2.

(4) Shang, H.; White, M. H.; Guarini, K. W.; Solomon, P.; Cartier, E.; McFeely, F. R.; Yurkas, J. J.; Lee, W.-C. Interface Studies of Tungsten Gate Metal–Oxide–Silicon Capacitors. *Appl. Phys. Lett.* **2001**, *78* (20), 3139–3141. https://doi.org/10.1063/1.1372340.

(5) Bajt, S.; Dai, Z. R.; Nelson, E. J.; Wall, M. A.; Alameda, J.; Nguyen, N.; Baker, S.; Robinson, J. C.; Taylor, J. S.; Clift, M.; et al. Oxidation Resistance of Ru-Capped EUV Multilayers. In *Emerging Lithographic Technologies IX*; Mackay, R. S., Ed.; SPIE, 2005; Vol. 5751, p 118. https://doi.org/10.1117/12.597443.

(6) Van Zwol, P. J.; Vles, D. F.; Voorthuijzen, W. P.; Péter, M.; Vermeulen, H.; Van Der Zande, W. J.; Sturm, J. M.; Van De Kruijs, R. W. E.; Bijkerk, F. Emissivity of Freestanding Membranes with Thin Metal Coatings. *J. Appl. Phys.* **2015**, *118* (21). https://doi.org/10.1063/1.4936851.

(7) Brongersma, H.; Draxler, M.; Deridder, M.; Bauer, P. Surface Composition Analysis by Low-Energy Ion Scattering. *Surf. Sci. Rep.* **2007**, *62* (3), 63–109. https://doi.org/10.1016/j.surfrep.2006.12.002.

(8) ter Veen, H. R. J.; Kim, T.; Wachs, I. E.; Brongersma, H. H. Applications of High Sensitivity-Low Energy Ion Scattering (HS-LEIS) in Heterogeneous Catalysis. *Catal. Today* **2009**, *140* (3–4), 197–201. https://doi.org/10.1016/j.cattod.2008.10.012.

(9) Zameshin, A. Probing Atmoic Scale Interface Processes Using X-Rays and Ions, University of Twente: Enschede, The Netherlands, 2018. https://doi.org/10.3990/1.9789036546508.

(10) Debski, A.; Debski, R.; Gasior, W. New Features of Entall Database: Comparison of Experimental and Model Formation Enthalpies. *Arch. Metall. Mater.* **2014**, *59* (4), 1337–1343. https://doi.org/10.2478/amm-2014-0228.

(11) de Boer, F. R.; Boom, R.; Mattens, W. C. M.; Miedema, A. R.; Niessen, A. K. *Cohesion in Metals: Transition Metal Alloys*; 1988.

(12) Brown, A. M.; Ashby, M. F. Correlations for Diffusion Constants. *Acta Metall.* **1980**, *28* (8), 1085–1101. https://doi.org/10.1016/0001-6160(80)90092-9.

(13) Zameshin, A. A.; Medvedev, R. V.; Yakshin, A. E.; Bijkerk, F. Interface Formation in W/Si Multilayers Studied by Low Energy Ion Scattering. *Thin Solid Films* **2021**, *724*, 138569. https://doi.org/10.1016/j.tsf.2021.138569.

(14) Chu, J. J.; Steeves, C. A. Thermal Expansion and Recrystallization of Amorphous Al and Ti: A Molecular Dynamics Study. *J. Non. Cryst. Solids* **2011**, *357* (22–23), 3765–3773. https://doi.org/10.1016/j.jnoncrysol.2011.07.019.

(15) Shyam, B.; Stone, K. H.; Bassiri, R.; Fejer, M. M.; Toney, M. F.; Mehta, A. Measurement and Modeling of Short and Medium Range Order in Amorphous Ta2O5 Thin Films. *Sci. Rep.* **2016**, *6* (April), 1–7. https://doi.org/10.1038/srep32170.

(16) Zalden, P.; Bichara, C.; van Eijk, J.; Braun, C.; Bensch, W.; Wuttig, M. Atomic Structure of Amorphous and Crystallized Ge15Sb85. *J. Appl. Phys.* **2010**, *107* (10), 104312. https://doi.org/10.1063/1.3380667.

CHAPTER 4

Nb texture evolution and interdiffusion in Nb/Si layered systems

In this chapter, we present a detailed study on the microstructure evolution and interdiffusion in Nb-Si layered systems. Interlayer formation during early stages of growth in sputter-deposited Nb-on-Si and Si-on-Nb bilayer systems is studied *in vacuo* using high-sensitivity low energy ion scattering technique. An asymmetric intermixing behavior is observed, where the Si-on-Nb interface is ~ 2x thinner than the Nb-on-Si interface, and it is explained by the surface energy difference between Nb and Si. During Nb-on-Si growth, crystallization of the Nb layer occurs around 2.1 nm as-deposited Nb thickness with a strong Nb (110) preferred orientation, which is maintained up to 3.3 nm as-deposited Nb thickness. A further increase in Nb layer thickness above 3.3 nm results in a polycrystalline microstructure with a reduced degree of texture. High resolution cross-sectional transmission electron microscopy imaging is performed on Nb/Si multilayers to study the effect of Nb layer texture on interdiffusion during low-temperature annealing. Nb/Si multilayers with amorphous 2 nm Nb layers and strongly textured 3 nm thick Nb layers, with limited grain boundary pathways for diffusion, show no observable interdiffusion during annealing at 200° C for 8 hours, whereas in a Nb/Si multilayer with polycrystalline 4 nm thick Nb layers, a ~ 1 nm amorphous Nb-Si interlayer is formed at the Si-on-Nb interface during annealing.

4.1. INTRODUCTION

The extensive research work on transition metal – silicon (TM-Si) layered thin film structures is generally motivated by their importance in several technological applications besides interests in exploring the fundamental physics phenomena. The practical applicability of these structures in advanced technologies relies on, and more often is limited by, their interface quality and thermal stability. Both are inherently related to structural properties, such as roughness, density, defects, grain size and preferred orientation[1,2] of individual layers in the stack. For this reason, much efforts have been taken in the past decades to understand the influence of structural properties of constituting layers on the functional properties of thin film devices.

Nb-Si layered systems are widely used in superconductor applications.[3,4] Nb/Si based multilayers have potential application in X-ray optics because of their favorable optical properties, thermal stability, and irradiation damage resistance.[5,6] Thin Nb layers can be used as a barrier in TM/Nb/Si and TM/Nb/SiO_2 systems,[7] which have useful applications in integrated circuits. The existing literature on Nb/Si multilayers unanimously report the asymmetry in interface width (Si-on-Nb interface is thinner than Nb-on-Si) for as-deposited structures, while the diffusion of Si and formation of the Nb_3Si phase at the interface are commonly observed during annealing.[8–11] Nevertheless, an understanding on the influence of structural properties of Nb layers on interdiffusion during annealing is still lacking. For instance, Okolo et al.[12] reported a strong (110) preferred orientation in Nb films that depends on Nb layer thickness and the substrate material. However, to our knowledge, there are no studies in the literature that report the effect of Nb layer texture on interdiffusion at Nb/Si interfaces. This knowledge can be beneficial in the fabrication of Nb layers with improved interface and barrier properties for Nb/Si based thin-film systems.

The aim of this work is to study the microstructure evolution of the Nb layer in the first few nanometers during growth on a Si layer, and investigate the influence of the Nb microstructural properties on the extent of interdiffusion at Nb/Si interfaces during annealing. The near-room-temperature layer growth and intermixing phenomena in Si-on-Nb and Nb-on-Si bilayer systems are studied using *in vacuo* high-sensitivity low energy ion scattering (HS-LEIS). Nb/Si multilayers with different Nb thicknesses are deposited to study the effect of Nb texture on thermal stability using high resolution transmission electron microscopy (HR-TEM).

4.2. EXPERIMENT AND METHODOLOGY

4.2.1. Deposition and Characterization

All samples were deposited using direct-current magnetron sputtering technique on single side polished Si(100) wafers with ~1 nm native oxide and 0.15 ± 0.05 nm root-mean-square (rms) roughness. A bilayer architecture as shown in Figure 4.1 was used for Si-on-Nb and Nb-on-Si LEIS

layer growth studies. Bilayer samples for layer growth studies were deposited in a sputter deposition chamber with in-vacuo sample transfer to a high-sensitivity low energy ion scattering (HS-LEIS) set up. The base pressure of the deposition chamber and the Kr gas working pressure were < $5x10^{-9}$ mbar and $1x10^{-3}$ mbar respectively. Kr sputter gas was chosen instead of conventional Ar sputter gas in order to limit the number of high-energy backscattered neutrals bombarding the growing Nb film layer, which can induce intermixing at early stages of Nb-on-Si growth. The substrate-to-target distance was 8 cm for both materials. Both magnetrons were equipped with a shutter in front to prevent cross-contamination, and a quartz crystal microbalance (QCM) at close proximity to monitor the deposited thickness. The deposition rates of Nb and Si were calibrated using ex-situ grazing incidence X-ray reflectivity (GI-XRR) measurements on Nb and Si layers each with 3 different thicknesses, respectively, for better accuracy. The sputter power values used for Nb and Si were 25 W and 18 W, respectively, and the corresponding sputter voltages were 320 V and 540 V. A low sputter power was chosen for both materials to get a low growth rate (Nb: 0.03 nm/s and Si: 0.05 nm/s), which is important to achieve a sub-nanometer (0.3 nm) growth step. The thickness accuracy of the deposited films is ± 0.05 nm. The Nb/Si multilayer samples, with a 4 nm Si cap to prevent oxidation of the stack, were produced in a Roth & Rau MS1600 deposition system under similar deposition conditions as compared to the depositions for in-vacuo layer growth studies, such as sputter voltage, sputter gas and pressure, and substrate-to-target distance. Hence, similar particle energies and layer microstructure can be expected during growth in both deposition systems.

High-sensitivity low energy ion scattering (HS-LEIS) was used to study the change in surface coverage as a function of as-deposited film layer thickness in Nb-on-Si and Si-on-Nb systems. HS-LEIS measurements were performed using an IONTOF Qtac100 tool with $1x10^{-10}$ mbar base pressure. A 3keV ion beam with 3 nA ion current and a 5 keV ion beam with 1 nA ion current at normal incidence angle were used for He^+ and Ne^+ LEIS measurements, respectively. An Ar^+ sputter gun operating at 59° incidence angle relative to the surface normal with 0.5 keV ion energy and 100 nA ion current was used for sputter depth profile measurements. More information on the HS-LEIS technique can be found in references [13,14].

Grazing incidence X-ray diffraction (GI-XRD) technique was used to investigate the crystalline properties of the multilayer samples. GI-XRD measurements were done using an in-house PANalytical Empyrean X-ray diffractometer with a Cu-Kα source (1.5406 Å). A BRUKER Dimension Edge atomic force microscope (AFM) with a high-resolution tip (MikroMasch HiRes-C15/Cr-Au) was used for surface morphology characterization. The multilayer samples were annealed at 200ºC for 8 hours in a high-vacuum environment to limit oxidation of the layers. High resolution cross-sectional transmission electron microscopy (XTEM) was used to study the structural and interface properties of as-deposited and annealed multilayer samples. XTEM images were obtained using a Philips CM300ST-FEG

transmission electron microscope (300 kV acceleration voltage) at the MESA+ institute, University of Twente. The specimens for XTEM were prepared by creating a symmetrical cross-sectional sandwich structure using dimple grinding/polishing and argon ion thinning methods.[15,16] In the final stages of Ar^+ thinning, the energy of Ar^+ was reduced from 4.5 keV to 0.5 keV to minimize specimen damage.

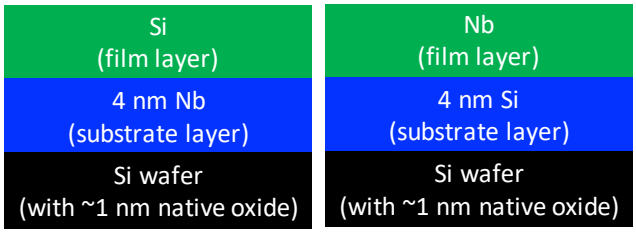

Figure 4.1. Bilayer architecture used for Si-on-Nb and Nb-on-Si layer growth studies

4.2.2. LEIS Growth Profile

Thin film interfaces are usually studied using techniques such as X-ray photoelectron spectroscopy (XPS), X-ray reflectivity (XRR) and XTEM. Using these techniques, it is possible to obtain the interface concentration profile and the effective interface width by considering a suitable thin film model that fits the experimental data well.[17–20] The significance of the HS-LEIS technique is its high surface sensitivity, which when coupled with the *in vacuo* sample transfer facility allows us to measure the evolution of surface coverage during layer growth ("growth profile").[21,22] This provides key information about film layer closing thickness, surface atomic densities, surface segregation, and other surface phenomena during growth that cannot be studied using conventional techniques. In addition, interface profile and effective interface width can also be extracted from LEIS growth profiles by considering an appropriate interface model.[21–23] The following procedure was used to record LEIS spectra for the layer growth studies:

(1) A 4 nm substrate layer was deposited onto a Si wafer, followed by a 0.3 nm film layer
(2) The sample was transferred *in vacuo* to the LEIS chamber and a LEIS spectrum was recorded
(3) A 4 nm substrate layer was deposited onto a new Si wafer, followed by the film layer with a sub-nanometer increase in thickness
(4) Steps 2 and 3 were repeated until the film layer signal during LEIS measurements saturates, which corresponds to a 100% film coverage

A quantitative measurement of the number of surface atoms of a certain element can be obtained from the integral of the corresponding LEIS surface peak after subtracting the background signal. The surface coverage of an element is given by the ratio of the integral of the surface peak in the investigated sample to that of a clean reference sample. Because LEIS cannot distinguish between intermixing and island formation processes during growth, *ex-situ* AFM measurements were done to characterize the surface morphology of the deposited layers.

It has been recently shown that the interface profile between two layers caused by intermixing during deposition near room temperature can be mathematically represented by a logistic function (LGF) of the form:[22,23]

$$C(z) = \frac{1}{1 + e^{\left(\frac{z - z_i}{0.59\,\sigma}\right)}}, \quad (1)$$

where, C is the concentration of the deposited film atom at a depth z from the surface, z_i is the point of inflection of the logistic function and σ is the effective width of the interface. Based on an LGF-like interface model, the expression for the evolution of film atom surface coverage θ as a function of the as-deposited film layer thickness h can be derived as:

$$\theta = 1 - e^{-\left(\frac{h}{0.59\,\sigma}\right)}. \quad (2)$$

The effective interface width of Si-on-Nb and Nb-on-Si systems can be obtained by fitting their respective LEIS growth profiles using Eq. (2), which is comparable to the interface width obtained from XRR spectra assuming an error function like interface model.

4.3. RESULTS AND DISCUSSION

4.3.1. LEIS Layer Growth Studies: Si-on-Nb and Nb-on-Si Bilayer Systems

The He^+ low energy ion scattering (LEIS) spectra of the Si-on-Nb system for various Si thicknesses are shown in Figure 4.2a. The He primary ions that scatter from surface atoms contribute to the surface peaks, whereas ions that scatter from the subsurface atoms (up to ~ 10 nm depth) contribute to the low energy tail. Besides surface peaks of Nb and Si atoms, there is a small contribution from impurity O atoms at the surface, which may arise from the presence of background residual oxygen and water during *in vacuo* sample transfer (~ 7 mins transfer time at $1x10^{-9}$ mbar). AFM images (not shown here) of 0.3 nm and 0.9 nm Si-on-Nb indicate a typical 2D growth with rms surface roughness in the range of ~ 0.2 ± 0.05 nm. This means that the change in surface peak intensity with increasing as-deposited Si thickness is an effect of intermixing during film layer growth and not because of a change in surface morphology.

The surface coverage evolution of Nb, Si and O atoms as a function of as-deposited Si thickness is shown in Figure 4.2b. The reference surface peak integral values for Nb and Si are obtained from their clean reference samples. The reference value for O (1180counts/nC) is taken from the work of Coloma Ribera et al.[21] The surface coverage of Si atoms does not reach 100% even when the Nb surface coverage goes to 0% because of the presence of O atoms at the surface. Because the surface coverage of O is constant for all samples, we use the normalized Si surface coverage values to obtain the effective interface width. The normalized Si LEIS growth profile with an LGF-like interface model fit (Eq. (2)) is shown in Figure 4.2c. The fit based on an LGF-like interface model describes the

experimental data well, and the effective width of the Si-on-Nb interface obtained from the LEIS growth profile fit is 0.47 ± 0.03 nm. The effective interface width obtained from the LEIS growth profile is analogous to the interface width usually obtained from the XTEM and XRR techniques. The as-deposited Si thickness required to obtain a 99% Si surface coverage ("intermixing thickness") is calculated from the LEIS fit as 1.3 nm ± 0.1 nm.

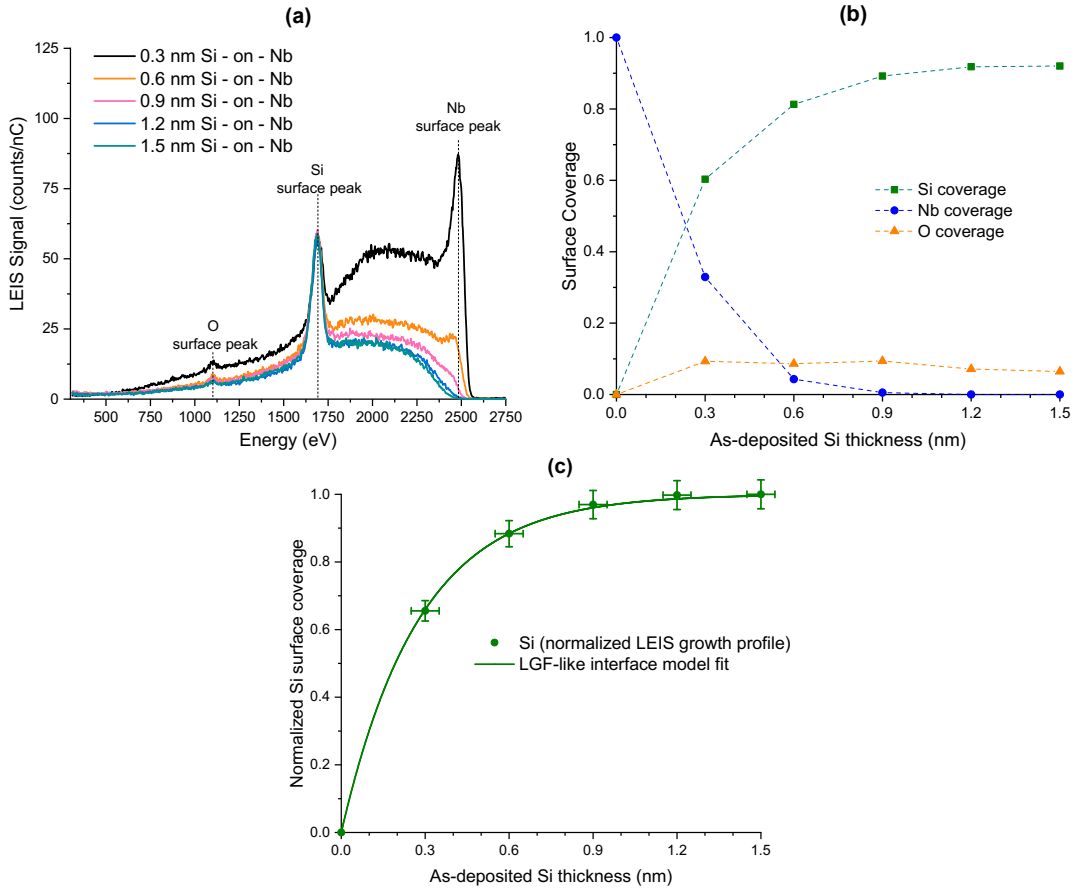

Figure 4.2. (a) He^+ LEIS spectra of Si-on-Nb growth for various as-deposited Si thicknesses, (b) LEIS growth profile of Si, Nb, and O as a function of as-deposited Si thickness, and (c) normalized Si LEIS growth profile with LGF-like interface model fit

A similar approach is taken to study the layer growth of Nb-on-Si. The He^+ LEIS spectra of the Nb-on-Si system for various Nb thicknesses are shown in Figure 4.3. AFM images (not shown here) show a typical 2D growth with rms surface roughness in the range of 0.2 ± 0.05 nm, again indicating that the observed changes in LEIS spectra are because of intermixing and not surface morphology. The Nb-on-Si LEIS spectra show two peculiar features as indicated in Figure 4.3b: (i) at 2.1 nm as-deposited Nb thickness, the intensity of the low energy Nb tail close to the Nb surface peak drops significantly, (ii) reduction in Nb surface peak intensity after 3.3 nm as-deposited Nb thickness.

To understand the drop in intensity near the surface peak at 2.1 nm Nb (feature (i)), it is important to look in more detail to the origin of the low energy Nb tail in the LEIS spectra.[13,24] The 3 keV He primary ions are neutralized once they enter the surface layer because of high neutralization probability. The neutral He atoms that backscatter from subsurface Nb atoms have to be reionized at

the surface level in order to be detected. Therefore, the shape and intensity of the low energy Nb tail depends both on the number of He neutrals backscattered from the Nb atoms distributed in depth, and the probability of reionization of these neutrals at the surface level. The reionization probability is material specific and is influenced by the surface composition.[13,24] However, a small change in surface composition from 1.8 nm to 2.1 nm of Nb – on – Si alone cannot explain the observed change in the slope and intensity of the low energy tail near the surface peak. The absence of other surface peaks except Nb eliminates the role of surface contamination, while surface roughness can be excluded because of low rms roughness values obtained from AFM images. Hence, the change in low energy tail is not because of surface effects but has to be caused by subsurface effects. The number of He neutrals backscattered from the bulk depends on the in-depth Nb concentration. A decrease in the Nb concentration in the subsurface layers would result in a reduced tail intensity close to the Nb surface peak. However, the possibility of Nb atoms being physically absent in the subsurface layers is highly unlikely because of negligible bulk diffusion near room temperature.

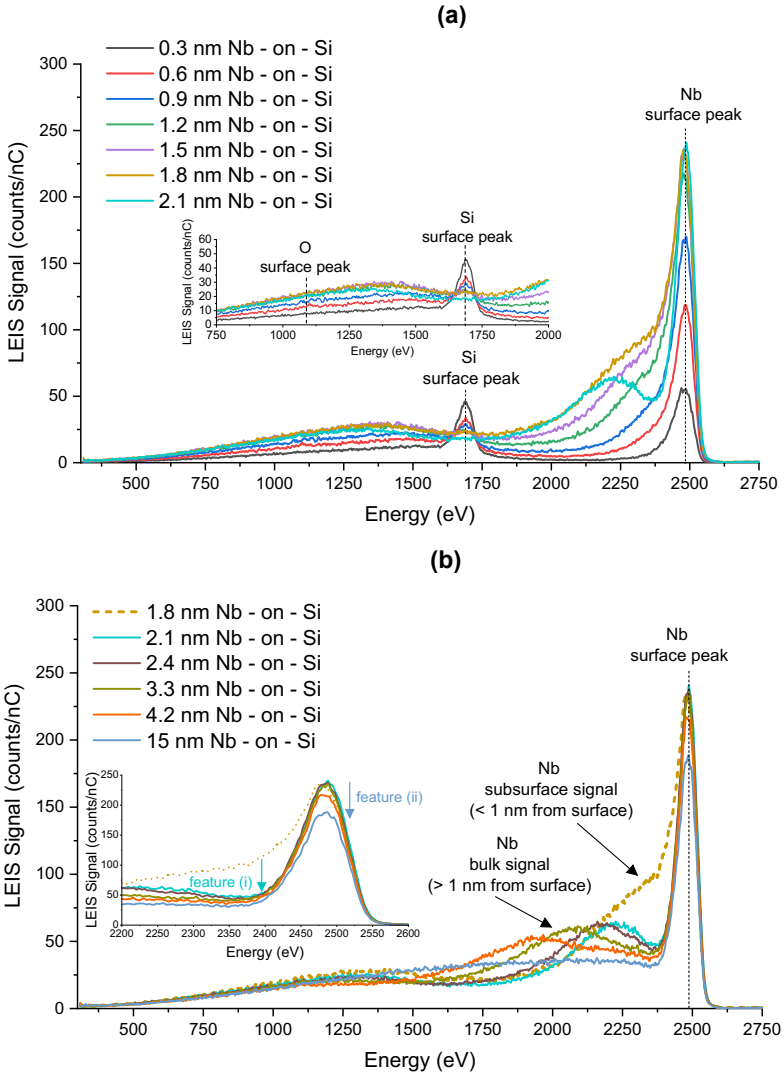

Figure 4.3. He^+ LEIS spectra of Nb-on-Si growth split into two figures for better visibility: (a) 0.3 nm to 2.1 nm as-deposited Nb thickness, (b) 1.8 nm to 15 nm as-deposited Nb

Another possible reason for a drop in the low energy tail intensity close to the surface peak is the "shadowing" of subsurface atoms by surface atoms as shown in Figure 4.4a, which leads to channeling of He neutrals through subsurface layers into bulk layers without backscattering. This effect is normally observed in single crystalline layers under a specific geometry, and it results in a strong reduction in the backscattering contribution from the subsurface layers.[25,26] During the growth of metal on Si layers in metal/Si multilayers, an abrupt crystallization of the metal layer is usually observed around an as-deposited metal thickness of 2-3 nm, resulting in typically 1 nm of crystalline metal layer on top of an amorphous metal-Si intermixed zone.[27] In order to verify the Nb crystallization step around 2.1 nm, a LEIS sputter profile measurement was performed on a Nb-on-Si sample after the crystallization step. The 500 eV Ar^+ sputtering is expected to result in amorphization of the crystalline Nb layer, which should eliminate the channeling effect (Figure 4.4b), and thereby, increase the backscattering contributions from the subsurface Nb atoms to the pre-crystallization level. Figure 4.5 shows the LEIS sputter depth profile measurement of a 2.4 nm Nb – on – Si sample, in which the expected increase in the intensity of the low energy tail just below the surface peak can be seen after Ar^+ sputtering. The tail contribution from deeper amorphous Nb-Si intermixed layers remains unaffected. The elimination of channeling effect by sputter-ion induced amorphization confirms crystallization of Nb around 2.1 nm as-deposited thickness. Note that the increase in Nb surface peak signal after sputtering is because of the removal of residual H and OH at the surface.

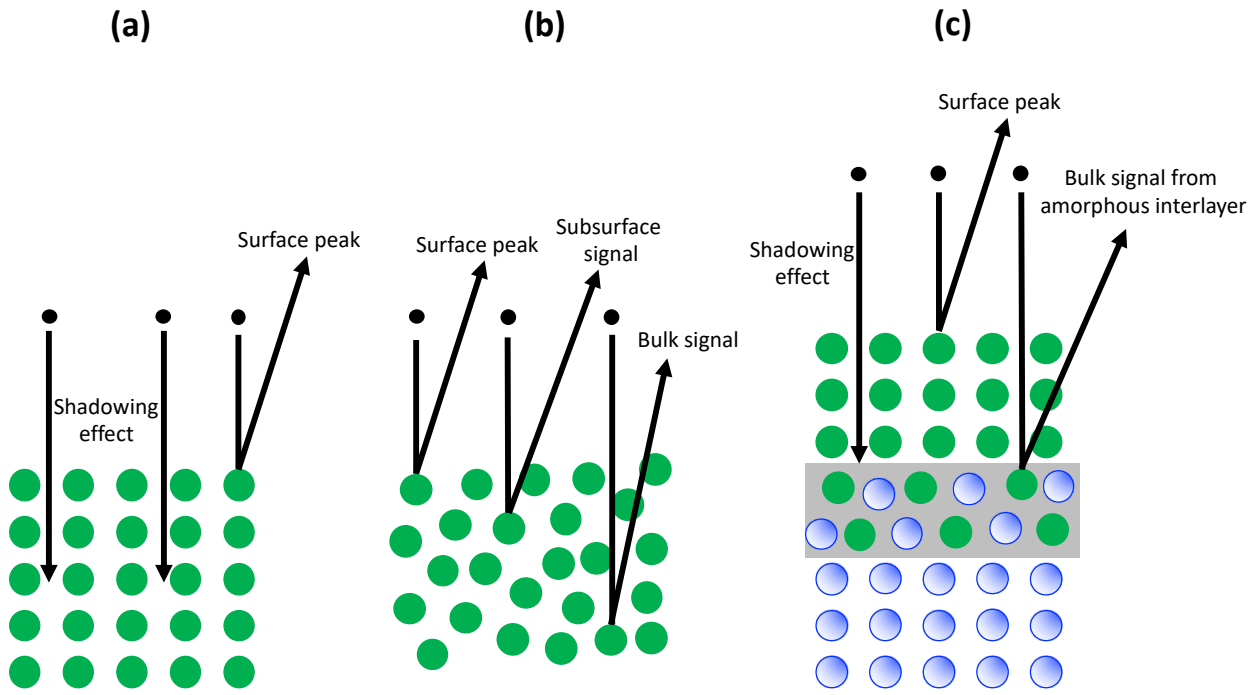

Figure 4.4. Schematic representation of low-energy ion scattering from: (a) crystalline layer, (b) amorphous layer, (c) crystalline film layer with an amorphous interlayer at the interface between film layer and substrate layer

A Nb crystallization step around 2.1 nm is a reasonable explanation for the drop only in the subsurface Nb tail contribution (crystalline part), while the contribution from the deeper amorphous intermixed zone remains unaffected (Figure 4.4c). However, it is important to note that sputter deposited metals usually form a polycrystalline structure after crystallization, in which the channeling effect is expected to be insignificant. Therefore, a highly textured (preferred orientation) Nb layer must be formed after crystallization for channeling to occur. The most densely packed (hkl) plane is generally preferred during the layer growth because of the low surface energy. For bcc metals, the densely packed (110) plane has the lowest surface energy when compared to other (hkl) planes,[28] and therefore, it is likely that bcc Nb layers show a (110) preferred orientation during Nb-on-Si growth. A strong texture in sputter deposited Nb layers with (110) preferred orientation has also been reported before.[11,12] We will later show the GI-XRD results of Nb/Si multilayers studied in this work, which confirm the Nb (110) preferred orientation after crystallization. Based on these evidences, it is possible to conclude that a strongly textured Nb layer is formed after the crystallization step around 2.1 nm during the growth of Nb-on-Si.

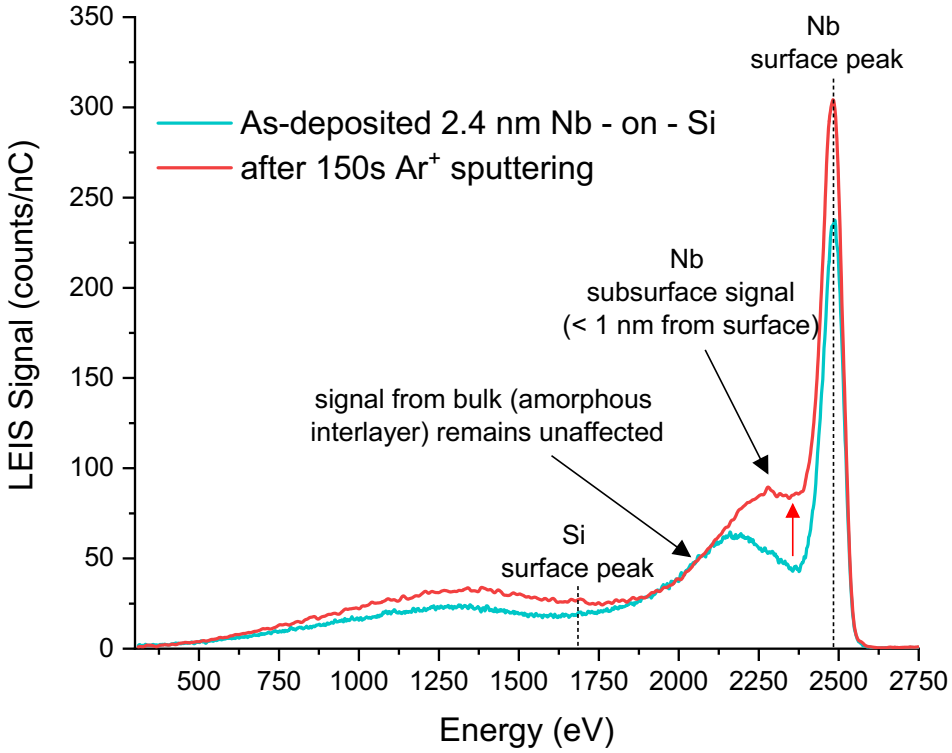

Figure 4.5. He^+ LEIS spectra of 2.4 nm Nb – on – Si: as-deposited and after 500 eV Ar^+ sputtering for 150s

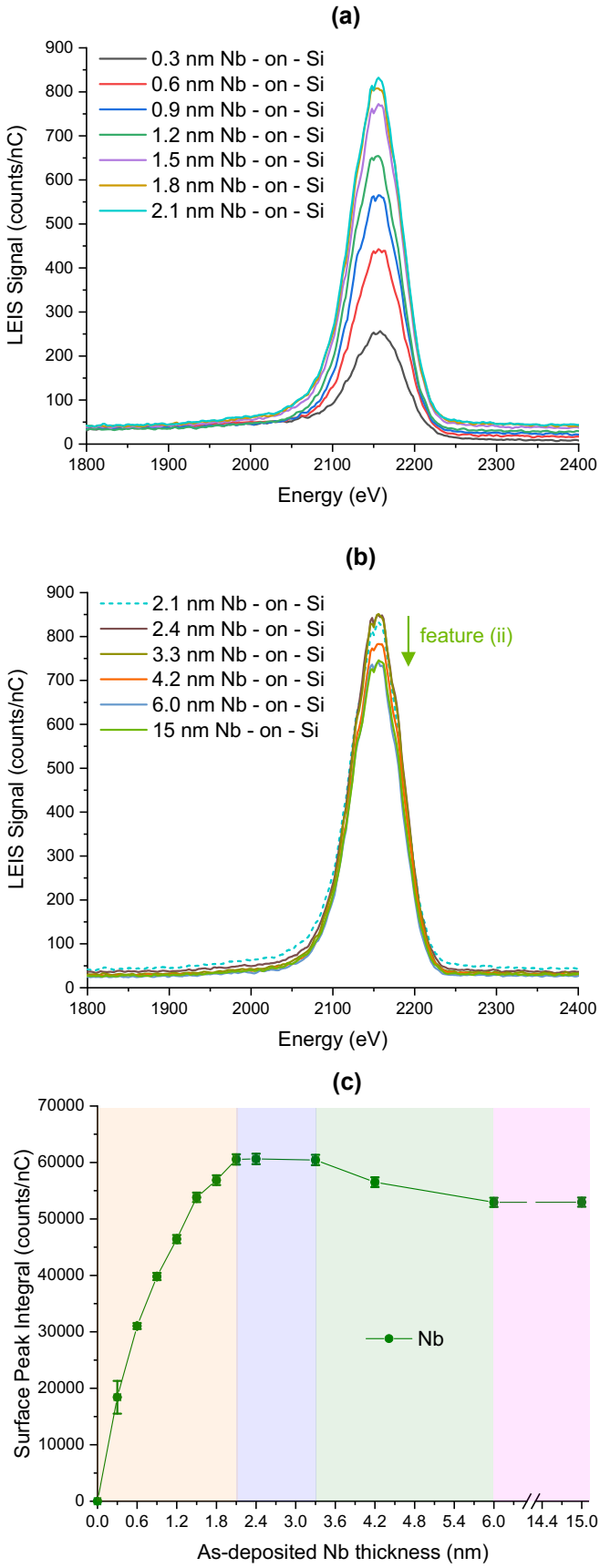

Figure 4.6. Ne^+ LEIS spectra of Nb-on-Si growth split into two figures for better visibility: (a) 0.3 nm to 2.1 nm as-deposited Nb thickness, (b) 2.1 nm to 15 nm as-deposited Nb thickness, and (c) Nb surface peak integral as a function of as-deposited Nb thickness

The feature (ii) observed in the Nb-on-Si LEIS spectra (Figure 4.3b) is the reduction in Nb surface peak intensity for Nb thicknesses above 3.3 nm. The complex shape of the tail in the case of Nb-on-Si LEIS spectra makes it difficult to subtract the background for the calculation of Nb surface peak integral. In order to overcome this problem, we use Ne^+ for LEIS measurements on newly prepared Nb-on-Si samples, for which the intensity of the low energy tail is considerably lower than in He^+ measurements, and therefore, its impact on the surface peak is negligible. The Ne^+ LEIS spectra of Nb-on-Si growth are shown in Figure 4.6a and Figure 4.6b, and the surface peak integral value for each Nb thickness is shown in Figure 4.6c. The Nb surface peak integral value increases up to around 2.1 nm Nb and then starts to decrease from 3.3 nm Nb up to 6 nm Nb, after which it saturates around 53000 counts/nC. As the surface peak integral is a direct measure of the number of surface atoms, a decrease in integral value implies a decrease in the number of Nb surface atoms. In the absence of other elements at the surface, the decrease in Nb surface signal can be caused by a reduction in density as a result of a porous growth, or by a significant change in Nb crystal orientations, resulting in a net change in the surface atomic density. A porous layer with ~15% lower density than bulk layer is required to explain the observed decrease in surface peak integral. Low-pressure magnetron sputtering deposition generally produces high density films and hence, a porous layer growth is highly unlikely. Thus, the reduction in surface peak integral between 3.3 nm and 6 nm as-deposited Nb thicknesses suggests a change in surface atomic density due to the structural evolution of the Nb layer. The observed LEIS growth profile can be explained by a textured Nb growth with high surface density planes up to 3.3 nm, followed by a polycrystalline growth with a reduced average surface atomic density up to 6 nm. We will later show the GI-XRD and XTEM results of Nb/Si multilayers that support this explanation.

It is important to note that the surface peak integral reaches a value of ~ 53000 counts/nC (similar to 6 nm and 15 nm Nb) already at 1.5 nm Nb even in the presence of ~ 8% Si surface coverage, which indicates a preference toward high surface atomic density even before the crystallization step. This suggests that the tendency to form a high surface density structure is most likely influenced by the Si substrate atoms. In our previous work,[22] we showed the importance of surface energy and strain energy on intermixing and segregation processes during growth. The low surface energy of Si facilitates the diffusion of Si to the surface during Nb-on-Si growth. However, the strain induced by a large size difference between Nb and Si (~ 0.28 Å) facilitates surface segregation of the large atom,[22] Nb in this case. The need to compete against the low surface energy Si in order to limit the Nb-Si intermixing, which would lead to a large strain energy, stimulates the textured growth of Nb layer with high surface density (110) preferred orientation, (i.e.) lowest possible Nb layer surface energy. Further increase in Nb thickness leads to a polycrystalline growth with other low surface density planes in addition to the high surface density (110) plane. Okolo et al[12] showed a greater degree of Nb texture

on an amorphous Si_3N_4 substrate when compared to an amorphous SiO_2 substrate. The authors explain this based on the difference in chemical interaction between Nb-O and Nb-N. However, we believe this is because of a stronger intermixing between Nb and Si during Nb-on-Si_3N_4 growth when compared to SiO_2, which facilitates a greater degree of textured growth on Si_3N_4. Coloma Ribera et al[21] showed that the intermixing length of Ru-on-Si > Ru-on-Si_3N_4 > Ru-on-SiO_2. Therefore, assuming a similar growth for Nb on Si, Si_3N_4 and SiO_2, the Nb texture is expected to be stronger on Si > Si_3N_4 > SiO_2 substrate layers. Furthermore, Okolo et al[12] showed an increased Nb layer texture for sputter cleaned substrates when compared to uncleaned substrates. The intermixing between Nb and Si (from Si_3N_4 and SiO_2 substrate layers) can be expected to be greater in the absence of surface contamination. This leads to an increased degree of Nb texture for cleaned substrates when compared to uncleaned substrates.

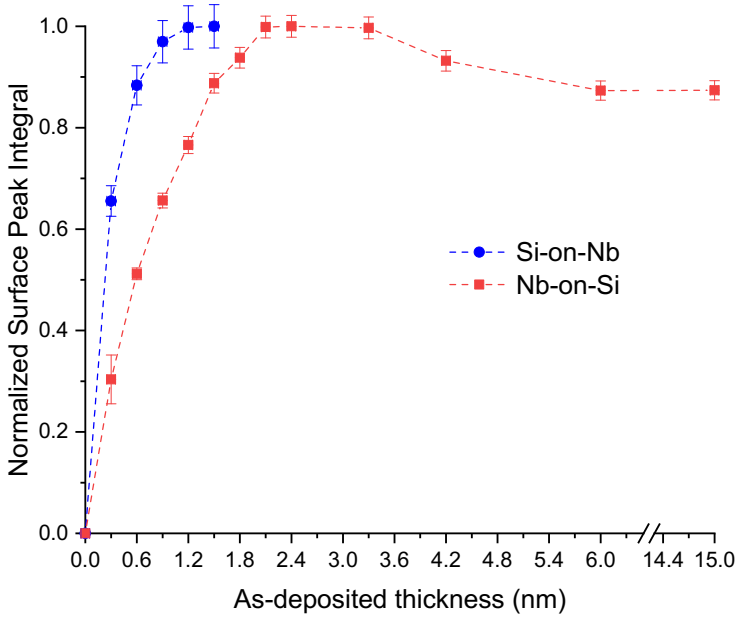

Figure 4.7. Normalized He^+ LEIS surface peak integral of Si-on-Nb system and normalized Ne^+ LEIS surface peak integral of Nb-on-Si system

Because of Nb structural evolution up to 6 nm as-deposited thickness, it is not possible to consider a suitable Nb surface peak integral reference for the surface coverage calculation. The accuracy of the Nb reference surface peak integral is critical for the Nb surface coverage calculation, which in turn determines the value of effective interface width obtained from the growth profile fit. The complexity in Nb layer surface evolution because of strong structural changes makes the LEIS growth profile fit based on a simple LGF-like interface model unreliable. For this reason, it is not possible to obtain an accurate value for the Nb-on-Si effective interface width from LEIS results. Nevertheless, comparing the normalized surface peak integral of Nb-on-Si and Si-on-Nb (Figure 4.7), it is possible to claim that the intermixing thickness of Nb-on-Si interface is ~ 2 times as that of Si-on-Nb. This means that the effective interface width of Nb-on-Si can be expected to be ~ 1 nm, which is confirmed by the XTEM results shown in the next section. This asymmetry in interface thicknesses

has been reported before for Nb/Si systems,[11] other TM/Si systems,[21,29–31] and also for TM-on-TM systems.[22] The reason for the asymmetry is mainly because of the surface energy difference between Nb (1.85 eV/atom) and Si (0.92 eV/atom).[22,32] The low surface energy Si tends to move to the surface during growth to reduce the net surface free energy of the system. This leads to an increased intermixing during Nb-on-Si growth when compared to Si-on-Nb growth, where low energy Si is the film layer.

4.3.2. Interface Diffusion Studies: As-deposited and Annealed Nb/Si Multilayer

The Nb-on-Si LEIS growth studies suggest crystallization of the Nb layer around 2.1 nm as-deposited thickness, followed by a textured growth with high surface density planes up to 3.3 nm Nb thickness, and a polycrystalline growth with reducing average surface atomic density from 3.3 nm to 6 nm. The structural properties of the Nb layer can influence the diffusion of atoms through interfaces at high temperatures. In order to study the effects of Nb structure on interdiffusion during annealing, three different Nb/Si multilayers with 4 nm Si layers and Nb thicknesses of 2 nm, 3 nm, and 4 nm were deposited, which, from now on, will be referred to as Nb-2, Nb-3 and Nb-4 multilayers respectively. As the intention of this study is to measure the interdiffusion at the interfaces without destroying the overall multilayer structure, Nb/Si multilayers were annealed at 200° C for 8 hours, for which interdiffusion effects are expected to be visible without significant structural modifications.[11]

The GI-XRD results of as-deposited Nb/Si multilayers are shown in Figure 4.8a. The higher order diffraction peaks are strongly suppressed in the Nb-2 multilayer, which suggests that the 2 nm Nb layers are quasi-amorphous or nanocrystalline with a short range order. The broad peak around 38° is due to collective scattering from the nearest neighbors in the Nb layer. The GI-XRD spectra of Nb-3 and Nb-4 multilayers indicate a polycrystalline bcc Nb structure. The intensities of diffraction peaks from a polycrystalline sample are expected to scale with the grain size and the thickness of the diffracting layer. However, in the case of the Nb-3 multilayer, intensity of the (110) peak is lower than that of the Nb-2 multilayer, whereas other diffraction peaks are dominant. An incidence angle (ω) scan with diffraction angle (2θ) fixed at 38° (Figure 4.8b) shows a steep increase in intensity around $\omega = \frac{1}{2} 2\theta$, whereas the ω scans of other diffraction peaks with 2θ fixed at their respective diffraction angles (not shown here) show an exponential drop in intensity with increasing ω. This implies a strong Nb (110) preferred orientation parallel to the surface in the Nb-3 multilayer. The ω scan of the Nb-4 multilayer shows a reduced degree of Nb (110) preferred orientation when compared to the Nb-3 sample. This reduction in the degree of preferred orientation of the highest density (110) planes between 3 nm and 4 nm Nb layers, (i.e.) a polycrystalline growth, is in accordance with the reduction in the Nb surface peak integral observed in the LEIS data (Figure 4.6c).

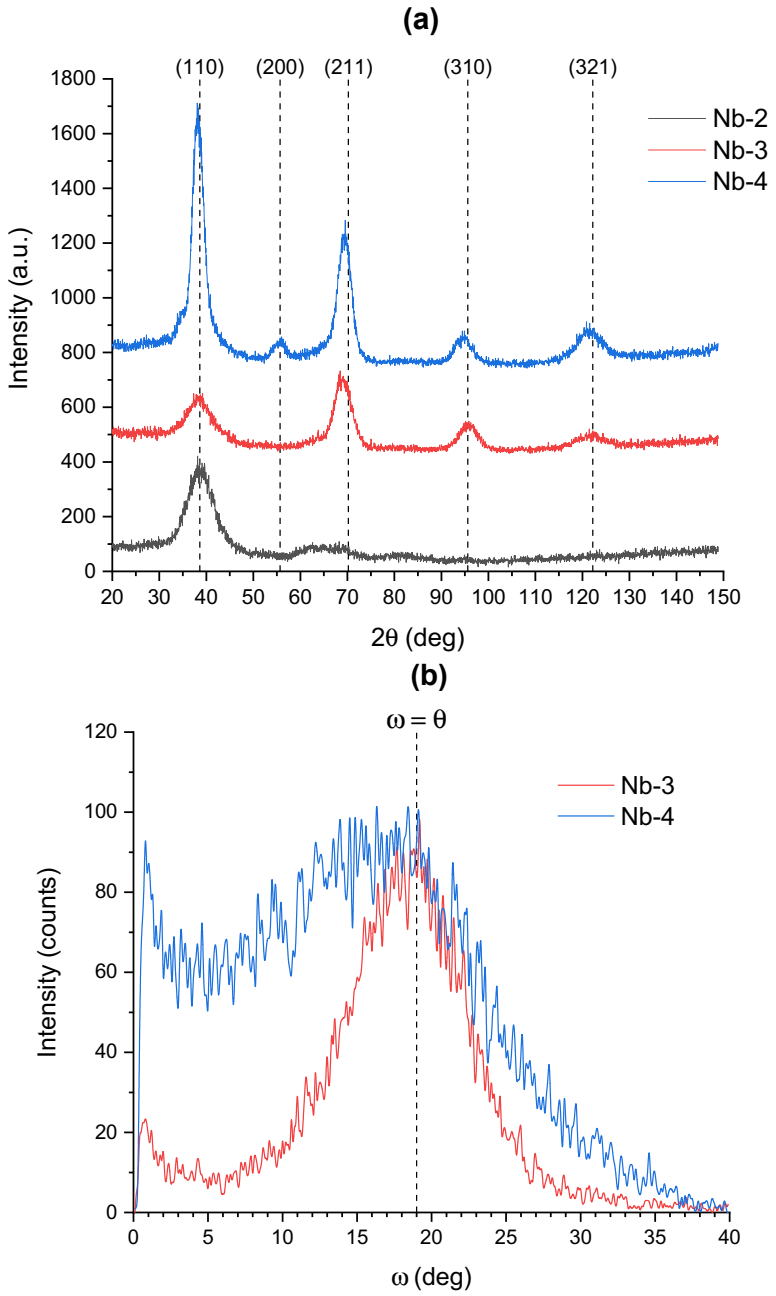

Figure 4.8. (a) GI-XRD spectra of Nb/Si multilayers, (b) incident angle [ω] scan with 2θ at 38° of Nb-3 and Nb-4 multilayers

High resolution cross-sectional transmission electron microscope (XTEM) images were used to study the layer and interface changes in the multilayers after annealing. XTEM images of as-deposited and annealed Nb/Si multilayers are shown in Figure 4.9. The Si layers are amorphous in all as-deposited and annealed multilayer samples, whereas the Nb layers are quasi-amorphous in the Nb-2 multilayer and crystalline in Nb-3 and Nb-4 multilayers. The magnified regions in the Nb layers are shown to enhance the visibility of the Nb layer structure. The 3 nm Nb layers show a strong preferred orientation with planes predominantly parallel to the surface, whereas other orientations in addition to the planes parallel to the surface can be seen in the 4 nm Nb layers. The structure of Nb layers did not change after annealing in all three multilayers, as expected for a lower temperature annealing at 200° C.

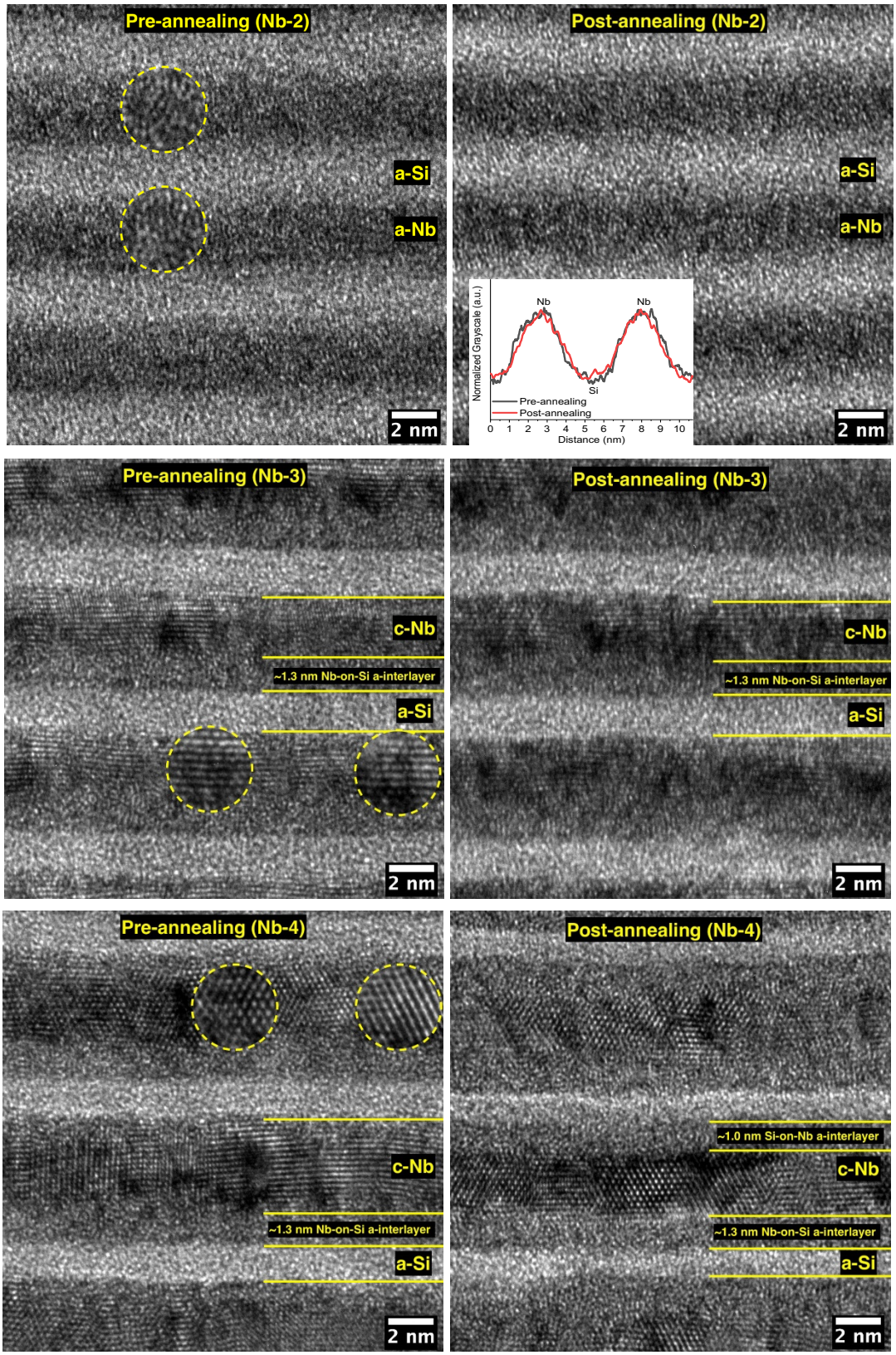

Figure 4.9. XTEM images of Nb/Si multilayers pre- and post-annealing

In the Nb-2 multilayer, the interfaces between the Nb and Si layers cannot be accurately resolved due to low contrast between quasi a-Nb and a-Si layers. Nevertheless, the shape of the line profiles (shown in inset) of the as-deposited and annealed structures is identical, which suggests negligible interdiffusion at the interfaces as a result of annealing. In the as-deposited Nb-3 multilayer,

a ~ 1.3 nm thick amorphous Nb-on-Si interface can be seen. The polycrystalline Nb layers extend all the way up to the following (top) Si layer, indicating a sharp Si-on-Nb interface. Because of negligible solubility of Si and Nb in each other at 200° C,[33,34] interdiffusion between Nb and Si during annealing in general will lead to solid state amorphization of the polycrystalline Nb layer and formation of an intermixed Nb-Si amorphous interlayer. As Nb layer and both interfaces remain unchanged within the resolution of the XTEM after annealing, it is possible to conclude that significant interdiffusion did not occur during annealing at 200° C in Nb-3 multilayer sample. The Nb-on-Si and Si-on-Nb interfaces in as-deposited Nb-4 multilayer are similar to that of as-deposited Nb-3 multilayer. However, after annealing, although the Nb-on-Si interface remains unaltered similar to the case of Nb-3 multilayer, formation of a ~1 nm thick amorphous interlayer at the Si-on-Nb interface can be clearly seen. This suggests a strong interdiffusion at the Si-on-Nb interface during annealing at 200° C. The thickness reduction after annealing in the polycrystalline Nb and the amorphous Si layers is ~ 1 nm and ~ 0.5 nm respectively, indicating that the amorphous interlayer formed at the Si-on-Nb interface is mostly Nb-rich. This is also in accordance with previous studies,[8–11] which show the formation of a Nb_3Si phase above 300° C.

Interdiffusion of layer materials during low temperature annealing (100° C – 250° C) is a commonly observed phenomenon in metal/silicon systems.[35,36] At these temperatures, grain boundary diffusion is generally more dominant when compared to vacancy diffusion through the bulk. Therefore, interdiffusion in Nb-4 multilayer during annealing at 200° C can be explained by thermally activated diffusion of Si atoms into the Nb layer, which is enhanced by the presence of grain boundaries in the polycrystalline Nb layer. Although Nb layers in Nb-3 multilayer are also polycrystalline, they are strongly textured when compared to Nb layers in the Nb-4 multilayer. This results in a reduced number of grain boundaries, and thereby restricts the available pathways for Si diffusion.[1] In the case of the Nb-2 multilayer, the absence of grain boundaries because of the quasi amorphous nature of the Nb layers and the presence of trap (defect) sites can strongly limit interdiffusion. Hence, Nb-2 and Nb-3 multilayers show greater thermal stability at 200° C when compared to Nb-4 multilayer. Note that the Nb-on-Si interface remains unaffected in all three samples. This can be because of the presence of ~ 1.3 nm thick amorphous Nb-Si interlayer formed during growth that can act as a barrier in preventing further interdiffusion through that interface in all three multilayer samples.

Finally, it is important to realize that thermally activated interdiffusion in nanoscale thin film structures initiates several distinct temperature dependent processes, such as solid state amorphization, phase formation and crystallization. In this work, we have taken the first step in understanding the structural evolution of Nb layers during Nb-on-Si growth, and its importance on interdiffusion during low temperature annealing. Further work is required to understand the effect of Nb layer texture on complex physical processes activated at higher temperatures.

4.4. SUMMARY AND CONCLUSIONS

LEIS growth profiles were used to study intermixing phenomena during early stages of growth in sputter deposited Nb-on-Si and Si-on-Nb systems. A decrease in Nb LEIS tail and surface peak intensities was observed during Nb-on-Si growth, which was attributed to crystallization and microstructure evolution of the Nb layer during growth. GI-XRD and XTEM studies were performed on Nb/Si multilayers, with different Nb thicknesses, to confirm the microstructure evolution of the Nb layer, and investigate the effect of the Nb layer texture on interdiffusion during low-temperature annealing at 200° C.

The following conclusions are derived:

- The as-deposited Si-on-Nb interface width is 0.47 ± 0.03 nm, which is approximately twice as sharp as the Nb-on-Si interface. The asymmetry in interface width is explained by the difference in surface energy between Si and Nb atoms. The low-surface-energy Si atoms tend to move toward the surface during growth, resulting in a wider intermixing zone during Nb-on-Si growth when compared to Si-on-Nb growth.
- During Nb-on-Si growth, Nb crystallizes around 2.1 nm as-deposited thickness with a strong Nb (110) preferred orientation. The large size difference between Nb and Si atoms can increase the strain energy at the Nb-on-Si intermixed zone, which is expected to stimulate the low surface energy Nb (110) preferred orientation during crystallization of the Nb layer. The textured growth continues up to 3.3 nm as-deposited Nb thickness, and further increase in Nb thickness results in a polycrystalline microstructure with a reduce degree of texture.
- Nb/Si multilayers with amorphous 2 nm Nb layers and strongly textured 3 nm Nb layers show no noticeable changes in structure during low-temperature annealing at 200° C because of the absence or limited number of grain-boundary pathways for diffusion of Si atoms. In Nb/Si multilayer with 4 nm polycrystalline Nb layers, diffusion occurs via grain boundaries resulting in a ~1 nm amorphous interlayer at the Si-on-Nb interface. The Nb-on-Si interface remains unaltered because of the presence of a ~1.3 nm amorphous interlayer that was formed during growth, which acts as a barrier layer in preventing further diffusion through that interface during low-temperature annealing.

As an overall conclusion, microstructural properties of metal layers in metal-Si thin film systems play a crucial role in determining thermal stability in the low-temperature regime (up to ~ 300° C), where grain boundary diffusion is expected to be the most dominant mechanism. Limiting grain-boundary pathways by stimulating textured growth or preventing crystallization of thin metal layers, may provide the possibility to improve the thermal stability and device performance.

4.5. REFERENCES

(1) Takeyama, M.; Noya, A.; Fukuda, T. Thermal Stability of Cu/W/Si Contact Systems Using Layers of Cu(111) and W(110) Preferred Orientations. *J. Vac. Sci. Technol. A Vacuum, Surfaces, Film.* **1997**, *15* (2), 415–420. https://doi.org/10.1116/1.580500.

(2) Maniruzzaman, M.; Takeyama, M. B.; Hayasaka, Y.; Aoyagi, E.; Noya, A. Formation of Preferentially Oriented Cu [111] Layer on Nb [110] Barrier on SiO 2. *Japanese J. Appl. Physics, Part 2 Lett.* **2004**, *43* (12 B), 1565–1568. https://doi.org/10.1143/JJAP.43.L1565.

(3) Zaytseva, I.; Abal'oshev, O.; Dłużewski, P.; Paszkowicz, W.; Zhu, L. Y.; Chien, C. L.; Kończykowski, M.; Cieplak, M. Z. Negative Hall Coefficient of Ultrathin Niobium in Si/Nb/Si Trilayers. *Phys. Rev. B* **2014**, *90* (6), 060505. https://doi.org/10.1103/PhysRevB.90.060505.

(4) Yusuf, S. M.; Iii, R. M. O.; Jiang, J. S.; Sowers, C. H.; Bader, S. D.; Fullerton, E. E.; Felcher, G. P. Magnetic Profile in Nb/Si Superconducting Multilayers. Journal of Magnetism and Magnetic Materials. *J. Magn. Magn. Mater.* **1999**, *199*, 564–566.

(5) Modi, M. H.; Rai, S. K.; Idir, M.; Schaefers, F.; Lodha, G. S. NbC/Si Multilayer Mirror for next Generation EUV Light Sources. *Opt. Express* **2012**, *20* (14), 15114. https://doi.org/10.1364/OE.20.015114.

(6) Ichimaru, S.; Ishino, M.; Nishikino, M.; Hatayama, M.; Hasegawa, N.; Kawachi, T.; Maruyama, T.; Inokuma, K.; Zenba, M.; Oku, S. Irradiation Damage Test of Mo/Si, Ru/Si and Nb/Si Multilayers Using the Soft X-Ray Laser Built at QST. In *X-Ray Lasers 2016*; Kawachi, T., Bulanov, S. V, Daido, H., Kato, Y., Eds.; Springer International Publishing: Cham, 2018; pp 303–308. https://doi.org/10.1007/978-3-319-73025-7_45.

(7) Jang, S.-Y.; Lee, S.-M.; Baik, H.-K. Tantalum and Niobium as a Diffusion Barrier between Copper and Silicon. *J. Mater. Sci. Mater. Electron.* **1996**, *7* (4), 1736–1738. https://doi.org/10.1007/BF00188954.

(8) Zhang, M.; Yu, W.; Wang, W. H.; Wang, W. K. Initial Phase Formation in Nb/Si Multilayers Deposited at Different Temperatures. *J. Appl. Phys.* **1996**, *80* (3), 1422–1427. https://doi.org/10.1063/1.362940.

(9) Bochníček, Z.; Vávra, I. Interdiffusion in Amorphous Nb/Si Multilayers. *Mater. Lett.* **2000**, *45* (2), 120–124. https://doi.org/10.1016/S0167-577X(00)00089-6.

(10) Suresh, N.; Phase, D. M.; Gupta, A.; Chaudhari, S. M. Electron Density Fluctuations at Interfaces in Nb/Si Bilayer, Trilayer, and Multilayer Films: An x-Ray Reflectivity Study. *J. Appl. Phys.* **2000**, *87* (11), 7946–7958. https://doi.org/10.1063/1.373479.

(11) Bochnícek, Z.; Vávra, I. Thermal Stability of Partially Crystalline Nb/Si Multilayers. *J. Phys. D. Appl. Phys.* **2001**, *34* (10A), A214–A218. https://doi.org/10.1088/0022-3727/34/10A/344.

(12) Okolo, B.; Lamparter, P.; Welzel, U.; Mittemeijer, E. J. Stress, Texture, and Microstructure in Niobium Thin Films Sputter Deposited onto Amorphous Substrates. *J. Appl. Phys.* **2004**, *95* (2), 466–476. https://doi.org/10.1063/1.1631733.

(13) Brongersma, H.; Draxler, M.; Deridder, M.; Bauer, P. Surface Composition Analysis by Low-Energy Ion Scattering. *Surf. Sci. Rep.* **2007**, *62* (3), 63–109. https://doi.org/10.1016/j.surfrep.2006.12.002.

(14) ter Veen, H. R. J.; Kim, T.; Wachs, I. E.; Brongersma, H. H. Applications of High Sensitivity-Low Energy Ion Scattering (HS-LEIS) in Heterogeneous Catalysis. *Catal. Today* **2009**, *140* (3–4), 197–201. https://doi.org/10.1016/j.cattod.2008.10.012.

(15) Keim, E. G.; Bijker, M. D.; Lodder, J. C. Preparation of Cross-Sectional Transmission Electron Microscopy Specimens of Obliquely Deposited Magnetic Thin Films on a Flexible Tape. *J. Vac. Sci. Technol. A Vacuum, Surfaces, Film.* **2002**, *19* (4), 1191–1194. https://doi.org/10.1116/1.1330259.

(16) Lisowski, W.; Keim, E. G.; Smithers, M. TEM and SEM Studies of Microstructural Transformations of Thin Iron Films during Annealing. *Appl. Surf. Sci.* **2002**, *189* (1–2), 148–156. https://doi.org/10.1016/S0169-4332(02)00016-8.

(17) Zameshin, A.; Makhotkin, I. A.; Yakunin, S. N.; van de Kruijs, R. W. E.; Yakshin, A. E.; Bijkerk, F. Reconstruction of Interfaces of Periodic Multilayers from X-Ray Reflectivity Using a Free-Form Approach. *J. Appl. Crystallogr.* **2016**, *49* (4), 1300–1307. https://doi.org/10.1107/S160057671601044X.

(18) Kessels, M. J. H.; Bijkerk, F.; Tichelaar, F. D.; Verhoeven, J. Determination of In-Depth Density Profiles of Multilayer Structures. *J. Appl. Phys.* **2005**, *97* (9), 093513. https://doi.org/10.1063/1.1882773.

(19) Sakhonenkov, S. S.; Filatova, E. O.; Gaisin, A. U.; Kasatikov, S. A.; Konashuk, A. S.; Pleshkov, R. S.; Chkhalo, N. I. Angle Resolved Photoelectron Spectroscopy as Applied to X-Ray Mirrors: An in Depth Study of Mo/Si Multilayer Systems. *Phys. Chem. Chem. Phys.* **2019**, *21* (45), 25002–25010. https://doi.org/10.1039/C9CP04582A.

(20) Sakhonenkov, S. S.; Filatova, E. O. Interface Formation between Be and W Layers Depending on Its Thickness and Ordering. *Appl. Surf. Sci.* **2020**, *534* (July), 147636. https://doi.org/10.1016/j.apsusc.2020.147636.

(21) Coloma Ribera, R.; van de Kruijs, R. W. E.; Sturm, J. M.; Yakshin, A. E.; Bijkerk, F. In Vacuo Growth Studies of Ru Thin Films on Si, SiN, and SiO 2 by High-Sensitivity Low Energy Ion Scattering. *J. Appl. Phys.* **2016**, *120* (6), 065303. https://doi.org/10.1063/1.4960577.

(22) Chandrasekaran, A.; van de Kruijs, R. W. E.; Sturm, J. M.; Zameshin, A. A.; Bijkerk, F. Nanoscale Transition Metal Thin Films: Growth Characteristics and Scaling Law for Interlayer Formation. *ACS Appl. Mater. Interfaces* **2019**, *11* (49), 46311–46326. https://doi.org/10.1021/acsami.9b14414.

(23) Zameshin, A. Probing Atmoic Scale Interface Processes Using X-Rays and Ions, University of Twente: Enschede, The Netherlands, 2018. https://doi.org/10.3990/1.9789036546508.

(24) Brüner, P.; Grehl, T.; Brongersma, H.; Detlefs, B.; Nolot, E.; Grampeix, H.; Steinbauer, E.; Bauer, P. Thin Film Analysis by Low-Energy Ion Scattering by Use of TRBS Simulations. *J. Vac. Sci. Technol. A Vacuum, Surfaces, Film.* **2015**, *33* (1), 01A122. https://doi.org/10.1116/1.4901451.

(25) Ion Channeling. In *Fundamentals of Nanoscale Film Analysis*; Springer US: Boston, MA; pp 84–104. https://doi.org/10.1007/978-0-387-29261-8_5.

(26) Shutthanandan, V.; Zhu, Z.; Stutzman, M. L.; Hannon, F. E.; Hernandez-Garcia, C.; Nandasiri, M. I.; Kuchibhatla, S. V. N. T.; Thevuthasan, S.; Hess, W. P. Surface Science Analysis of GaAs Photocathodes Following Sustained Electron Beam Delivery. *Phys. Rev. Spec. Top. - Accel. Beams* **2012**, *15* (6), 063501. https://doi.org/10.1103/PhysRevSTAB.15.063501.

(27) Bajt, S.; Stearns, D. G.; Kearney, P. A. Investigation of the Amorphous-to-Crystalline Transition in Mo/Si Multilayers. *J. Appl. Phys.* **2001**, *90* (2), 1017–1025. https://doi.org/10.1063/1.1381559.

(28) L. Vitos; A. V. Ruban; H. L. Skriver; J. Kollár. The Surface Energy of Metals. *Surf. Sci.* **1998**, *411* (1–2), 186–202. https://doi.org/10.1016/S0039-6028(98)00363-X.

(29) Eberl, C.; Liese, T.; Schlenkrich, F.; Döring, F.; Hofsäss, H.; Krebs, H. U. Enhanced Resputtering and Asymmetric Interface Mixing in W/Si Multilayers. *Appl. Phys. A Mater. Sci. Process.* **2013**, *111* (2), 431–437. https://doi.org/10.1007/s00339-013-7587-5.

(30) Gupta, A.; Kumar, D.; Phatak, V. Asymmetric Diffusion at the Interfaces in Fe/Si Multilayers. *Phys. Rev. B - Condens. Matter Mater. Phys.* **2010**, *81* (15), 1–5. https://doi.org/10.1103/PhysRevB.81.155402.

(31) Li, H.; Zhu, J.; Wang, Z.; Song, Z.; Chen, H. Asymmetrical Diffusion at Interfaces of Mg/SiC Multilayers. *Opt. Mater. Express* **2013**, *3* (5), 546. https://doi.org/10.1364/ome.3.000546.

(32) de Boer, F. R.; Boom, R.; Mattens, W. C. M.; Miedema, A. R.; Niessen, A. K. *Cohesion in Metals: Transition Metal Alloys*; 1988.

(33) McKeown, J. T.; Radmilovic, V. R.; Gronsky, R.; Glaeser, A. M. Silicide Characterization at Alumina-Niobium Interfaces. *J. Mater. Sci.* **2011**, *46* (11), 3969–3981. https://doi.org/10.1007/s10853-011-5324-z.

(34) Cahn, R. W. Binary Alloy Phase Diagrams-Second Edition. T. B. Massalski, Editor-in-Chief; H. Okamoto, P. R. Subramanian, L. Kacprzak, Editors. ASM International, Materials Park, Ohio, USA. December 1990. Xxii, 3589 Pp., 3 Vol., Hard- Back. $995.00 the Set. *Adv. Mater.* **1991**, *3* (12), 628–629. https://doi.org/10.1002/adma.19910031215.

(35) Bruijn, S.; Van De Kruijs, R. W. E.; Yakshin, A. E.; Bijkerk, F. In-Situ Study of the Diffusion-Reaction Mechanism in Mo/Si Multilayered Films. *Appl. Surf. Sci.* **2011**, *257* (7), 2707–2711. https://doi.org/10.1016/j.apsusc.2010.10.049.

(36) Huang, Q.; Zhang, J.; Qi, R.; Yang, Y.; Wang, F.; Zhu, J.; Zhang, Z.; Wang, Z. Structure and Stress Studies of Low Temperature Annealed W/Si Multilayers for the X-Ray Telescope. *Opt. Express* **2016**, *24* (14), 15620. https://doi.org/10.1364/OE.24.015620.

CHAPTER 5

Solid state reactions in Zr-Si layered systems during low temperature annealing

We present the interdiffusion phenomena observed during layer growth and low temperature annealing of Zr-Si layered structures. *In vacuo* high-sensitivity low-energy ion scattering (HS-LEIS) is used to study the change in surface atomic composition during the growth of Zr-on-Si and Si-on-Zr bilayer systems. The chemical interaction between Zr and Si atoms during growth is studied by measuring the binding energy shift using *in vacuo* X-ray Photoelectron Spectroscopy (XPS). High-resolution cross-sectional transmission electron microscopy (XTEM) imaging is performed on Zr/Si multilayer structures to characterize the effect of low-temperature (200 °C) annealing on interdiffusion between Zr and Si layers. The LEIS growth profile data of Zr-on-Si and Si-on-Zr systems show a fairly symmetrical interface with an effective width of ~ 0.8 – 0.9 nm. These values are similar to the ~ 1 nm amorphous Zr-on-Si and Si-on-Zr interfaces observed in the XTEM images of as-deposited Zr/Si multilayer structures. The XPS binding energy shift data suggests that the chemical interaction between Zr and Si atoms exists up to 0.9 nm as-deposited Zr thickness during Zr-on-Si growth, which indicates the Zr-Si intermixed region. However, in the case of Si-on-Zr growth, the chemical interaction is limited to 0.3 – 0.6 nm as-deposited thickness of Si, above which the growth of a pure Si layer begins. The asymmetry in chemical interaction during Zr-on-Si and Si-on-Zr growth is described based on the floating segregation behavior of Zr and Si atoms induced by the large atomic size difference. The XTEM images of Zr/Si multilayer samples annealed at 200 °C for 8h, shows complete solid state amorphization of Zr layers resulting in the formation of a thick ZrSi interlayer. The strong interdiffusion during low temperature annealing is tentatively explained to be driven by the strain energy at the interfaces because of the large atomic size difference between Zr and Si atoms.

5.1. INTRODUCTION

Interdiffusion and solid state reactions in nanoscale transition-metal/silicon (TM/Si) layered systems have attracted strong interests for decades.[1,2] This is primarily because of their importance in semiconductor devices. On the one hand, interdiffusion in TM/Si layers may lead to degradation of device functionality;[3] on the other hand, it may provide the possibility of producing stable transition-metal silicide layers through thermally-activated solid state reactions in TM/Si multilayers.[2,4] Activation of interdiffusion and solid state reactions at low thermal energy is essential in achieving the desired transition-metal silicide layer. Therefore, it is important to understand the fundamental layer material and structural properties that govern the interdiffusion of atoms during layer growth and during low temperature annealing.

The Zr/Si layered system has a wide range of applications in optics and semiconductor devices, where some applications demand a sharp interface between Zr and Si layers and others require a well-controlled low-temperature activation of a solid state reaction between Zr and Si layers. For instance, a Zr/Si multilayer is an excellent system for making a transmission filter for a soft X-ray telescope to suppress UV, visible and IR radiation.[5] In this case, limiting the interdiffusion between Zr and Si layers is necessary to achieve layer stability and maintain the excellent optical properties. Zr/Si multilayers are also an effective solution to produce zirconium silicide thin films via a solid state reaction.[4,6] The importance of zirconium silicide thin films in integrated circuits as a low-resistance contact[7] and their potential applications as high strength nanoscale membranes[8] have generated considerable interest in the solid state reaction of Zr/Si multilayers.

In this article, we report a detailed study on the layer growth and interface characteristics of Si-on-Zr and Zr-on-Si bilayer systems, and the interdiffusion in Zr/Si multilayers during low temperature annealing. The intermixing and segregation phenomena during near-room-temperature layer growth are studied using in-vacuo high-sensitivity low-energy ion scattering (HS-LEIS). The chemical interaction between Zr and Si atoms at the interfaces is studied using in-vacuo X-ray Photoelectron Spectroscopy (XPS). The structural characteristics of as-deposited and annealed Zr/Si multilayers are characterized using high-resolution transmission electron microscopy (HR-TEM).

5.2. EXPERIMENT AND METHODOLOGY

All Zr-Si bilayer and multilayer samples were deposited using a direct-current magnetron sputtering technique on single side polished Si(100) wafers with ~1 nm native oxide and an rms surface roughness of 0.15 ± 0.05 nm. The Si-on-Zr and Zr-on-Si bilayer samples for layer growth studies were deposited in a sputter deposition system with *in vacuo* transfer to a high-sensitivity low energy ion scattering (HS-LEIS) setup and an X-ray Photoelectron Spectroscopy (XPS) setup, which were mounted in two separate UHV chambers, connected to the deposition chamber. The base pressure of

the deposition chamber was < $5x10^{-9}$ mbar. Krypton was used as the sputter gas at a working pressure of $1x10^{-3}$ mbar. The substrate-to-target distance for Zr and Si depositions was 8 cm. Both magnetrons were equipped with a shutter in front to prevent cross-contamination during deposition. The deposited thicknesses were monitored using a quartz crystal microbalance present in close proximity to each magnetron. The deposition rates of Zr and Si were calibrated using ex-situ grazing incidence X-ray reflectivity (GI-XRR) measurements on Zr and Si layers each with three different thicknesses, respectively, for better accuracy. The Zr/Si multilayer samples, starting with a Si layer and terminating with a 4 nm Si cap layer to prevent oxidation of the multilayer stack, were deposited in a Roth & Rau MS1600 deposition system. The deposition conditions used for multilayer samples, such as substrate-to-target distance, sputter voltage, and sputter gas and pressure, were similar to that of the bilayer samples. Hence, the particle energies and layer microstructure can be expected to be similar in both deposition systems.

The multilayer samples were annealed at 200 °C for 8 h in a high-vacuum environment to limit the oxidation of the layers. A Philips CM300ST-FEG Transmission Electron Microscope (300 kV acceleration voltage) was used for obtaining high resolution cross-sectional transmission electron microscope (XTEM) images. The specimens for XTEM were prepared by creating a symmetrical cross-sectional sandwich structure using dimple grinding/polishing and argon ion thinning methods.[9,10] The energy of the Ar^+ was reduced from 4.5 keV to 0.5 keV during the final stages of thinning procedure in order to minimize specimen damage.

In vacuo high-sensitivity low energy ion scattering (HS-LEIS) was used to study the intermixing and surface segregation phenomena that occur during layer growth. HS-LEIS measurements were performed using an IONTOF Qtac[100] tool with $1x10^{-10}$ mbar base pressure. A 3keV He^+ ion beam with 3 nA ion current at normal incidence angle was used for LEIS measurements. Detailed information on the HS-LEIS technique can be found in the references[11,12]. A bilayer architecture as shown in Figure 5.1a was used for the LEIS layer growth studies. The high surface sensitivity of HS-LEIS coupled with the *in vacuo* sample transfer between deposition and LEIS chambers enables the measurement of the evolution of surface coverage as a function of the deposited film layer thickness, which we refer to as LEIS growth profile.[13,14] The following procedure was used to obtain the LEIS growth profile for Zr-on-Si and Si-on-Zr systems:[13,15]

(1) A 4 nm substrate layer (Zr or Si) was deposited on a Si wafer, followed by deposition of a 0.3 nm film layer (Si or Zr, correspondingly).
(2) The sample was transferred *in vacuo* to the LEIS chamber and a LEIS spectrum was recorded.
(3) A 4 nm substrate layer was deposited on a new Si wafer, followed by deposition of the film layer, with a sub-nanometer increase in thickness.

(4) Steps 2 and 3 were repeated until the film layer LEIS signal saturates, which corresponds to a 100% film coverage.

The integral area of the LEIS surface peak of an element, after background subtraction, provides a quantitative measurement of the number of surface atoms of that element. The surface coverage of an element is then given by the ratio of the integral area of the surface peak in the investigated sample to that of the reference sample. It is not possible to distinguish between intermixing and island growth using LEIS measurements. Therefore, *ex-situ* AFM measurements were done using a BRUKER Dimension Edge atomic force microscope (AFM) with a high-resolution tip (Mikro-Masch HiRes-C15/Cr-Au) to characterize the surface morphology and roughness of the deposited samples.

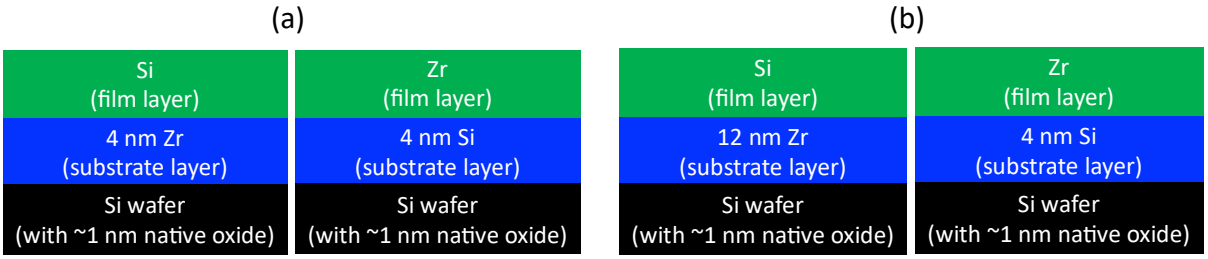

Figure 5.1. Bilayer architecture used for: (a) LEIS layer growth studies, (b) XPS layer growth studies (thicknesses not to scale).

The LEIS surface coverage evolution provides key information about the film layer closing thickness, surface atomic densities, and surface segregation during growth. Furthermore, the in-depth concentration profile and interface width can also be extracted from the LEIS growth profile by assuming a suitable mathematical model for the interface profile. It has been recently reported that the deposition-induced interface concentration profile between film and substrate layers can be represented by a logistic function (LGF).[13,15,16] Based on the LGF-like interface model, the expression for the evolution of film atom surface coverage θ, as a function of the as-deposited film layer thickness h and the effective interface width σ, can be derived as:

$$\theta = 1 - e^{-\left(\frac{h}{0.59\,\sigma}\right)}. \quad (1)$$

Eq. (1) describes cases where the evolution of the film atom coverage as a function of the as-deposited film thickness is defined purely by intermixing between film and substrate atoms during growth. For cases where surface segregation of substrate or film atoms is present during growth in addition to the intermixing process, the film atom surface coverage is given by Zameshin's segregation model[13,16]:

$$\theta(h, \alpha, \lambda) = \left(1 - e^{\left(\frac{-h}{0.59\,\sigma}\right)}\right) - \left(\frac{\alpha}{0.59\,\sigma\,\lambda - 2}\left(e^{-\frac{2h}{0.59\,\sigma}} - e^{-\lambda h}\right)\right), \quad (2)$$

where the dimensionless parameter α represents the strength of floating segregation of substrate atoms, and the parameter λ, with an inverse length unit, denotes the effectiveness of removal of the segregated

atoms. Note that the segregation model simplifies to Eq. (1) in the absence of segregation ($\alpha = 0$). The effective interface width (σ) of Si-on-Zr and Zr-on-Si systems can be obtained by fitting their respective LEIS growth profiles using Eq. (1) or Eq. (2) depending on the presence or absence of segregation. The value of σ obtained from the LEIS growth profile is analogous to the interface width values commonly obtained from an X-ray reflectometry spectrum assuming an error function-like interface model.

In vacuo X-ray photoelectron spectroscopy (XPS) was used to study the chemical interaction between Zr and Si at the interface during the growth of Si-on-Zr and Zr-on-Si. The XPS measurements were done using a Thermo Theta Probe Spectrometer using a monochromatic Al-Kα source. The bilayer architectures shown in Figure 5.1b were used for the XPS layer growth studies. Because the XPS depth resolution is ~ 10 nm, a 12 nm Zr substrate layer was used for Si-on-Zr system to avoid any XPS signal from the underlying Si wafer. The procedure for recording the XPS spectra was similar to that of the LEIS growth studies: 0.3 nm increments in as-deposited film layer thicknesses and freshly prepared samples for each growth step.

5.3. RESULTS AND DISCUSSION

5.3.1. Layer Growth Studies: Zr-on-Si and Si-on-Zr Bilayer Systems

The LEIS spectra of the Zr-on-Si system are shown in Figure 5.2a for various as-deposited Zr thicknesses. The He^+ primary ions that backscatter from the surface layer contribute to the surface peak and those scattering from the bulk layers contribute to the low energy tail. The increase in Zr surface peak signal and decrease in Si surface peak signal for increasing as-deposited Zr thickness can be observed for Zr-on-Si growth. AFM images (not shown here) suggest a 2D growth with rms roughness in the range of ~ 0.2 ± 0.05 nm, which is similar to the Si substrate rms roughness. Therefore, the change in Zr and Si surface peak intensities with increasing Zr layer thickness is solely because of intermixing between Zr and Si atoms during layer growth, and it does not have a contribution from 3D island growth.

Figure 5.2b shows the surface coverage evolution of Zr atoms as a function of as-deposited Zr thickness for Zr-on-Si growth, and the LGF-like interface model fit according to Eq. (1). It is obvious that the fit based on an LGF-like interface model cannot describe the Zr-on-Si growth profile. The growth profile can however be explained by floating segregation of Si substrate atoms in addition to the intermixing process as described by Zameshin's segregation model according to Eq. (2) with intermixing and segregation terms. The effect of segregation in addition to the intermixing process has been previously reported for TM-on-Si systems[16,17], and also for TM-on-TM systems[13]. The floating segregating atoms are considered to be removed via grain boundaries or defect sites, and are expected to have no effect on the effective interface width.[13] The LEIS growth profile fit based on the

segregation model (Eq. (2)), as shown in Figure 5.2c, fully describes the surface coverage evolution of Zr film atoms in Zr-on-Si growth. The corresponding contributions from the segregating Si substrate atoms and Zr film atoms in the absence of segregation are also shown in the figure. The as-deposited Zr thickness required to obtained 99% Zr coverage ("intermixing thickness") is 2.7 nm ± 0.1 nm, and the effective interface width is 0.94 ± 0.14 nm. The effective interface width, which is analogous to the interface width obtained from XRR fit or XTEM, is a commonly used term to define the interfaces in multilayer structures. The intermixing thickness is important for applications where a complete coverage of substrate layer by the film layer is required.

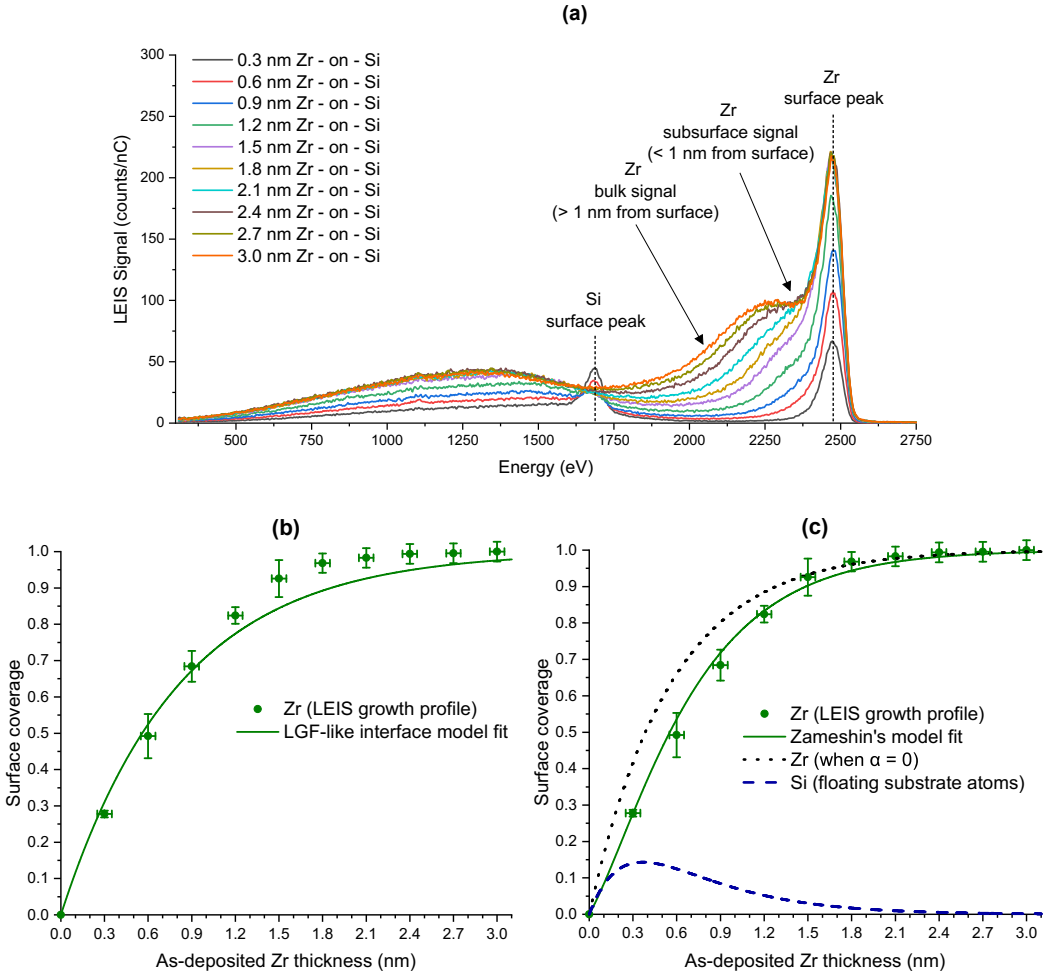

Figure 5.2. (a) LEIS spectra of Zr-on-Si growth for various as-deposited Zr thickness, LEIS growth profile of Zr-on-Si with (b) LGF-like interface model fit and (c) Zameshin's segregation model fit

The He+ LEIS spectra of the Si-on-Zr systems are shown in Figure 5.3a for various as-deposited Si thicknesses. AFM images (not shown here) suggest a 2D growth with rms roughness in the range of ~ 0.2 ± 0.05 nm, which is similar to the Si substrate rms roughness. This suggests that the change in LEIS surface peak intensity is caused by intermixing and not because of 3D island growth. Figure 5.3b shows the LEIS growth profile of Si-on-Zr the surface coverage evolution of Si atoms as a function of as-deposited Si thickness for growth, and the LGF-like interface model fit according to

Eq. (1). Note that a similar fit is obtained when Zameshin's segregation model according to Eq. (2) is used, as shown in Figure 5.3c. The effective interface width σ obtained from the LGF-like interface model fit is 0.83 ± 0.10 nm and the intermixing thickness for Si-on-Zr is 2.3 nm ± 0.1 nm. Thus, within the error, the effective interface width values of Zr-on-Si and Si-on-Zr seem to be comparable, indicating symmetrical interfaces.

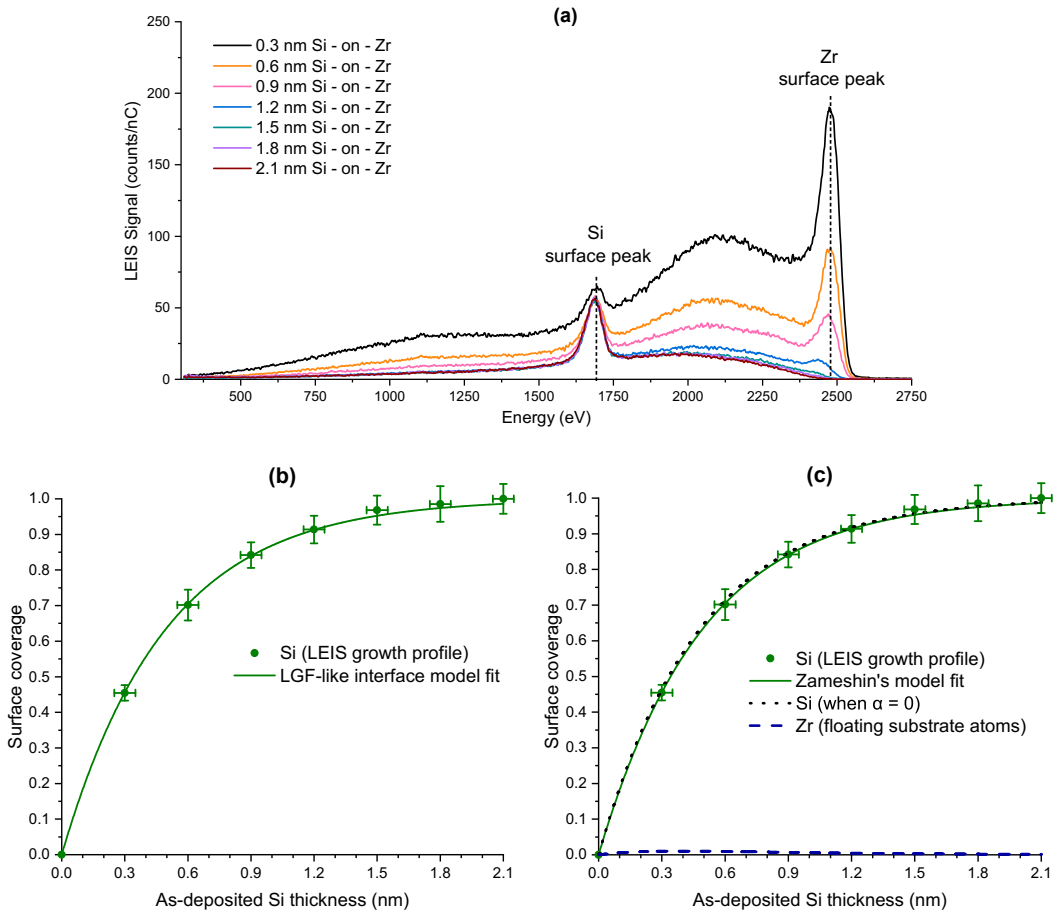

Figure 5.3. (a) LEIS spectra of Si-on-Zr growth for various as-deposited Si thickness, LEIS growth profile of Si-on-Zr with (b) LGF-like interface model fit, (c) Zameshin's segregation model fit

The transition metal – silicon (TM-Si) interfaces are generally known to be asymmetric in interface thickness, where the Si-on-TM interface is sharper than the TM-on-Si interface.[14,15,17] This can be explained by the surface energy difference between the TM and Si atoms, where it is energetically favorable for the low surface energy Si atoms to stay at the surface during growth. As a result, the intermixing probability for TM-on-Si growth is greater than Si-on-TM growth, which results in asymmetric interfaces. This effect has also been shown to be true for TM-on-TM systems.[13] However, in the case of the Zr-Si system, in spite of having a large surface energy difference (Si: 0.92 eV/atom, Zr: 1.63 eV/atoms),[13,18] the effective interface width values for Zr-on-Si and Si-on-Zr interfaces obtained from the LEIS growth profile are surprisingly similar. Some authors explain the asymmetry in the TM-Si interface width by the crystallinity of the TM layer, where Si diffuses faster into amorphous TM in the initial stages of TM-on-Si growth than Si growing on a crystalline TM layer

during Si-on-TM growth.[19] Although the crystallinity may explain the asymmetry in some TM-on-Si systems, in this work we will show XTEM images of Zr/Si multilayers, where the 4 nm Zr layers are clearly polycrystalline. Therefore, crystallinity of the Zr layer cannot explain the observed symmetrical interfaces. Besides crystallinity, a highly porous growth of Zr layer can potentially lead to stronger interdiffusion at Si-on-Zr interface during Si growth. However, layers produced by magnetron sputtering, under the deposition conditions described in the experimental section, generally yield dense films, which would rule out porosity of the Zr layer as a possible reason for symmetrical interfaces. Furthermore, the bond energy[20] and crystal structure of Zr is similar to that of Ru and yet the Si-on-Zr interface width is ~1.5 times larger than the interface width of the Si-on-Ru system obtained from the LEIS growth profile fit by Coloma Ribera et al[14]. Therefore, none of the arguments based on surface energy difference, layer crystallinity and porosity, and bond energy can describe the symmetry in Zr-Si interfaces.

In order to understand the reason behind the observed interface symmetry in Zr/Si system, the process of segregation during growth should be considered. It has been recently shown that TM atoms with a large atomic size tend to segregate during TM-on-TM growth and the effect is significant especially when the substrate atom is larger than the film atom.[13] However, based on the LEIS growth profile fits of Zr-on-Si and Si-on-Zr systems, segregation of Si is observed during Zr-on-Si growth and no segregation is observed during Si-on-Zr growth. This is contrary to the results obtained in TM-on-TM work, which suggest a strong segregation of Zr substrate atoms during Si-on-Zr growth because of its large size. This is however not obvious from the LEIS growth profile of Si-on-Zr, where a simple LGF-like interface model, without the segregation component, seems to explain the growth profile data well. Our hypothesis is that the large Zr substrate atoms segregate strongly during Si-on-Zr growth, however, the effect of Zr surface segregation is not captured distinctly in the Si-on-Zr LEIS growth profile because of an interplay between simultaneous segregation of Si and Zr atoms. The segregation of Zr atoms is counterbalanced by Si segregation, which results in segregated Zr atoms getting trapped in the growing Si matrix until all the floating segregating Zr atoms are eventually removed from the surface. Note that Zameshin's segregation model does not consider simultaneous segregation of both film and substrate atoms, and therefore, it is not possible to separate the intermixing and floating segregation contributions. Nevertheless, based on our hypothesis, the Si-on-Zr interface is expected to have two contributions: (i) Zr-Si intermixing caused by surface-energy difference and deposition process during the early stages of Si-on-Zr growth as described in reference[13], followed by (ii) Zr-Si intermixed region caused by floating Zr atoms trapped in the Si matrix as a result of simultaneous segregation of Zr and Si atoms. Region (i) is expected to be an intermixed region with similar Zr and Si nearest neighbor atoms, whereas region (ii) is expected to be a predominantly Si matrix with trapped floating Zr atoms.

In order to understand the nature of nearest neighbor atoms and chemical interaction at Zr-Si interfaces, *in vacuo* X-ray photoelectron spectroscopy (XPS) was used for measuring the binding energy shift of Zr and Si XPS peaks as a function of increasing film layer thickness. During the early stages of growth, the substrate element photoelectron peak will be mostly dominated by the intense signal from the bulk of the substrate layer and hence, peak shift because of chemical interaction at the surface level will be insignificant. For this reason, the film element photoelectron peak was to studied during growth, (i.e.) the Si 2p peak was analyzed for Si-on-Zr growth and the Zr 3d peak was analyzed for Zr-on-Si growth. This allows us to measure a shift in binding energy caused by chemical interaction, in the absence of surface oxidation.

Figure 5.4a shows the Zr 3d photoelectron spectra of Zr-on-Si system for increasing as-deposited Zr thickness. No ZrO_2 peak can be seen around 182.8 eV in all the investigated samples, indicating that the Zr film layer is not oxidized during *in vacuo* sample transfer. The Zr 3d photoelectron spectra consists of the Zr $3d_{3/2}$ and Zr $3d_{5/2}$ doublet peaks. The positions of the peak binding energy of both the Zr 3d peaks shift towards lower binding energy with increasing as-deposited Zr thickness. The Zr $3d_{5/2}$ peak binding energy decreases from 179.1 eV to 178.7 eV, indicating a strong Zr-Si chemical interaction in the initial stages of Zr-on-Si growth,[21] followed by the growth of elemental Zr (178.7 eV). The Zr $3d_{5/2}$ and Zr $3d_{3/2}$ photoelectron peaks were fitted using two components for each: elemental Zr and Zr-Si. It is important to note that, in the case of intermixing during growth, the stoichiometry of Zr-Si varies with increasing as-deposited Zr thickness. Therefore, the term "Zr-Si" in this work represents the nearest neighbor effect and not the stoichiometric Zr-silicide formation generally observed after annealing at high temperatures. Nevertheless, for the sake of simplicity, a fixed binding energy value is used for the Zr-Si $3d_{5/2}$ component for peak fitting. The peak binding energy values used for Zr $3d_{5/2}$ and Zr-Si $3d_{5/2}$ were 178.7 ± 0.1 eV and 179.1± 0.1 eV, and the peak binding energy values used for Zr $3d_{3/2}$ and Zr-Si $3d_{3/2}$ were 181.0 ± 0.1 eV and 181.4 ± 0.1 eV.[21]

Figure 5.4b shows the area of Zr $3d_{5/2}$ and Zr-Si $3d_{5/2}$ peaks obtained from the fit, plotted as a function of as-deposited Zr thickness during Zr-on-Si growth. The Zr-Si peak increases up to an as-deposited Zr thickness of ~0.9 nm, whereas the Zr peak area increases strongly after ~ 0.9 nm as-deposited Zr thickness. This indicates the intermixing between Zr and Si atoms up to 0.9 nm as-deposited thickness and the growth of a predominantly Zr layer after that. The reduction in Zr-Si peak area can be explained by the reduced signal from the Zr-Si intermixed region buried under the growing Zr layer. The Zr-Si chemical interaction up to ~0.9 nm of as-deposited Zr thickness observed in XPS growth profile is in accordance to the 0.94 ± 0.14 nm effective interface width of Zr-on-Si calculated from the LEIS growth profile.

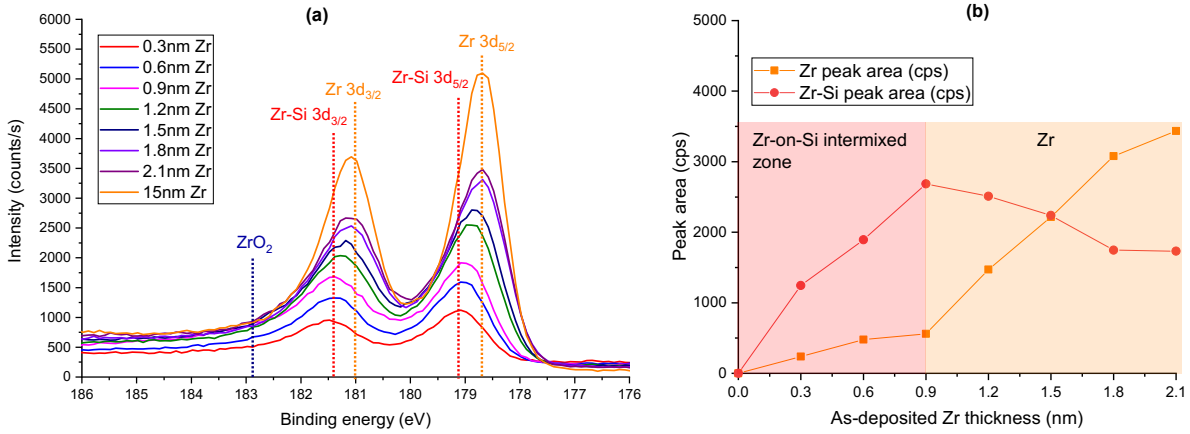

Figure 5.4. (a) XPS spectra of Zr-on-Si growth for various as-deposited Zr thickness, (b) Zr and Zr-Si integral peak area as a function of as-deposited Zr thickness

Figure 5.5 shows the Si 2p photoelectron spectra of Si-on-Zr for increasing as-deposited Si thickness. The Si 2p photoelectron peak binding energy increases from ~ 98.5 eV to 99.1 eV with increasing Si thickness. The lower peak binding energy in the initial stages of growth, when compared to the reference binding energy for elemental Si 2p of ~ 99.1 eV, indicates a chemical interaction between Si and Zr.[21] In order to quantify the contributions from the elemental and Zr-Si Si atoms, the Si 2p photoelectron peak was fitted with four Si 2p components: elemental Si $2p_{3/2}$, elemental Si $2p_{1/2}$, Zr-Si Si $2p_{3/2}$ and Zr-Si Si $2p_{1/2}$. The peak binding energy values of elemental Si 2p3/2 and silicide Si $2p_{3/2}$ were 99.0 ± 0.1 eV and 98.4 ± 0.1 eV respectively, and the peak binding energy values of the Si $2p_{1/2}$ components were set to + 0.63 ± 0.1 eV from their corresponding Si $2p_{3/2}$ peaks.[21]

Figure 5.5 shows the area of Si $2p_{3/2}$ and Zr-Si $2p_{3/2}$ peaks obtained from the fit, plotted as a function of as-deposited Si thicknesses. After 0.3 nm as-deposited Si thickness, the Zr-Si $2p_{3/2}$ peak area decreases, whereas the elemental Si $2p_{3/2}$ peak increases strongly. The absence of chemical interaction between Zr and Si atoms above ~ 0.3 nm as-deposited Si thickness indicates that the intermixing between Zr and Si atoms is limited to ~ 0.3 nm, in comparison to Zr-on-Si, in which the intermixing is observed up to 0.9 nm. Above 0.3 nm as-deposited Si thickness, the growing film layer is predominantly Si-rich and the floating segregating Zr atoms trapped in the Si matrix have insignificant effect on the binding energy of Si. This strongly supports our hypothesis that the Si-on-Zr interface is driven by intermixing at early stages of Si growth, followed by simultaneous segregation of Zr and Si atoms resulting in segregating Zr atoms trapped in the Si matrix.

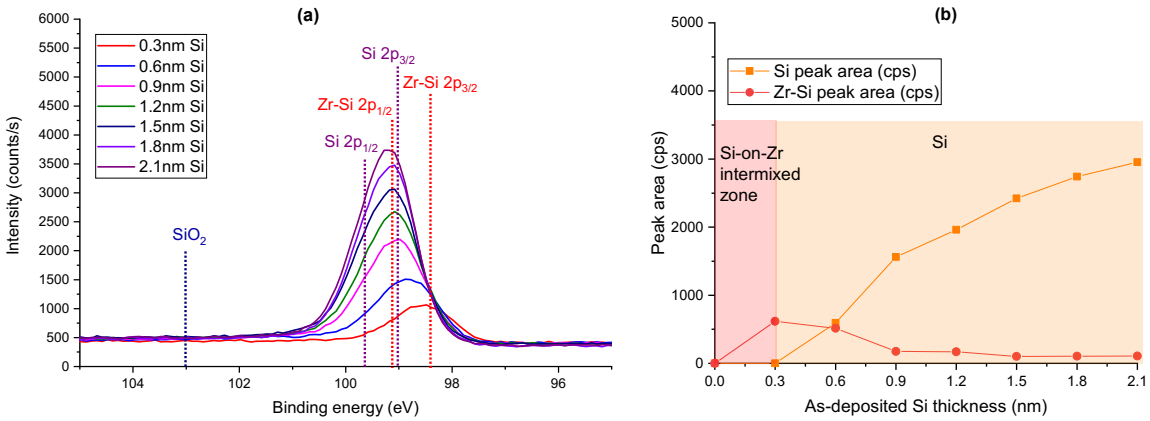

Figure 5.5. (a) XPS spectra of Si-on-Zr growth for various as-deposited Si thickness, (b) Si and Zr-Si integral peak area as a function of as-deposited Si thickness

5.3.2. Interface Diffusion Studies: As-deposited and Annealed Zr/Si Multilayer System

The interdiffusion in Zr/Si multilayers with as-deposited Zr and Si layer thickness of 4 nm each, after annealing at 200°C for 8h is investigated using XTEM imaging. The XTEM image of the as-deposited Zr/Si multilayer is shown in Figure 5.6a. The XTEM image shows ~3 nm thick polycrystalline Zr layers, ~2.2 nm thick amorphous Si layers, and distinct ~1 nm thick interface regions visible between the Zr and Si layers. It is important to note that the first Si layer (on top of the c-Si substrate) is ~3.5 nm thick because of the fact that it has only one interface with Zr when compared to the subsequent Si layers with two interfaces with the Zr layers. This results in less a-Si being consumed in intermixing between Si and Zr for the first Si layer. This effect was also observed in the TEM image of Ru/Si multilayers reported by Y. Cheng et al[22]. It is important to note that, although Zr-on-Si and Si-on-Zr interfaces are symmetrical in terms of the interface width (~1 nm each), the Zr-on-Si interface formation is driven by the surface energy difference and deposition process, whereas the Si-on-Zr interface is driven by intermixing at the early stages of growth, followed by floating Zr atoms trapped in the growing Si matrix.

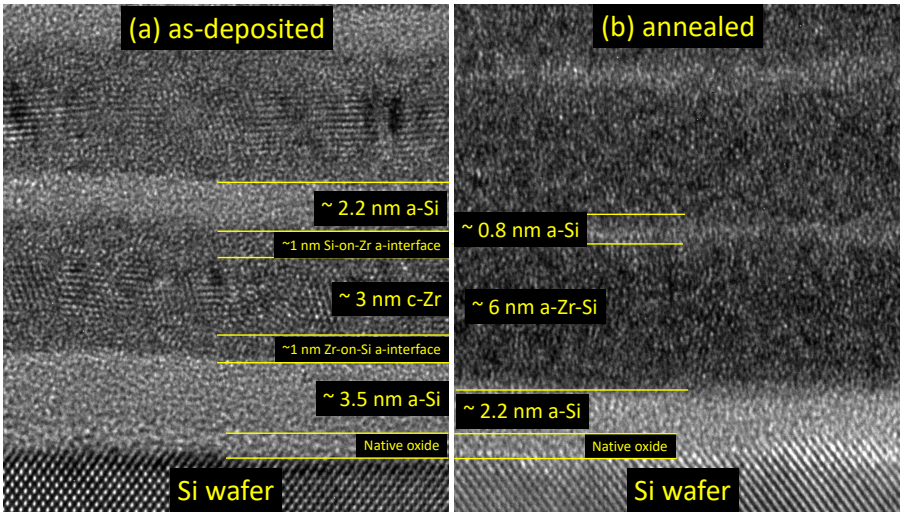

Figure 5.6. XTEM images of Zr/Si multilayer (a) as-deposited and (b) annealed at 200°C for 8h

The XTEM image of the annealed Zr/Si multilayer is shown in Figure 5.6b. The first Si layer thickness has been reduced by ~ 1.3 nm, which can be attributed to the diffusion mainly at the top interface (Zr-on-Si) because no interdiffusion is expected to occur at the bottom interface (Si – on – c-Si substrate). The thickness of the subsequent Si layers has reduced from ~ 2.2 nm to ~ 0.8 nm, indicating a strong thermally-activated interdiffusion. A complete solid state amorphization of the polycrystalline Zr layer is obvious from the figure, which results in the formation of a ~ 6 nm thick amorphous Zr-Si intermixed layer. Solid state amorphization of metal layers during annealing is a well-known phenomenon in TM/Si multilayer systems. In our previous study on Nb/Si multilayers[15], with 4 nm Nb and Si layers, no diffusion was observed at Nb-on-Si interface after annealing at 200 °C for 8 hours, while ~ 1 nm interdiffusion was observed at the Si-on-Nb interface, which was attributed to the thermally-activated grain boundary diffusion of Si atoms. The Nb layer remained polycrystalline even after annealing, although the layer thickness reduced from ~ 3.3 nm to ~ 2.4 nm. An increase in thickness of the amorphous interlayer due to interdiffusion during annealing has been reported for other TM/Si multilayers as well.[15,23] However, none of the reported TM/Si multilayers shows a complete amorphization of the 3-4 nm thick TM layer during low temperature annealing around 200 °C as seen in the case of Zr/Si multilayers. This effect cannot be explained by thermally-activated diffusion of atoms via grain boundary. Considering the large atomic size difference between Zr and Si atoms, the strain energy can be expected to be significant at the interfaces with a mixture of Zr and Si atoms, which can drive the bulk diffusion of atoms via interfaces, activated or enhanced by the thermal energy provided during annealing at 200 °C.

The atomic radii difference between Zr and Si atom is ~ 0.42 Å. This is significantly greater than other TM/Si systems (Mo/Si ~ 0.21 Å, Ru/Si ~ 0.16 Å, W/Si ~ 0.21Å, Nb/Si – 0.28 Å) commonly reported in the literature that do not show complete amorphization of the metal layers. In order to verify the strain-energy-activated bulk diffusion hypothesis, we investigated the Ce/Si system, selected because it has an even larger atomic radii difference (0.64 Å) than Zr/Si. A Ce/Si multilayer with 3 nm Ce and Si layers each was deposited under conditions similar to that of Zr/Si. Figure 5.7 shows the grazing incidence X-ray reflectometry (GI-XRR) spectra of a Ce/Si multilayer, measured on days 1 and 3 after deposition. A shift in the position of multilayer Bragg peaks toward higher incidence angle can be observed between the measurements taken on day 1 and day 3, which suggests a compaction in the multilayer, most likely driven by interdiffusion of atoms via the interfaces as a function of time near room-temperature. This data indicates that a large atomic size difference between two layer materials can drive the interdiffusion during low temperature annealing. Therefore, the complete solid state amorphization of the Zr layer in Zr/Si multilayer could have been driven by the strain energy at the interfaces as a result of the large atomic size difference between Zr and Si atoms.

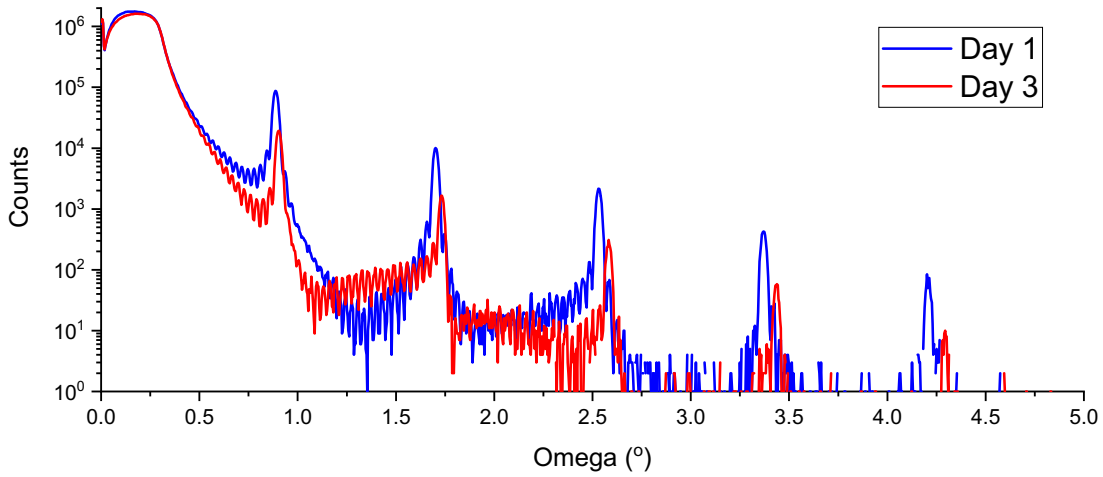

Figure 5.7. XRR spectrum of Ce/Si multilayer measured on Day 1 and Day 3

In conclusion, the large atomic size difference (> 0.42 Å) between the layer materials can lead to significant strain energy at the interface region, which can drive the interdiffusion of atoms during low temperature annealing. It is suggested here that the larger the size difference, the lower the thermal energy required to activate the diffusion process. The two material combinations investigated here do fit in such hypothesis. The phenomenon of spontaneous interdiffusion is highly beneficial for applications that require solid state reaction between layer materials at low temperatures in order to form an alloy or compound layer. However, for applications that require sharp interfaces, interdiffusion of atoms at low temperatures can result in poor functional properties of the layered structure.

5.4. SUMMARY AND CONCLUSIONS

Intermixing and nearest-neighbor chemical interaction during the growth of Zr-on-Si and Si-on-Zr systems were investigated using *in vacuo* HS-LEIS and XPS, respectively. The LEIS growth profiles of Zr-on-Si and Si-on-Zr systems seem to be identical, however, the XPS binding energy shift shows that the chemical interaction between Zr and Si atoms exists up to ~ 0.9 nm in the case of Zr-on-Si, whereas ~ 0.3 nm in the case of Si-on-Zr. This asymmetry in chemical interaction is explained in terms of intermixing and a floating segregation behavior of atoms during growth. XTEM imaging was performed on Zr/Si multilayers to study the effect of low temperature annealing on interdiffusion between Zr and Si layers.

The following conclusions are derived:

- The as-deposited effective interface width of Zr-on-Si system obtained from the LEIS growth profile fit is 0.94 ± 0.14 nm. Si exhibits floating segregation during Zr-on-Si growth. Based on the XPS binding energy shift, a chemical interaction can be expected between Zr and Si atoms up to 0.9 nm as-deposited Zr thickness during Zr-on-Si growth, which suggests a Zr-Si intermixed region. With further increase in Zr thickness, growth of pure Zr with limited or no Si neighboring atoms was observed. The XTEM image of as-deposited Zr/Si multilayer

shows a ~ 1 nm amorphous intermixed region at Zr-on-Si interface, which is similar to the values obtained from the LEIS and XPS data.

- The Si-on-Zr LEIS growth profile looks visually identical to the Zr-on-Si LEIS growth profile. For this system, a hypothesis was proposed to describe the Si-on-Zr growth that suggests two mechanisms contributing to the Si-on-Zr interface formation: (i) a surface-energy difference and deposition process induced intermixing of Zr and Si during early stages of Si-on-Zr growth, followed by (ii) a process of floating segregation of Zr atoms being trapped in the growing Si matrix, forming a Zr-Si intermixed region, because of simultaneous floating segregation of Zr and Si atoms during Si-on-Zr growth. The XTEM image shows a ~ 1 nm amorphous intermixed region at the Si-on-Zr interface, which is similar to the Zr-on-Si interface. However, XPS binding energy shift indicates that the chemical interaction between Zr and Si is limited to ~ 0.3 nm as-deposited Si thickness during Si-on-Zr growth, which validates the hypothesis.
- The XTEM images of Zr/Si multilayer after low temperature annealing at 200 °C show a complete solid state amorphization of the Zr layers and formation of a thick ZrSi layer. This phenomenon is explained by the strain-energy induced interdiffusion at the Zr-Si interfaces because of the large atomic size difference between Zr and Si atoms. In fact, Ce/Si multilayer system, having even larger atomic radii difference, used for verification of the process is shown to exhibit interdiffusion even near room temperature.

5.5. REFERENCES

(1) Roy, S.; Paul, A. Growth of Hafnium and Zirconium Silicides by Reactive Diffusion. *Mater. Chem. Phys.* **2014**, *143* (3), 1309–1314. https://doi.org/10.1016/j.matchemphys.2013.11.039.

(2) Chen, L. J. Solid State Amorphization in Metal/Si Systems. *Mater. Sci. Eng. R Reports* **2000**, *29* (5), 115–152. https://doi.org/10.1016/S0927-796X(00)00023-1.

(3) Wang, W. H.; Bai, H. Y.; Zhang, M.; Zhao, J. H.; Zhang, X. Y.; Wang, W. K. Interdiffusion in Nanometer-Scale Multilayers Investigated by in Situ Low-Angle x-Ray Diffraction. *Phys. Rev. B - Condens. Matter Mater. Phys.* **1999**, *59* (16), 10811–10822. https://doi.org/10.1103/PhysRevB.59.10811.

(4) Shim, J. Y.; Kwak, J. S.; Chi, E. J.; Baik, H. K.; Lee, S. M. Formation of Amorphous and Crystalline Phases, and Phase Transition by Solid-State Reaction in Zr Si Multilayer Thin Films. *Thin Solid Films* **1995**, *269* (1–2), 102–107. https://doi.org/10.1016/0040-6090(95)06744-2.

(5) Bibishkin, M. S.; Chkhalo, N. I.; Gusev, S. A.; Kluenkov, E. B.; Lopatin, A. Y.; Luchin, V. I.; Pestov, A. E.; Salashchenko, N. N.; Shmaenok, L. A.; Tsybin, N. N.; et al. Multilayer Zr/Si Filters for EUV Lithography and for Radiation Source Metrology; Valiev, K. A., Orlikovsky,

A. A., Eds.; 2008; Vol. 702502, pp 702502-702502–702510. https://doi.org/10.1117/12.802347.

(6) Chen, H. L.; Ju, S. P.; Wu, T. Y.; Hsieh, J. Y.; Liu, S. H. Investigation of Zr and Si Diffusion Behaviors during Reactive Diffusion-a Molecular Dynamics Study. *RSC Adv.* **2015**, *5* (33), 26316–26320. https://doi.org/10.1039/c4ra16962j.

(7) Yamauchi, T.; Zaima, S.; Mizuno, K.; Kitamura, H.; Koide, Y.; Yasuda, Y. Solid Phase Reaction and Electrical Properties in Zr/Si System. *Appl. Phys. Lett.* **1990**, *57* (11), 1105–1107. https://doi.org/10.1063/1.103505.

(8) van Zwol, P. J.; Nasalevich, M.; Kurganova, E.; Voorthuijzen, P.; Vles, D.; Péter, M.; Symens, W.; van der Zande, W.; Notenboom, A.; Klootwijk, J.; et al. Pellicle Films Supporting the Ramp to HVM with EUV. **2017**, No. October 2017, 22. https://doi.org/10.1117/12.2280560.

(9) Lisowski, W.; Keim, E. G.; Smithers, M. TEM and SEM Studies of Microstructural Transformations of Thin Iron Films during Annealing. *Appl. Surf. Sci.* **2002**, *189* (1–2), 148–156. https://doi.org/10.1016/S0169-4332(02)00016-8.

(10) Keim, E. G.; Bijker, M. D.; Lodder, J. C. Preparation of Cross-Sectional Transmission Electron Microscopy Specimens of Obliquely Deposited Magnetic Thin Films on a Flexible Tape. *J. Vac. Sci. Technol. A Vacuum, Surfaces, Film.* **2002**, *19* (4), 1191–1194. https://doi.org/10.1116/1.1330259.

(11) Brongersma, H.; Draxler, M.; Deridder, M.; Bauer, P. Surface Composition Analysis by Low-Energy Ion Scattering. *Surf. Sci. Rep.* **2007**, *62* (3), 63–109. https://doi.org/10.1016/j.surfrep.2006.12.002.

(12) ter Veen, H. R. J.; Kim, T.; Wachs, I. E.; Brongersma, H. H. Applications of High Sensitivity-Low Energy Ion Scattering (HS-LEIS) in Heterogeneous Catalysis. *Catal. Today* **2009**, *140* (3–4), 197–201. https://doi.org/10.1016/j.cattod.2008.10.012.

(13) Chandrasekaran, A.; van de Kruijs, R. W. E.; Sturm, J. M.; Zameshin, A. A.; Bijkerk, F. Nanoscale Transition Metal Thin Films: Growth Characteristics and Scaling Law for Interlayer Formation. *ACS Appl. Mater. Interfaces* **2019**, *11* (49), 46311–46326. https://doi.org/10.1021/acsami.9b14414.

(14) Coloma Ribera, R.; van de Kruijs, R. W. E.; Sturm, J. M.; Yakshin, A. E.; Bijkerk, F. In Vacuo Growth Studies of Ru Thin Films on Si, SiN, and SiO 2 by High-Sensitivity Low Energy Ion Scattering. *J. Appl. Phys.* **2016**, *120* (6), 065303. https://doi.org/10.1063/1.4960577.

(15) Chandrasekaran, A.; van de Kruijs, R. W. E.; Sturm, J. M.; Bijkerk, F. Nb Texture Evolution

and Interdiffusion in Nb/Si-Layered Systems. *ACS Appl. Mater. Interfaces* **2021**, *13* (26), 31260–31270. https://doi.org/10.1021/acsami.1c06210.

(16) Zameshin, A. Probing Atmoic Scale Interface Processes Using X-Rays and Ions, University of Twente: Enschede, The Netherlands, 2018. https://doi.org/10.3990/1.9789036546508.

(17) Zameshin, A. A.; Medvedev, R. V.; Yakshin, A. E.; Bijkerk, F. Interface Formation in W/Si Multilayers Studied by Low Energy Ion Scattering. *Thin Solid Films* **2021**, *724*, 138569. https://doi.org/10.1016/j.tsf.2021.138569.

(18) de Boer, F. R.; Boom, R.; Mattens, W. C. M.; Miedema, A. R.; Niessen, A. K. *Cohesion in Metals: Transition Metal Alloys*; 1988.

(19) Bajt, S.; Stearns, D. G.; Kearney, P. A. Investigation of the Amorphous-to-Crystalline Transition in Mo/Si Multilayers. *J. Appl. Phys.* **2001**, *90* (2), 1017–1025. https://doi.org/10.1063/1.1381559.

(20) Eberhart, J. G.; Horner, S. Bond-Energy and Surface-Energy Calculations in Metals. *J. Chem. Educ.* **2010**, *87* (6), 608–612. https://doi.org/10.1021/ed100189v.

(21) Yamauchi, T.; Kitamura, H.; Wakai, N.; Zaima, S.; Koide, Y.; Yasuda, Y. Photoelectron Spectroscopic Studies on Interfacial Reactions in Zr/2×1(100)Si and Zr/SiO 2 /(100)Si Systems . *J. Vac. Sci. Technol. A Vacuum, Surfaces, Film.* **1993**, *11* (5), 2619–2622. https://doi.org/10.1116/1.578616.

(22) Cheng, Y.; Liu, J.; Stearns, M. B.; Stearns, D. G. Annealing Studies of Ru/Si Multilayer by High-Angle Annular Dark-Field Microscopy and HREM; Ceglio, N. M., Ed.; 1992; Vol. 1547, pp 167–175. https://doi.org/10.1117/12.51278.

(23) Nedelcu, I.; Van De Kruijs, R. W. E.; Yakshin, A. E.; Bijkerk, F. Thermally Enhanced Interdiffusion in MoSi Multilayers. *J. Appl. Phys.* **2008**, *103* (8). https://doi.org/10.1063/1.2907964.

Summary and Conclusion

This thesis describes advanced experimental research on the physical and chemical properties of bilayer and multilayer ultra-thin films. Atomic scale processes that occur at the interfaces of thin film stacks are known to dramatically influence their functional properties. This includes layer roughness and intermixing occurring during the film deposition process, as well as interdiffusion of layer materials and interlayer compound formation during usage of the thin-films, for example, exposure of an optically reflective multilayer stack to a high-power light source and electromigration due to current flow in integrated circuit devices. Currently, there is a critical demand for a broadly applicable material-selection-guide to design atomically sharp and stable layer stacks for various thin-film devices. This thesis has given an important onset for that. It is focused on understanding the surface and interface diffusion mechanisms involved during: (i) near room temperature layer growth, and (ii) low temperature annealing of transition metal (TM) and Si based layered systems. The thesis presents a novel scaling law for the effective interface width between two layers, which can be used for the selection of suitable layer materials to achieve well-controlled interfaces in a thin-film stack.

The intermixing and segregation processes during room temperature deposition were studied using high-sensitivity low-energy ion scattering (HS-LEIS). A film-on-substrate bilayer architecture was used for the layer growth studies. Using *in vacuo* LEIS, it was possible to obtain a "growth profile" by measuring the change in surface atomic composition as a function of sub-nanometer increase in the as-deposited film thickness. Key layer growth and interface properties such as the effective interface width, the layer closure thickness and the surface segregation of several TM and Si based bilayer systems were obtained from their corresponding LEIS growth profiles using a logistic-function-based interface atomic composition model.

A semi-empirical surface atomic exchange model was developed to describe the relation between the effective layer interface width and layer material properties such as surface energy and crystal structure. The model parameters were extracted by fitting the experimental effective interface width data of several TM-on-TM layered structures obtained from their corresponding LEIS growth profiles. The effective interface width could be described as an exponential function of the surface-energy difference between film and substrate atoms, with a subtrend based on the crystal structure of the layers. The model serves as a *scaling law* to predict the effective interface width and the layer closing thickness of TM-on-TM layered systems. In addition to the intermixing process, segregation of film or substrate atoms during growth was observed in some of the investigated TM-on-TM systems. The segregation phenomenon was attributed to the strain energy induced by the large atomic size between the film and substrate atoms (e.g. Ru-Sc), and in some cases, it could be attributed to the low

activation energy for self-diffusion (e.g. Cu). The investigated TM-on-TM systems were categorized into four types based on the observed intermixing and segregation characteristics, and a general rule was proposed to predict the possible growth type of TM-on-TM systems based on the substrate-film atomic radii difference ($r_s - r_f$), the enthalpy of mixing, and the surface-energy difference between substrate and film atoms.

The applicability of the proposed general rules of growth and interface characteristics for TM-on-TM systems was also studied for TM-on-Si systems. In all TM-on-Si (TM: Zr, Ta, Mo, Ru, Ir, Pt) systems investigated in this work, segregation of Si atoms during growth was observed. The effective interface width of all investigated TM-on-Si systems, except Zr and Ta on Si, followed the interface width scaling law obtained from the TM-on-TM studies. For TM-on-Si systems with a large atomic size difference ($r_s - r_f < -0.22$ Å), as in the case of Zr-on-Si and Ta-on-Si systems having large film atoms, a competing segregation mechanism of TM and Si atoms in the early stages of growth resulted in a reduced effective interface width when compared to the value predicted by the scaling law.

The interdiffusion of atoms during low temperature annealing (200ºC) was studied using high resolution cross-sectional transmission electron microscopy (XTEM). A multilayer architecture was used for thermal diffusion studies to limit the influence of surface oxidation and damage from XTEM sample preparation. In Nb/Si systems, Nb was found to undergo two microstructural transitions within the first 4 nm of as-deposited Nb on a Si layer: (i) an amorphous-to-crystalline transition with a strong texture around 2.1 nm, and (ii) transition to a polycrystalline growth around 3.3 nm. In order to study the effect of the Nb microstructure on interdiffusion via interfaces during low temperature annealing, three Nb/Si multilayers were deposited: (i) with 2 nm amorphous Nb layers, 3 nm strongly textured Nb layers, and 4 nm polycrystalline Nb layers with a reduced degree of texture. Nb/Si multilayers with amorphous and strongly textured Nb layers show better thermal stability during low temperature annealing (200ºC) when compared to a Nb/Si multilayer with polycrystalline Nb layers, because of the limited grain boundary pathways for diffusion in amorphous and textured Nb layers.

In the Zr/Si multilayer system, low temperature annealing (200ºC) resulted in complete solid state amorphization of the polycrystalline Zr layer and the formation of a thick amorphous ZrSi layer. The Zr/Si multilayers exhibited a stronger degree of interdiffusion and a solid state amorphization at 200ºC when compared to Nb/Si multilayers studied in this thesis and other Metal/Si structures reported in literature. The strong interdiffusion via the Zr-Si interfaces was explained by the large strain at the interfaces caused by the large atomic size difference (~ 0.42 Å) between Zr and Si atoms when compared to most other Metal/Si systems. In fact, Ce/Si multilayers, with a Ce-Si atomic size

difference of ~ 0.64 Å, were shown to exhibit interdiffusion even near room temperature in the first few days after deposition.

The following conclusions are derived from this thesis work:

(1) For near room temperature growth of TM and Si based systems:

- Intermixing between two layers during growth is a consequence of surface atomic exchange processes that are activated by: (i) ballistic collision between film and substrate atoms during deposition, and (ii) surface energy minimization, where the lowest surface energy atom tends to move toward the surface.
- The surface energy difference and preferred crystal structure (BCC, HCP, FCC) of the layer materials determine the extent of the intermixing and the effective interface width between the layers. In general, the magnitude of intermixing will be higher if the surface free energy of the substrate atoms is lower than the film atoms. Also, BCC TMs tend to show less intermixing when compared to HCP and FCC TMs because of the higher bond strength of BCC atoms.
- Floating segregation or surface segregation of atoms can occur in some systems in addition to the intermixing process. The strength of segregation depends on the surface energy difference, atomic size difference, and the enthalpy of mixing between the film and substrate atoms. Floating segregation can also be observed in the case of film or substrate atoms with low activation energy for self-diffusion (e.g. Cu), however, atomic size difference is the dominating factor. Si tends to exhibit floating segregation behavior during TM-on-Si growth.

(2) For low temperature annealing of TM-Si systems

- Intermixing between layer materials during low temperature annealing (< 300ºC) is a consequence of bulk diffusion of Si atoms facilitated by the grain boundaries in TM layers.
- In TM-Si layered systems, amorphous and strongly textured TMs with limited number of grain boundary pathways for diffusion show enhanced stability during low temperature annealing when compared to polycrystalline TM layers with more grain boundaries.
- A large atomic size difference between TM and Si atoms (e.g. Zr-Si) will lead to an increased strain energy at the interfaces. This will enhance the interdiffusion process, resulting in solid state amorphization and complete intermixing of few nanometer thick layers during low temperature annealing. In fact, spontaneous intermixing can occur even at room temperature over a period of time as in the case of Ce-Si with ~ 0.64 Å atomic radii difference.

Samenvatting en Conclusie

Dit proefschrift beschrijft geavanceerd experimenteel onderzoek naar de fysische en chemische eigenschappen van dubbelagen en multilagen ultradunne films. Het is bekend dat de processen aan atoomschaal die plaatsvinden op de grensvlakken van dunne-films hun functionele eigenschappen dramatisch beïnvloeden. Dit omvat laagruwheid en vermenging die optreden tijdens het film depositie proces, evenals interdiffusie van laagmaterialen en vorming van tussenlaag verbindingen tijdens gebruik van de dunne films, bijvoorbeeld belichting van een optisch reflecterende multilagen stapel aan een krachtige lichtbron en elektromigratie als gevolg van stroom in apparaten met geïntegreerde schakelingen. Momenteel is er een kritische vraag naar een breed toepasbare materiaalkeuzegids voor het ontwerpen van atomair scherpe en stabiele lagenstapels voor verschillende dunnefilmapparaten. Dit proefschrift heeft daarvoor een belangrijke aanzet gegeven. Het is gericht op het begrijpen van de oppervlakte- en interface-diffusiemechanismen die betrokken zijn bij: (i) laaggroei bij kamertemperatuur, en (ii) gloeien bij lage temperatuur van op overgangsmetaal (TM) en Si gebaseerde gelaagde systemen. Het proefschrift presenteert een nieuwe schaalwet voor de effectieve interfacebreedte tussen twee lagen, die kan worden gebruikt voor de selectie van geschikte laagmaterialen om goed gecontroleerde interfaces in een dunne-filmstapel te bereiken.

De processen van vermenging en segregatie tijdens depositie bij kamertemperatuur werden bestudeerd met hooggevoelige lage energie ionenverstrooiing (HS-LEIS). Een film-op-substraat bilaagarchitectuur werd gebruikt voor de laaggroeistudies. Met behulp van LEIS in vacuo was het mogelijk om een "groeiprofiel" te verkrijgen door de verandering in de atomaire samenstelling van het oppervlak te meten als een functie van sub-nanometer toename van de filmdikte zoals afgezet. Sleutellaaggroei en interface-eigenschappen zoals de effectieve interfacebreedte, de laagafsluitingsdikte en de oppervlaktesegregatie van verschillende op TM en Si gebaseerde dubbellaagse systemen werden verkregen uit hun overeenkomstige LEIS-groeiprofielen met behulp van een op logistiek-functie gebaseerd atomair samenstellingsmodel van de interface.

Een semi-empirisch oppervlakte-atoomuitwisselingsmodel werd ontwikkeld om de relatie te beschrijven tussen de effectieve laaginterfacebreedte en laagmateriaaleigenschappen zoals oppervlakte-energie en kristalstructuur. De modelparameters werden geëxtraheerd door de experimentele effectieve interfacebreedtegegevens van verschillende TM-on-TM gelaagde structuren die zijn verkregen uit hun overeenkomstige LEIS-groeiprofielen, te fitten. De effectieve interfacebreedte kan worden beschreven als een exponentiële functie van het oppervlakte-energieverschil tussen film- en substraatatomen, met een subtrend gebaseerd op de kristalstructuur van de lagen. Het model dient als schaalwet om de effectieve interfacebreedte en de laagsluitdikte van TM-

on-TM gelaagde systemen te voorspellen. Naast het vermengingsproces werd segregatie van film- of substraatatomen tijdens de groei waargenomen in sommige van de onderzochte TM-on-TM-systemen. Het fenomeen van segregatie werd toegeschreven aan de spanningsenergie die werd veroorzaakt door de grote atoomgrootte tussen de film- en substraatatomen (bijv. Ru-Sc), en in sommige gevallen kon het worden toegeschreven aan de lage activeringsenergie voor zelfdiffusie (bijv. Cu). De onderzochte TM-on-TM-systemen werden gecategoriseerd in vier typen op basis van de waargenomen vermengings- en segregatiekenmerken, en er werd een algemene regel voorgesteld om het mogelijke groeitype van TM-on-TM-systemen te voorspellen op basis van het substraat-film-atomaire radii-verschil ($r_s - r_f$), de enthalpie van mengen en het oppervlakte-energieverschil tussen substraat- en filmatomen.

De toepasbaarheid van de voorgestelde algemene regels voor groei en interface-eigenschappen voor TM-op-TM-systemen werd ook bestudeerd voor TM-op-Si-systemen. In alle TM-op-Si (TM: Zr, Ta, Mo, Ru, Ir, Pt) systemen die in dit werk zijn onderzocht, werd segregatie van Si-atomen tijdens de groei waargenomen. De effectieve interfacebreedte van alle onderzochte TM-op-Si-systemen, behalve Zr en Ta op Si, volgde de schaalwet van de interfacebreedte verkregen uit de TM-op-TM-onderzoeken. Voor TM-op-Si-systemen met een groot verschil in atomaire grootte (rs - rf < – 0,22 Å), zoals in het geval van Zr-op-Si- en Ta-on-Si-systemen met grote filmatomen, kan een concurrerend segregatiemechanisme van TM- en Si-atomen in de vroege stadia van groei resulteerden in een verminderde effectieve interfacebreedte in vergelijking met de waarde voorspeld door de schaalwet.

De interdiffusie van atomen tijdens gloeien bij lage temperatuur (200ºC) werd bestudeerd met behulp van hoge resolutie cross-sectionele transmissie-elektronenmicroscopie (XTEM). Een meerlagige architectuur werd gebruikt voor thermische diffusiestudies om de invloed van oppervlakteoxidatie en schade door XTEM-monstervoorbereiding te beperken. In Nb/Si-systemen bleek Nb twee microstructurele overgangen te ondergaan binnen de eerste 4 nm van zoals afgezet Nb op een Si-laag: (i) een amorfe-naar-kristallijne overgang met een sterke textuur rond 2,1 nm, en (ii) overgang naar een polykristallijne groei rond 3,3 nm. Om het effect van de Nb-microstructuur op interdiffusie via interfaces tijdens gloeien bij lage temperatuur te bestuderen, werden drie Nb/Si-multilagen gedeponeerd: (i) met 2 nm amorfe Nb-lagen, 3 nm sterk getextureerde Nb-lagen en 4 nm polykristallijne Nb-lagen met een verminderde mate van textuur. Nb/Si-multilagen met amorfe en sterk getextureerde Nb-lagen vertonen een betere thermische stabiliteit tijdens gloeien bij lage temperatuur (200ºC) in vergelijking met een Nb/Si-multilaag met polykristallijne Nb-lagen, vanwege de beperkte korrelgrenspaden voor diffusie in amorfe en getextureerde Nb-lagen.

In het Zr/Si meerlaagse systeem resulteerde gloeien bij lage temperatuur (200ºC) in volledige vaste toestand amorfisatie van de polykristallijne Zr-laag en de vorming van een dikke amorfe ZrSi-

laag. De Zr/Si-multilagen vertoonden een sterkere mate van interdiffusie en een amorfisatie in vaste toestand bij 200ºC in vergelijking met de Nb/Si-multilagen die in dit proefschrift en andere in de literatuur beschreven metaal/Si-structuren zijn bestudeerd. De sterke interdiffusie via de Zr-Si-interfaces werd verklaard door de grote spanning op de interfaces veroorzaakt door het grote verschil in atomaire grootte (~ 0,42) tussen Zr- en Si-atomen in vergelijking met de meeste andere Metaal/Si-systemen. In feite bleek dat Ce/Si-multilagen, met een Ce-Si-atoomgrootteverschil van ~ 0,64 Å, interdiffusie vertoonden, zelfs in de buurt van kamertemperatuur in de eerste paar dagen na depositie.

De volgende conclusies zijn afgeleid van dit proefschrift::

(1) For near room temperature growth of TM and Si based systems:

- Intermixing between two layers during growth is a consequence of surface atomic exchange processes that are activated by: (i) ballistic collision between film and substrate atoms during deposition, and (ii) surface energy minimization, where the lowest surface energy atom tends to move toward the surface.
- The surface energy difference and preferred crystal structure (BCC, HCP, FCC) of the layer materials determine the extent of the intermixing and the effective interface width between the layers. In general, the magnitude of intermixing will be higher if the surface free energy of the substrate atoms is lower than the film atoms. Also, BCC TMs tend to show less intermixing when compared to HCP and FCC TMs because of the higher bond strength of BCC atoms.
- Floating segregation or surface segregation of atoms can occur in some systems in addition to the intermixing process. The strength of segregation depends on the surface energy difference, atomic size difference, and the enthalpy of mixing between the film and substrate atoms. Floating segregation can also be observed in the case of film or substrate atoms with low activation energy for self-diffusion (e.g. Cu), however, atomic size difference is the dominating factor. Si tends to exhibit floating segregation behavior during TM-on-Si growth.

(2) For low temperature annealing of TM-Si systems

- Intermixing between layer materials during low temperature annealing (< 300ºC) is a consequence of bulk diffusion of Si atoms facilitated by the grain boundaries in TM layers.
- In TM-Si layered systems, amorphous and strongly textured TMs with limited number of grain boundary pathways for diffusion show enhanced stability during low temperature annealing when compared to polycrystalline TM layers with more grain boundaries.
- A large atomic size difference between TM and Si atoms (e.g. Zr-Si) will lead to an increased strain energy at the interfaces. This will enhance the interdiffusion process,

resulting in solid state amorphization and complete intermixing of few nanometer thick layers during low temperature annealing. In fact, spontaneous intermixing can occur even at room temperature over a period of time as in the case of Ce-Si with ~ 0.64 Å atomic radii difference.

Valorization and Outlook

Nanometer- and sub-nanometer-scale thin films have become an integral unit of advanced technological devices, especially in the fields of semiconductors and optics. Understanding the physics of atomic scale diffusion processes is important to fabricate atomically sharp interfaces in ultra-thin-film layered systems. This thesis presents a semiempirical model that describes the surface atomic exchange processes occurring during near room temperature layer growth. On the one hand, the experimental data for effective interface width and layer closure thickness of several transition metals (TM) and Si based bilayer systems reported in this thesis, serve as a database for the thin-film physics community; on the other hand, the values of the model parameters extracted based on the experimental data serve as a scaling law to predict the effective interface width as well as the layer closure thickness of TM and Si based bilayer systems. The practical significance of this work in terms of its application in science and society lies in the quantitative predictive power of the model: it provides the ability to select the most suitable layer materials based on the layer growth and interface characteristics, to achieve well-controlled interfaces in a thin-film stack. The ability to predict the interface width between two layers will be highly beneficial for optical and magnetic multilayer applications, whereas the ability to predict the growth and segregation characteristics will be useful in the fields of thin film catalysis and sensors, diffusion barriers, and semiconductor industry. In addition, the knowledge obtained from this work, especially the prediction of segregation behavior during growth, is expected to be beneficial in explaining scientific results in the field of surface physics without the need for advanced surface-sensitive characterization methods.

In addition to the layer growth studies during near room temperature growth, this thesis also presents a study on interdiffusion during low temperature annealing in TM-Si based systems. In the Nb-Si system, the diffusion of Si into the Nb layer strongly depends on the microstructural properties of the Nb layer. The data suggests that amorphous or strongly textured ultra-thin metal films with limited grain boundary pathways for diffusion, will exhibit better thermal stability than a polycrystalline layer. The results of Zr-Si study reveal the importance of atomic size difference between the layer materials in determining the thermal stability. The strain energy caused by the large atomic size difference between the layer materials can enhance the interdiffusion process during low temperature annealing and in the extreme case, can activate interdiffusion even near room temperature. These results will encourage further research in the direction of tuning microstructure properties of ultra-thin TM films and using novel thin-film designs, such as using interlayers, dopants, passivation of layers, to obtain enhanced thermal stability.

The results reported in this thesis are only early steps in moving toward designing and fabricating complex nano- and molecular-scale structures with atomic-scale control over diffusion processes. In the long term, the developments in the ultra-fast computing technology and its easy access to all scientific community and research groups, will provide the advanced knowledge and prediction capability of atomic diffusion processes required to enable the high-volume manufacturing of complex molecular- and atomic-scale thin-film devices. In the short- and mid-term, further research and understanding, including a further developed model, are required to facilitate the developments in a wide range of thin-film based technological applications. Based on this thesis work, the following points are identified as some of the important steps necessary to improve the layer growth model:

- Atomic size: Although the effect of atomic size on the segregation mechanism is explained qualitatively in this thesis, the surface atomic exchange model presented in this thesis does not include the atomic size of the layer materials, for the sake of simplicity. Therefore, an improved version of the model that considers the strain energy (atomic size difference) is necessary for the quantitative analysis of segregation during growth.
- Multi-element layered systems: The model presented in this thesis deals with the simple case of TM and Si based layered systems. However, several applications demand multi-element layers, such as compounds and alloys. The model currently lacks the capability of explaining the intermixing mechanism between film and substrate layers comprising multiple elements and with interstitial atoms, such as carbon, boron, oxygen, nitrogen. A quantitative estimation of growth and intermixing characteristics in multi-element layers, especially with interstitial atoms, will require a sophisticated model that considers various competing surface atomic exchange processes.
- Deposition Methods: The reported values of the semiempirical model parameters depend on the energy contribution from the deposition process, which varies strongly for different deposition methods. Therefore, the quantitative predictability of the model does not hold good for deposition methods significantly different from that of the magnetron sputtering in terms of incident atom energy, substrate temperature, ion bombardment. For high-energy depositions, such as ion-bombardment assisted deposition or pulsed laser deposition, deposition (ballistic collision) induced intermixing can be more significant than the surface-energy difference, whereas for CVD/ALD growth, the surface-energy induced intermixing can be more important than the ballistic-collision (deposition) induced intermixing. Nevertheless, the intermixing and segregation mechanisms and trends for other deposition methods should be qualitatively similar to that of magnetron sputtering. For a much broader applicability, future developments to the model must include the energy contribution from the deposition process.

Acknowledgements

In September 2015, Fred and Robbert encouraged me to continue with PhD research after finishing my master thesis. I agreed to take this journey/challenge before starting an industrial career. It has been 7 years since that discussion; looking back and connecting the dots, I express my sincere gratitude and thanks to Fred and Robbert for encouraging me to start the PhD research, for guiding me throughout the PhD journey, and for patiently supporting me in the last 2 years with my PhD thesis.

I am thankful to Fred for giving me the opportunity to do my internship, master thesis, and PhD work at the XUV Optics group, and for all the critical feedback and guidance, which helped me grow as an independent researcher. Most importantly, thank you for teaching me the art of looking at the bigger picture.

I express my sincere gratitude to Robbert for being my daily supervisor and for constantly encouraging critical thinking. Thank you for teaching me why it is important to understand and explain the cause (science), instead of just presenting the observable consequence (experimental data). “Why” is an important word that I have learnt from you.

Marko was a one-stop-solution for all scientific, technical, and Dutch language questions. I liked how he thought about every question I asked and gave a complete and sincere answer. I have learnt the effective-problem-solving skill from him. Marko, hartelijk bedankt! I would like to thank Eric for all the scientific discussions and fun conversations, especially in Dutch. Eric, I follow this at home – “to be continued”. I would like to thank Andrey and Igor (Igor, Igor, Igor!) for the scientific discussions and constructive feedback. I would like to thank Hartmut, Sebastian, and Joern from ZEISS for all the constructive feedback and great scientific discussions.

I would like to thank Mike for his technical support during my master thesis and PhD work, and for his friendship and great food off-work. I would like to thank Carin, Theo, Koen, Bart, Dennis for the nice conversations during the lunch-break walk to Coop supermarket – dank jullie wel! het was geweldig om met jullie samen te werken! I would like to thank all my (former) colleagues for the constructive feedbacks and scientific discussions, coffee-break conversations, and fun activities: Airat, Cris, Parikshit, Andrey, Igor, Dmitry, Roger, Gosia, Olena, Sasha, Kostya, Roman, Philip, Wesley, Seda, Maria.

I would like to thank Han and Sonja for hosting me and making me a part of their family. My strong connection with the Netherlands (Dutch people, food, language, culture, tv shows) started from this family. Hartelijke groetjes!

Finally, I would like to thank my parents, family, and friends for their continuous love, support, and encouragement. Last 2 years have been extremely difficult with constant traveling and long work hours. There was limited time for personal life and I spent most of it writing this thesis. I would like to thank my wife, Pavithra, for being extremely selfless and supporting me throughout this journey and constantly pushing me to finish this thesis.

Once again, I express my sincere gratitude, appreciation, and thanks to my supervisors, (former) colleagues, and family for all the support, patience, and encouragement in completing this thesis.

About the Author

Anirudhan Chandrasekaran was born on the 29th of June 1992 in Madurai, Tamil Nadu, India. After graduating from high school in 2009, he pursued his undergraduate degree in Nanotechnology at SRM University, Chennai, India. During his undergraduate studies, he received the Australian Government DEEWR scholarship for study-abroad program at La Trobe University, Australia. In October 2013, he moved to Germany to pursue his Master of Science degree in Optics and Photonics at Karlsruhe School of Optics and Photonics, Karlsruhe Institute of Technology. During his Master's degree, he moved to the Netherlands in 2014 to do his internship at the Industrial Focus Group XUV Optics, University of Twente. After completing the Master's degree coursework in Germany in May 2015, he went back to the Industrial Focus Group XUV Optics for his Master thesis work on the "Development of La/B based multilayer mirrors for B-EUV Lithography". In November 2015, he started his PhD work at the Industrial Focus Group XUV Optics, University of Twente. While working on his PhD thesis, he moved to Belgium in February 2020 to start his industrial career as a Senior Process Engineer at ASM Belgium. In 2020 and 2021, he traveled between Europe and Asia business units, and in January 2022, he was transferred to the ASM America business unit in Phoenix, USA, where he is currently working as a Senior Process Engineer.